Technische Universiteit Delft

Design of actively controlled semi permeable trailing edge inserts for aero-acoustic noise reduction

Yasir Khan

TU Delft

Design of actively controlled semi-permeable trailing edge inserts for aero-acoustic noise reduction

by

Yasir Khan

to obtain the degree of Master of Science
at the Delft University of Technology,
to be defended publicly on Wednesday, October 28, 2020 at 14:00.

Student number:	4770609	
Project duration:	October 1, 2019 – October 28,2020	
Thesis committee:	Prof. dr. ir. S. van der Zwaag,	TU Delft, supervisor
	Ir. J. Sinke,	TU Delft
	Dr. Y. Tang	TU Delft
	A. Rubio Carpio	TU Delft

An electronic version of this thesis is available at `http://repository.tudelft.nl/`.

TU Delft

Preface

This report was written to fulfill the requirements for obtaining the degree of Master of Science in Aerospace Engineering at Delft University of Technology. This thesis project concludes my two years of comprehensive study at Delft. My experience with research has been bitter-sweet in the past one year. It was pleasing as well as challenging, in parts. But this journey could not have been possible without the support of so many people around me.

First of all, I express immense gratitude towards my supervisor, Prof. Sybrand van der Zwaag, for his constant guidance, both technical and moral, throughout the length of my thesis. I feel my learning curve continuously went up while working with him.

Additionally, I would like to thank Reza Hedayati for his valuable assistance in the initial phase of my thesis. Furthermore, I would also thank Peter van Dulk, Berthil Grashof, Stefan Bernardy and David Wassdorp for their valuable technical support for my thesis.

Lastly, I could not have reached this position without the unconditional love and support of my mom and dad who cannot be thanked enough.. . .

Yasir Khan

Delft, October 2020

Abstract

An experimental study is conducted on the design of actively controlled semi-permeable inserts for mitigating turbulent boundary layer noise originating from the trailing edge of an airfoil. Two sets of perforated inserts with hole diameter: 0.8 mm and hole spacing: 1.5 mm & 3 mm, are considered. The inserts are 3-D printed with a middle-disk shift mechanism to change flow parameters across the perforated disks without modifying the hole diameter and hole spacing. The pressure drop experiments across the inserts are carried out at pipe-level Reynolds numbers ranging from 160 to 2380 to characterize the variation in flow permeability, flow resistivity and form factor of inserts.

The tests are carried out in two phases: static and dynamic configuration. A novel static set-up with orientation pins is devised to implement the middle-disk shift mechanism. For the dynamic configuration, an actuation device is designed and constructed to control permeability on-line through an external motor controller. The findings show that the middle-disk shift mechanism can achieve a maximum permeability variation of ΔK_{max}>4.5x10^{-9} m^2 at a net effective porosity change of $\Delta\epsilon_{Eff}$>72%, for the current set of perforated inserts. The results also suggest that the mechanism is most potent in the range of 50% closed hole (half shut)- to 100% closed hole (completely shut)- orientations. The flow parameter variations for the static configuration are fairly replicated by the dynamic configuration, thereby, establishing repeatability of the actuation device. Therefore, the dynamic configuration set-up holds good promise for up-scaling to real structures, that is, trailing edge of an airfoil with relevant optimization.

Contents

List of Figures

List of Tables

1 Introduction

1.1. Aero-acoustic noise: What is it and why is it relevant?

In today's world, noise pollution is a topic of major concern. Although air-transport is pertinent to the present society, accompanying noise problem can be a cause of major concern. The perception of sound also has psychological causes hence for noise originating from an aircraft [36], the annoyance can be reduced by giving people an "impression" that their preferences are being taken into account. A great example of it, in the past, was the thunderous roar of a Concorde supersonic jet which was perceived as music to ears of aviation enthusiasts while it was intimidating to others [1]. Alongside acoustic variables like pitch and loudness, non-acoustic variables such as perceived control, attitudes towards source and noise sensitivities can contribute towards the reaction a person has towards sound [14, 29].

Aircraft noise is increasingly playing a major role as a noise pollution contributor in modern times. For example, the noise produced by aircraft operating at airports near urban settlements causes significant reduction in service hours of flight in order to comply with the noise restrictions set by international aviation bodies [58]. A key component of external aircraft noise, during take-off and landing is the broadband sound generated by turbulent flow around the air frame and wing. This is the flow-induced sound source. This air frame noise is usually generated from landing gears, flaps and slats. In helicopters or UAVs, the aero-acoustic noise can originate from rotor blades. The turbulent flow induced pressure fluctuations negatively affect the aircraft fuselage as fatigue loading on the outer panels or as vibration induced acoustic noise inside the aircraft cabin, thus, potentially becoming a source of discomfort for passengers. Free turbulence is considered to be very inefficient at low Mach numbers hence, majority of the acoustic noises originate from interaction of turbulence and airfoil's surface [43]. Therefore, the scattering of turbulent pressure fluctuations and their translation into pressure waves contributes to generation of acoustic noise from the external frame of an aircraft. These induced vibrations can cause costly damages to structures, thereof, making the study for mitigation of turbulent boundary layer induced vibrations and acoustics imperative. The reliable and efficient prediction as well as reduction of the noise produced from air-flow over wind turbines/aircraft trailing edges is crucial for rotor blade/aircraft wing design[17]. Figure 1.1 displays the key sources of aero-acoustic noise in an aircraft.

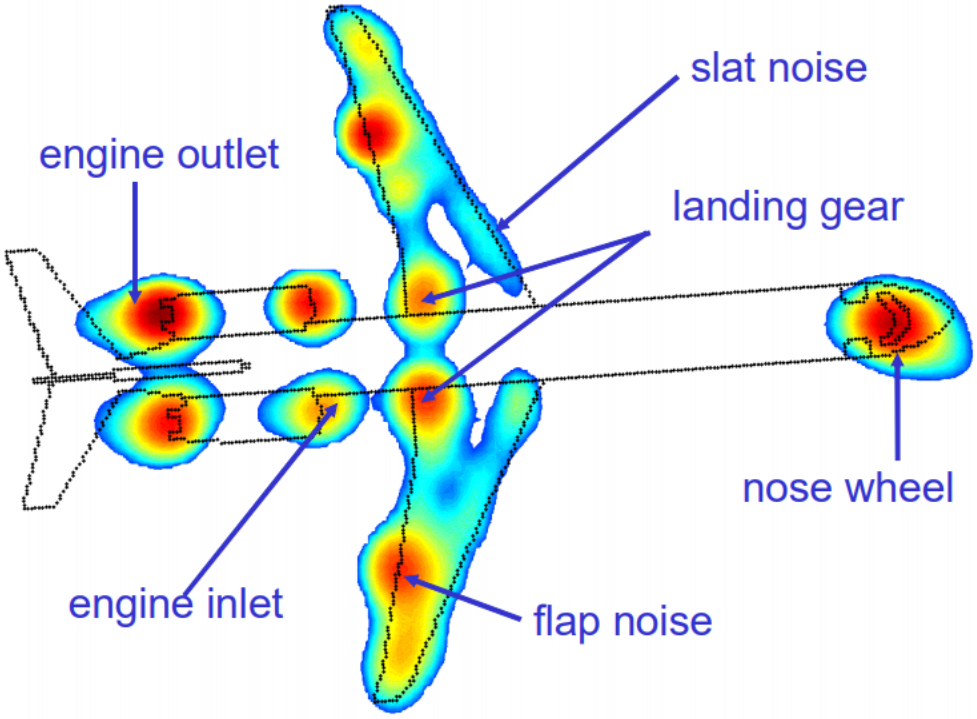

Figure 1.1: Prominent noise sources in an aircraft measured with a microphone array [43]

1.2. Mechanisms of Noise generation

Sound is a pressure disturbance that travels in the form of a wave without causing major fluctuations in density and velocity of fluid in which it passes through. The pressure of sound waves is however expressed in terms of a logarithmic scale whose units are decibels :

$$SPL(dB) = 20.log\frac{p_{rms}}{p_{ref}} \tag{1.1}$$

Here p_{rms} is the root mean square value of pressure and p_{ref} is the reference value of pressure taken as 2 x 10^{-5} Pa [52]. During the flow of sound over not-so-long distances we assume that fluid presents no viscous force and therefore sound is assumed to flow in a friction-less or inviscid media. The inertial forces of motion are presumed to push sound waves through the medium.
The production of flow induced noise is due to various mechanisms which can be broadly categorized into three categories. The type of mechanism depends on the flow parameters of fluid such as Reynolds number, type of boundary layer and geometry of object in flow. The three prominent mechanisms of flow induced noise in the presence of solid bodies are as follows:

1.2.1. Vortex shedding noise

Figure 1.2 shows that the fluid flow past a bluff body causes vorticity in the shape of Von Karman vortex street shape. This results in fluctuations in the pressure along the surface of the body which propagates outward in the form of sound. The noise produced via this

mechanism has a characteristic frequency known as Tonal frequency.

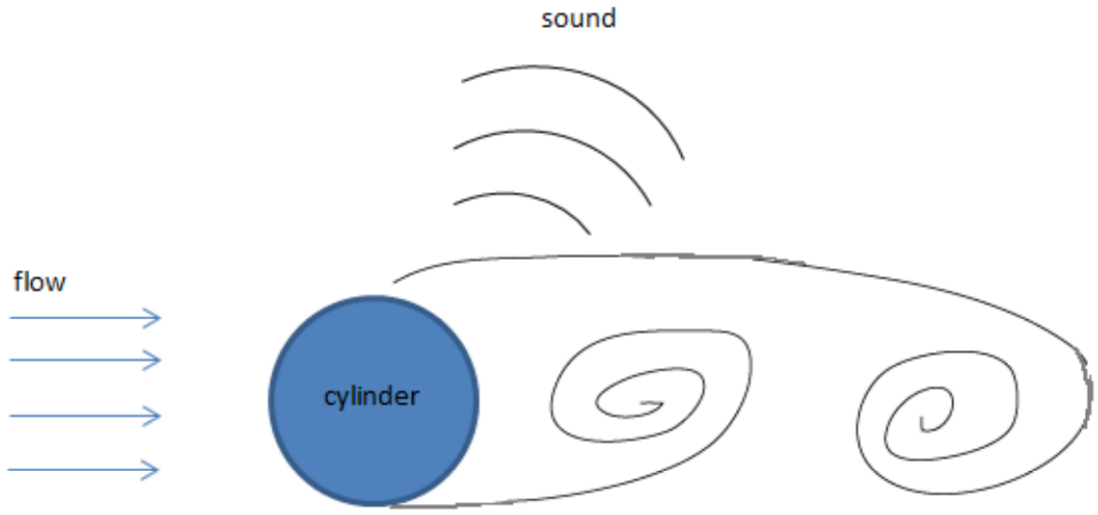

Figure 1.2: Noise generation through Vortex shedding [52]

1.2.2. Turbulence - Structure interaction

Figure 1.3 displays the vortical structures that are shed by a bluff body present in the upstream of the specimen. The vortical structures radiate sound when they are entrenched on a solid surface like leading edge of a wing.

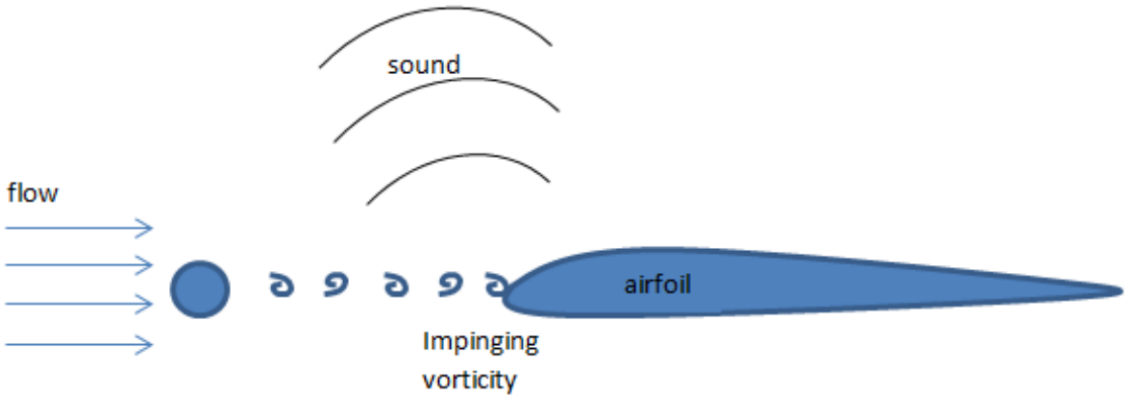

Figure 1.3: Noise generation through turbulence - structure interaction [52]

1.2.3. Trailing edge noise

Figure 1.4 presents the pressure fluctuations on a surface that can also occur while vortical structures are convecting in the turbulent boundary layer. They lead to the generation of sound carrying broadband characteristics. Boundary layer instabilities can also lead to sound generation that carries a tonal character.

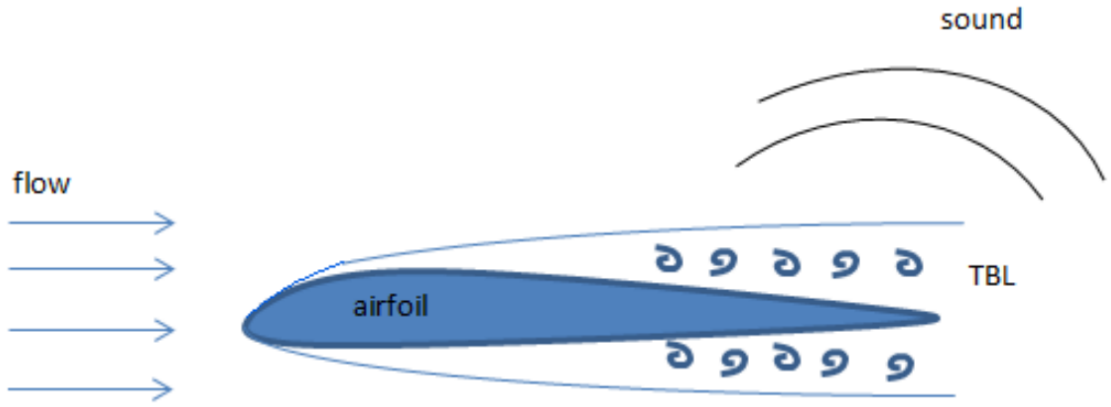

Figure 1.4: Noise generation through trailing edge of blade [52]

The trailing edge noise conceived within the turbulent layer over the airfoil is prominent source of sound for wind turbines [44], ventilation systems [40] and aircraft wings [46]. Noise is created by local stress fluctuations in flow (viscous stress effects); pressure fluctuations at walls (e.g. dipole sources at solid boundaries); mass and heat fluctuations (distributed mono-pole sources); and external fluctuating force fields [43]. Apart from acoustic waves, vorticity and thermal instability waves are also generated with the flow of fluid but they get convected with the flow while acoustic waves propagate relative to flow with speed of sound. The energy of acoustic waves is very small compared to the other forms of fluctuations. Generally, when a turbulent flow approaches an airfoil, a boundary layer forms along the surface which is further convected past the trailing edge. A pressure difference that develops between suction and pressure side of the airfoil due to its design causes tip vortex at the side-edges of the airfoil. This flow over an airfoil is schematically depicted in the Figure 1.5.
The mitigation of this unwanted sound has been an area of interest for several researchers in the past decade. From the time of taking inspiration from nature for developing serrated wings to more advanced porous materials, researchers have tried to reduce the energy content of turbulent structures. In theory, a reduction in span-wise coherence length at trailing edge or a mitigation of scattering efficiency of surface discontinuities can significantly reduce noise sources near trailing edge. The mechanisms to reduce turbulent flow induced trailing edge noise are discussed in Section 1.3

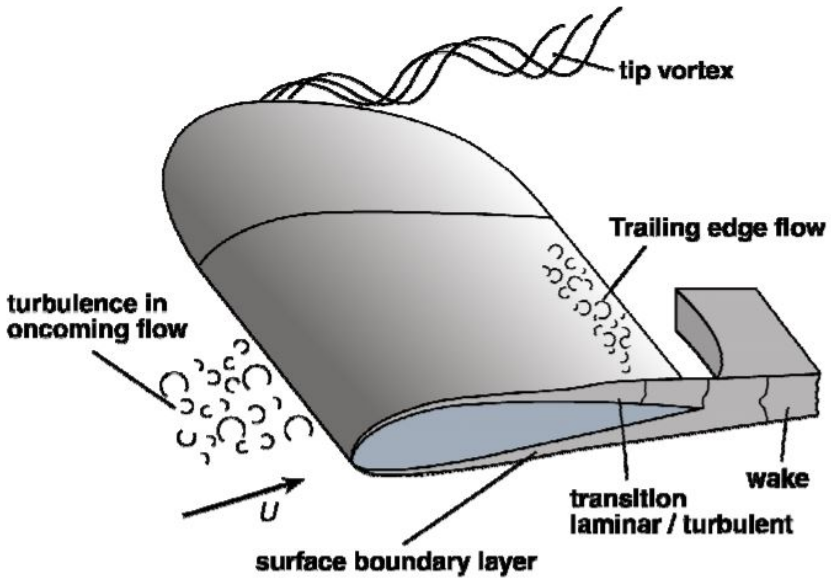

Figure 1.5: Interaction of flow over an airfoil [43]

1.3. Past strategies to mitigate trailing edge noise

The aero-acoustic noise phenomenon has been under research for the past several decades to gain physical understanding of turbulent flow as well as to mitigate noise sources. Most of the erstwhile tests have centered around reducing energy content of the turbulent structure, decreasing span-wise coherence length at trailing edge or mitigating scattering efficiency of surface discontinuity [47].

The earliest researches were inspired from nature and aimed at reducing acoustic pressure waves. One such example is about Owls. They are known for their capability of silent flight which helps them hunt with ease. Structurally Owl's wings are permeable at the end and they also contain fringes on the trailing edge of their feathers. These peculiar characteristics got translated into man-made solutions for the aircraft industry. Some strategies already employed in the past on the trailing edge of an aircraft wing are as follows: serrated trailing edge [5, 10, 25] (Section 1.3.1), brush-like edges[15] (Section 1.3.2), finlets[11] (Section 1.3.3), aeroacoustic optimization of airfoil shape [31, 37], boundary layer suction/blowing [4, 18], metal foams with and without polymeric coatings [22] (Section 1.3.4) and passive perforated inserts [47] (Section 1.3.5). Past researches have shown that both trailing edge serrations and trailing edge brushes haven't been able to yield noise reduction of more than 7 dB at frequency ranges of 1-2 kHz [3, 23].

The following sub-sections list some reliable models of trailing edge modifications that have been incorporated in an airfoil to impede pressure fluctuations at the edges, thereby, reducing noise.

1.3.1. Trailing Edge Serrations

In the last decade, serrated trailing edge modifications (Figure 1.6a) were considered to offer most effective noise reduction due to their design simplicity [39, 43] . Some recent investigations have displayed that air-flow passing through serrated airfoils is strongly three dimensional with vortical structures emerging along edges of serrations [3]. Flow mea-

surements and computations have shown that turbulent flow seeps into the gaps between serrations at lower angle of attacks as well[30].
Hence, an update on the design was implemented by Avallone et al [5] wherein they created iron-shaped curved trailing-edges and performed numerical computations using Lattice-Boltzmann solver to solve the problems faced by conventional straight serrated edges. Far-field noise and flow field was investigated using the newly developed design. The serration extent was 20% of chord length and had a wavelength of 20 mm. The iron-shaped design reduced far-field broadband noise by 2 dB in the range of 5 <St <15 (Figure 1.6b). The Strouhal number is a dimensionless quantity describing oscillating flow mechanisms. It is given by the formula : $St = \frac{fL}{U}$ where f is the frequency of vortex shedding, L is the characteristic length and U is flow velocity. It was observed that newly developed design could mitigate both outward and downward flow motions near serrations. But strong outward and inward flow motions were seen at the serration tip with the new model. An important conclusion from their paper was that intensity of scattered pressure waves depends on the stream-wise location and the reduction in overall sound pressure level (OSPL) was due to modifications at the root. Therefore, wing tip modifications are imperative for sound mitigation caused by turbulent flow generated noise.

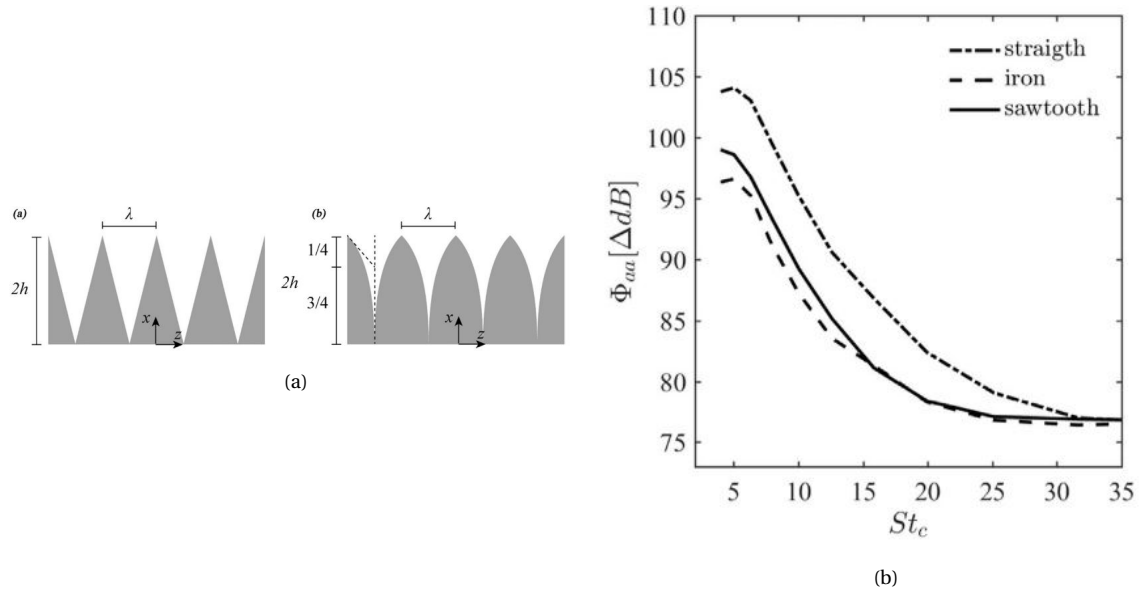

Figure 1.6: Design of saw-tooth edges alongside traditional edges and power spectra comparison;(a) Sketch of (a) Conventional and (b) Iron shaped trailing-edge serrations; and (b) Power Spectra of far-field pressure fluctuations for straight, saw-tooth and iron-shaped trailing-edge serrations [5]

1.3.2. Trailing Edge Brushes

The focus on wing-tip modifications lead researchers to create trailing edge compliant brushes that provided a credible solution for mitigating Turbulent Boundary Layer at Trailing Edge (TBL-TE) by combining the effects of porosity and trailing edge geometry [15]. A study by Ortmann et al [45] demonstrated that the negative effects of thin slit like brushes on the lift coefficient of airfoil was minimal. Past experiments have shown that brushes are highly efficient in disorganizing the Von Karman vortex street and suppressing the vortex shedding, thereby producing lower noise emissions. The crucial parameters for noise mit-

igation by a brush are the fibre length, fibre diameter, and their density[45].
Finez et al [15] conducted research on a well cambered NACA 65(12)-10 airfoil. Figure 1.7a shows brush samples of different fibre diameters and lengths that were installed on the trailing edge of the airfoil. They achieved a noise reduction of maximum 3 dB at 600-2000 Hz frequency range as shown in Figure 1.7b. The reason for noise reduction was investigated to be disorganization of turbulent structures of air flow via the span-wise fibres of brush. The brushes were found to reduce span-wise coherence of turbulent eddies to a large extent. But, a high curvature of incident flow led to production of a secondary acoustic source, thereby, reducing potential noise abatement in the 2000-5000 Hz frequency range and limiting the usage of brushes at the trailing edges.

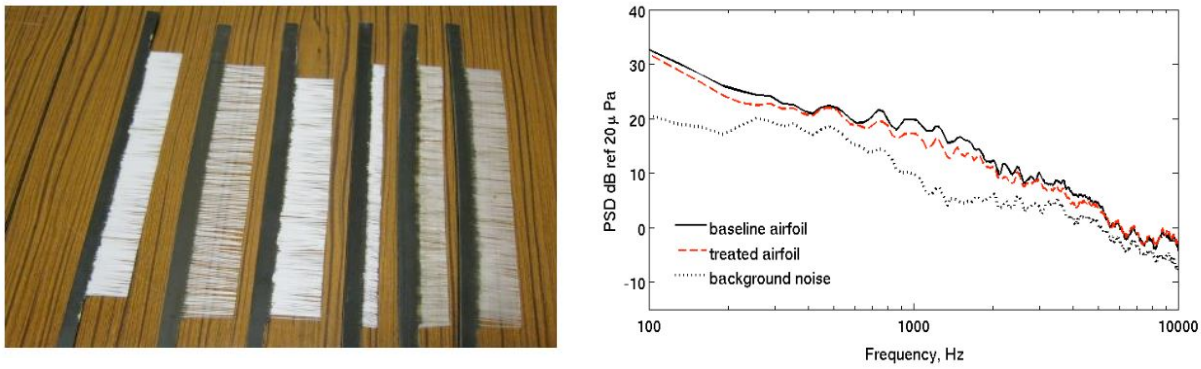

(a) (b)

Figure 1.7: Samples of different brushes used in tests and spectral density comparison levels for baseline and treated airfoils;(a): Brushes of different lengths and diameters to be installed on airfoil trailing edge; and (b): Acoustic pressure spectral density in far field [15]

1.3.3. Trailing edge Finlets

Clarks et al [11] did extensive computational and experimental studies to investigate the fluid mechanics of finlets. The results of simulation suggested that the suction side of finlets mitigate noise by concealing the surface pressure fluctuations by retarding the flow between finlets, thereby, reducing noise. On the other hand, pressure side finlets reduce noise by contrasting span-wise organized turbulent structures through formation of boundary layers on finlets themselves. Figure 1.8a shows a trailing edge consisting of long, thin stream-wise elements (finlets) spaced evenly at trailing edge. A noise attenuation of upto 10 dB at Re = $3x10^6$, for the far-field noise, was found in an experimental setup (Figure 1.8b). The experiments showed that noise attenuation was mostly found at frequencies below 2 kHz. The flow simulations also displayed that suction side of finlets were majorly responsible for noise attenuation. Therefore, the ineffectiveness of the finlets in reducing SPL post-2 kHz is considered to be a major drawback for the model.

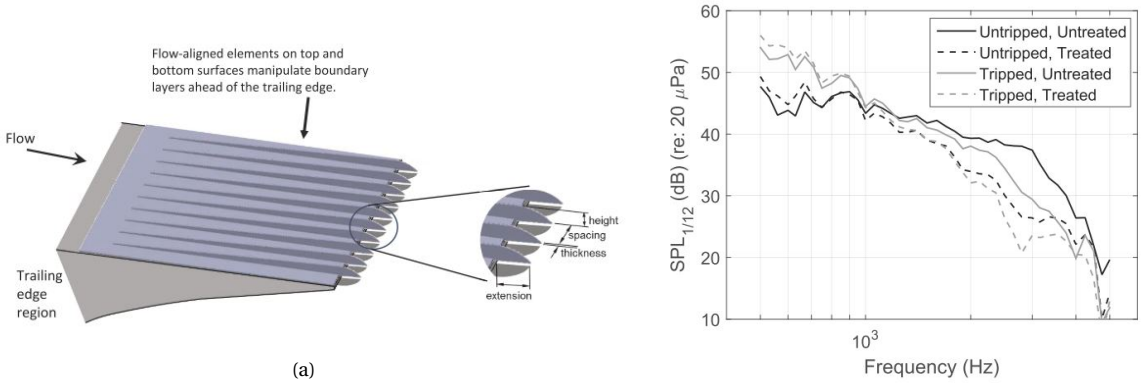

(a) (b)

Figure 1.8: Finlet design at trailing edges and resulting noise spectra of treated trailing edge. Figure (a): Finlet concept of Clark. Figure (b): Noise spectra in 1/12th octave bands [11]

1.3.4. Trailing Edge Porous Inserts

The application of permeable trailing edge inserts has been studied extensively by various researchers in the field of aero-acoustics. It is well established that permeable trailing edge inserts reduce the acoustic impedance jump at the airfoil edge and assist in noise scattering. They do so by relocating the impedance jump to other locations in the stream-wise direction, like solid-permeable junction [28, 32], that lead to a destructive interference of stream-wisely distributed noise sources. The permeability of the material plays a decisive role determining the flow interaction between suction and pressure sides of airfoil, thereby decreasing the magnitude of impedance [21]. Therefore, application of more permeable materials leads to higher noise mitigation, in general.

In one of the previous studies on permeable inserts, Sarradj and Geyer [51] created fully porous airfoil of different materials: polymer, glass and metal with variable air-flow resistivities. They tested aerodynamic and aero-acoustic performances and observed that even though a noise reduction of 8 dB was achieved, the lift coefficient (C_L) decreased by 70%. Thus, it demonstrated that completely porous airfoils are of no significant usage, as aerodynamic properties can't be compromised to such a large extent.

A recent study by the same authors [19] on partially porous airfoils resulted in a maximum noise reduction of 10 dB at Strouhal range of S_t = 10-70. It was achieved by covering the frontal portion of airfoil with a thin impermeable film. Important takeaway from the research was that increasing permeability of the porous part increases boundary layer thickness, turbulence intensity in the vicinity of trailing edge as well as in wake region along with wake deficit.

Another study by Geyer et al [20] included experiments on generation of trailing edge noise on airfoil made with different porous materials. The chord-wise extent of porous material was varied during experimentation which resulted in an increase in noise for some specimens as compared to solid airfoil due to higher surface roughness, very low porosity, and possible induced-vibration of trailing edge. Also, air-flow resistivity and extent of porous material installation in chord-wise direction was stated as having strong influence on the lift and drag coefficients. Figure 1.9 shows sample 3D sound maps for non-porous airfoil with the chosen prismatic integration volume in blue that is used to derive spectra of noise contributions produced by noise source of interest.

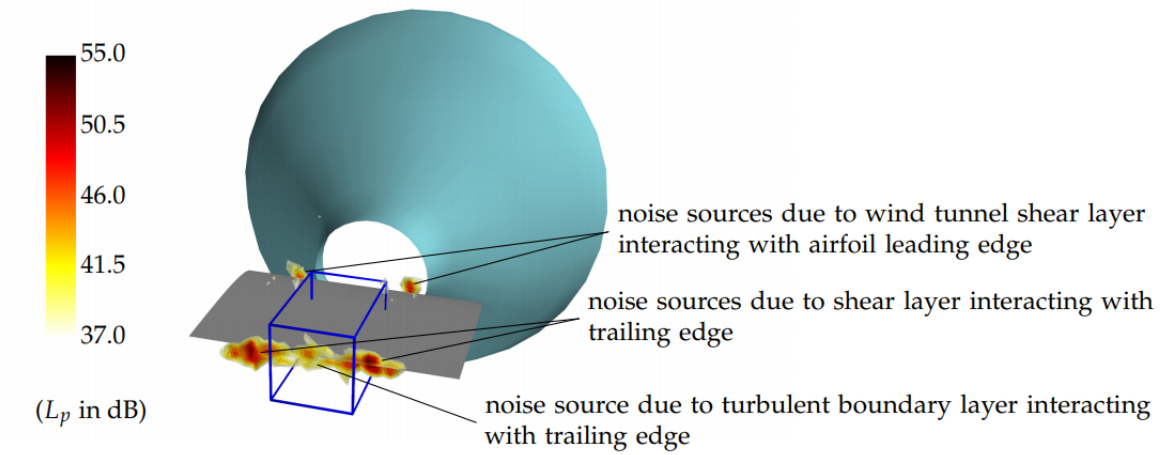

Figure 1.9: Sound maps obtained for a solid airfoil for a third octave band with centre frequency of 5 kHz and flow speed of 81.5 m/s. [20]

The effectiveness of permeable inserts with respect to angle of attack was studied by Herr et al [24] who applied porous inserts at 10% of chord length of airfoil. The partially porous airfoils caused a noise reduction of 2-6 dB but the effect of porous trailing edge reduced as the angle of attack was increased. Rubio Carpio et al [47] made similar observations after employing Ni-Cr-A metal foam inserts on NACA 0018 airfoils at 10% and 20% chord lengths. They remarked that at lower frequencies, by increasing the angle of attack, a reduction in the noise abatement ability of the porous treatment was observed while at higher frequencies, better noise abatement was observed. Noise abatement of upto 11 dB was observed at 20% chord length at zero degree angle of attack.
Subsequently, Hedayati et al [22] also worked on modifying metal foam inserts by spray-coating them to control the thickness of the struts of the foam and to vary their average diameters. The pore geometry was modified to achieve noise reduction in the experiments. Metal foams with pore sizes of 580, 800 and 1200 μm were internally spray-coated with an elastomeric coating with different degrees of layering to get different pore sizes (Figure 1.10a). The experimental data showed that the coating has significant impact on airflow resistivity but minimal effect on frequency - dependant noise reduction and on absolute noise reduction levels (OSPL). In fact, the results of the experiments showed that coated foams reduced noise relatively similar to uncoated foams of equivalent sizes (Figure 1.10b). Therefore,the focus of the present research work is on an alternative permeable trailing edge insert design, that is, the perforated channel inserts. This research exploits the fact that a smoother transition from the solid wing to porous insert at the trailing edge leads to lesser flow field fluctuations, thereby, reducing noise generation. Section 1.4 describes the acoustic capabilities of perforated channel inserts with respect to metal foams and subsequent sections list the need for actively controlling the system.

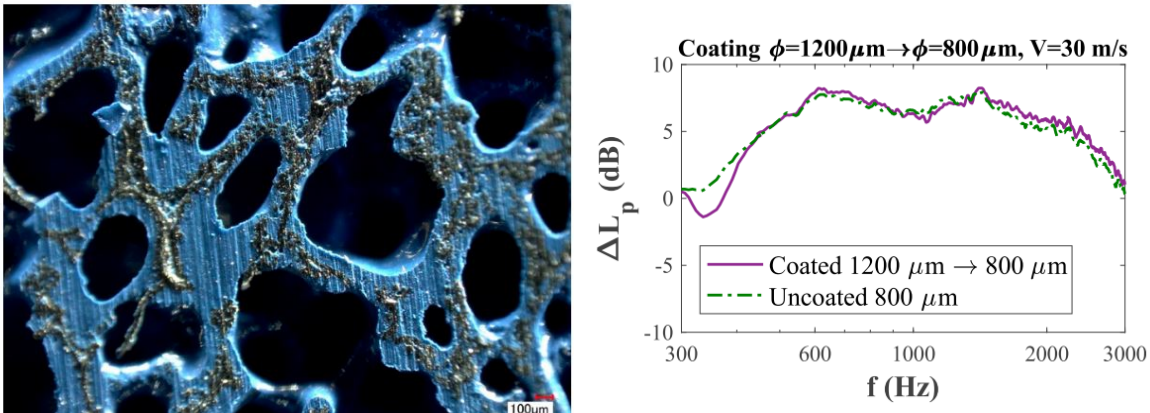

(a) (b)

Figure 1.10: Micro-structure of spray coated pores and resulting acoustic pressure drop comparison with baseline; (a): Cross-section of trailing edge spray-coated by solvent based paint; and (b): Comparison of noise abatement between coated and uncoated trailing edge with respect to baseline edges [22]

1.4. Trailing Edge Perforated Channel Inserts

The perforated channel inserts are 3-D printed specimens with cylindrical channels that make it porous. Rubio Carpio et al [47] conducted acoustic experiments on metal foam and perforated samples to compare the noise mitigation among them due to difference in their topography and permeability. Two perforated inserts of hole spacing 3 mm and 1.5 mm were chosen to contrast with metal foams of hole diameter 450 μm and 580μm. The comparison of the far-field noise emission from the base model and the permeable counterparts was recorded in terms of $L_{p(1/3)}$ (Sound Pressure Levels in 1/3-octave band) at no angle of incidence ($\alpha = 0^o$). Figure 1.11a displays the relationship of relative 1/3-octave band sound levels to the frequency bandwidth. It is calculated by the following equation:

$$\Delta L_{p(1/3)} = L^{solid}_{p(1/3)} - L^{perm.}_{p(1/3)} \tag{1.2}$$

It was observed that perforated channel insert of higher permeability, l_h = 1.5 mm (cyan), reduced more noise compared to its counter-part, l_h = 3 mm (yellow).
Interestingly, the perforated insert of hole spacing, l_h = 1.5 mm showed a strong presence of tonal noise at f_c = 630 Hz due to vortex shedding from the blunt end of the body of airfoil. The two perforated inserts also show similar trends of noise abatement with respect to the frequency bandwidth - something which is not present in the metal foam inserts. For the metal foam inserts, a higher d_c of the foam (orange) led to more noise compared to the baseline model post the cross-over frequency f_c which can be attributed to increased roughness of the material.

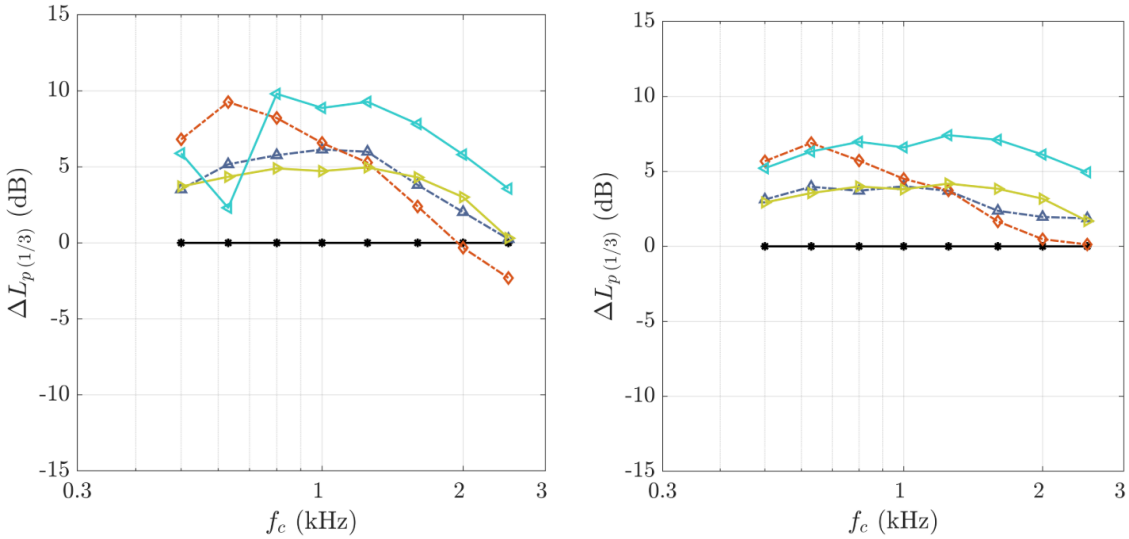

Figure 1.11: Relative $L_{p(1/3)}$ values with respect to solid insert at U_∞ = 26 m/s; (a) no incidence; and (b) $\alpha = 4.8^o$ [47]

A second set of experiments conducted at $\alpha = 4.8^o$ showed that noise abatement was at par with previous data but no tonal noise was present throughout the frequency bandwidth for perforated channel insert of l_h = 1.5 mm. Figure 1.11b displays the $\Delta L_{p(1/3)}$ values for the airfoil tested at $\alpha = 4.8^o$.

The Overall Sound Pressure Level (OSPL) which is the integrated sound pressure level across the complete frequency bandwidth is an important parameter to consider when gauging the acoustic characteristics with respect to external variables like permeability, free stream velocity, etc. It is given by the following equation: $OSPL = 10log_{10}\sum_{f_c} 10^{L_{p(1/3)}/10}$. The same study also found a direct relation between OSPL and permeability since the noise mitigation abilities increased with increase in permeability of inserts with similar pore structure. Hence, Flow Permeability (K) of the porous insert was considered to be a major contributing factor to TBL-TE noise reduction while other parameters like Tortuosity (Γ) also played a certain role. The type of material pore arrangement also affects the fluid-dynamic and acoustic features at the interface. For example, application of very small pore diameters ($d_h < 0.8$ mm) or hole spacing ($l_h < 1.5$ mm) can create hydro-dynamically rough surfaces which can lead to production of excess noise at high frequency bandwidth. Such arrangements can counter the benefits of installing permeable materials at the edge of airfoil [48]. Rough surfaces can also lead to higher turbulence close to the walls due to additional surface drag and add re-circulation zones within the porous medium. Manufacturing processes also limit the surface smoothness of the material and add to its roughness. Lately, the use of additive manufacturing techniques like 3-D printing have helped in greatly improving the finish quality of the inserts [27].

Another study by Rubio Carpio et al [50] was conducted on perforated samples of same hole diameter ($d_h = 0.8$ mm) but varying line spacing and hence different flow permeablities (K). The perforated samples were tested at two angles of attack $\alpha = 0.2^o$ and $\alpha = 5.4^o$. The noise scattering of perforated trailing edges was compared to that of open-cell metal foam inserts with random micro-structure but similar permeablities. The change in maximum noise at-

tenuation $\Delta L_{p,max}$ with permeability K was calculated and fitted to a hyperbolic function to ease the interpretation of the data. Equation 1.5 gives defines the hyperbolic function:

$$\Delta L_{p,max} = atanh(bK) \tag{1.3}$$

where a is the asymptotic $\Delta L_{p,max}$ value and b is the slope of the function within the low permeability range. Figure 1.12 plots the $\Delta L_{p,max}$ with respect to the permeability (K) for different samples and angles of attack. It is observed that for perforated inserts at $\alpha = 0.2^0$, increasing the permeability to K = 3.5 x 10^{-9} m^2 causes up to 8.3 dB ($\Delta L_{p,max}$) noise mitigation. Subsequently, further increasing the permeability of the material only mitigates noise by $\Delta L_{p,max} \approx 1$ dB. Also, increasing the angle of attack α to 5.4^0 reduces the noise attenuating capabilities of the system. Also, it can be inferred that for inserts of higher permeablities (l_h = 1.5 mm), the decrease in noise mitigation capabilities for increase in lift conditions is approximately 2 dB while inserts with lower permeablities (l_h = 5 mm) only have a loss of approximately 0.5 dB. Therefore, taking into account the loss of lift characteristics and high sensitivity to change in α, inserts with moderate permeability (below a threshold of K = $3.5x10^{-9}m^2$) are recommended for future research.
The current study of work draws inspiration from Figure 1.12 and intends to vary the Flow Permeability (K) of perforated channel inserts in the region of K = 0-3.5x10^{-9} m^2 through an actuation system that can potentially be scaled-up to application in real structures.

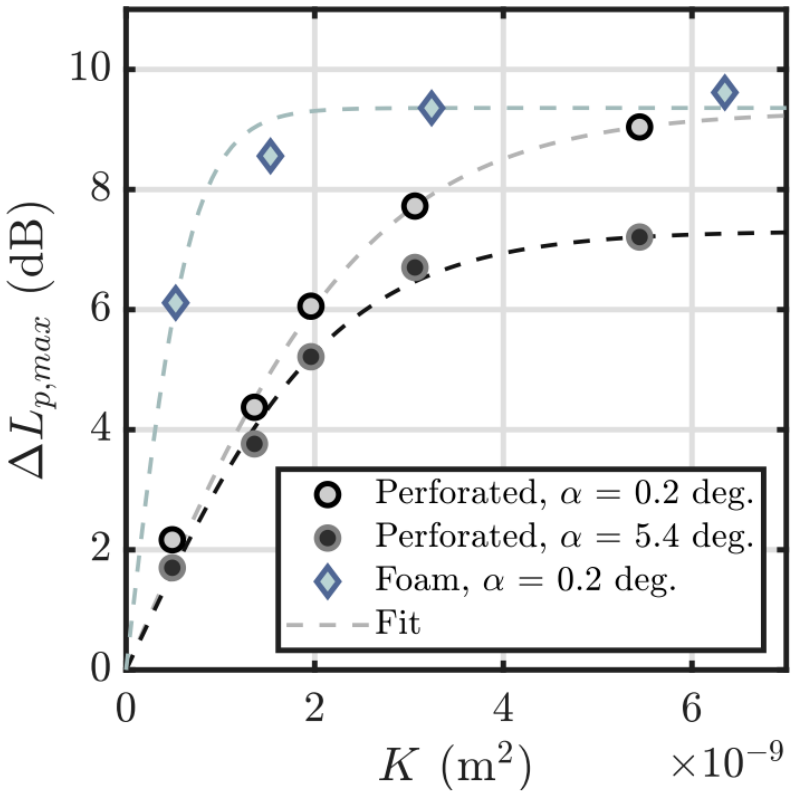

Figure 1.12: Change in maximum noise mitigation with permeability for perforated and metal foam inserts at $\alpha = 0.2^o$ and 5.4^o. [50]

1.5. Objectives of the Research

In the previous sections it has been narrated that passive permeable trailing edge inserts can be effectively utilized to reduce pressure fluctuations originating from turbulent flow over an airfoil. Permeable trailing edges, either in the form of (unstructured) metallic foams or in the form of perforated channel inserts either with a uniform or a tailored distribution of the holes can lead to significant noise reduction. However, this noise reduction comes at the expense of the lift generated. The optimal (value) balance between noise reduction and performance reduction may vary: for land-based wind turbines the reduction of noise levels may be important at night, while during the daytime with a higher background noise level, the performance level may be more important. So, there arises a need to design systems with a variable, actively controlled permeability in the range found to be important in prior aero-acoustic studies.
This research seeks to achieve actively controlled semi-permeable trailing edge inserts with a potential for up-scaling. Following are the research questions-cum-challenges that pertain to the design of an actively controlled semi-permeable trailing edge insert for a full-scale structure:

1. Can an actively controlled system be installed on the trailing edge without major modifications in the aerodynamic frame of the aircraft wing?
   Prior studies (Section 1.3 & 1.4) have focused on passively reducing noise while deploying perforated channel inserts or metal foams. Others have used trailing edge serrations or brushes for achieving the same. An actively controlled system would require the incorporation of actuation system in the wing without disturbing the aerodynamic design of the structure.

2. What is the extent and efficacy of change in permeability and porosity of the perforated insert through an actuation system?

   - Should an actuation system be designed that can control permeability of each individual hole of the porous insert?
     Piezo-electric actuators can be utilized to effectively control individual holes of up to d_h = 0.3 mm [35] in the insert. Such mechanisms provide immense leverage to the user/pilot to manoeuvre the material permeability of airfoil trailing edge based on impact air-velocity and lift-requirements of the aircraft wing. But this method can be complex in its pattern and demand higher technological support for its design.
   - Should the actuation system be designed to control permeability at pre-defined sections of the airfoil insert?
     An alternative approach for achieving variable permeability is the division of trailing edge insert in multiple sections along its chord-wise length and subsequent deployment of individual actuation systems for each section. Such a system can ease the complexity of manufacturing process of inserts. However, flow permeability modulation will decrease.

3. Will an active change in permeability of system affect the noise abatement with respect to different frequency bandwidths to a significant extent?
   Previous studies have shown passive perforated inserts with varying porosity reduce

Overall Sound Pressure Level (OSPL) as well as ΔL_p at multiple frequency bandwidths. Therefore, a replication or improvement of past noise mitigation results through actively controlled perforated inserts will be imperative to this field of work.

Keeping in mind the potential engineering challenges listed above, the targets of this graduation project are as follows:

- Establish a mechanism to control the permeability of perforated channel inserts.
- Create a static set-up in which the permeability as measured in the permeability test rig can be varied from impermeable to permeable with a Flow Permeability value in the range of K $\approx$ 0 - 4x10^{-9} m^2.
- Design and construct a set-up in which the permeability can be varied dynamically and on line. The new device should, in principle, have the potential of being applied to real structures after suitable modifications and refinements.
- Perform pressure drop tests with the newly constructed device and establish the degree of precision and accuracy of the device.
- Analyse the relation between permeability and porosity for the perforated disks and come up with suggestions for further improvement.

2

Mechanics of fluid flow across perforated plates

This chapter covers the determination of characteristics of fluid flow across a permeable medium. The mechanics of transpiration flow and its numerical modelling in Darcy and non-Darcy regimes is imperative to the conception of variation in Flow Permeability (K), Flow Resistivity (R) and Form Factor (C). The following section derives a general model for motion of fluid by method of volume averaging that is subsequently utilized to present a momentum equation that can explain viscous and inertial drags acting on a fluid particle flowing through semi-permeable medium. An expression for prediction of Flow Permeability purely based on the geometry of the perforated model is presented that has been used for permeability comparisons in chapter 5. Also, the equation for pressure losses in a pipe is presented which is instrumental in calculating effective hydraulic diameters later in this report. In the end, the motion of equation exercised by current research to fit pressure drop and flow rate data is presented.

2.1. Modelling of forced fluid motion through pores

Forced convection of fluid across perforations or openings can occur through mechanical means, gravity or natural wind. A quantification of the phenomenon of this transport phenomenon is necessary to understand the relation between fluid motion, its driving forces and the medium of transmission.

Energy is lost when a fluid particles transmit through pores that causes pressure drop over the perforated samples. Generally, the pressure drop across open pores are presented proportional to the fluid velocity squared [2]. Additionally, a linearly dependant term on fluid velocity is added for extreme narrow openings. For porous medium, pressure drop is considered to be proportional to fluid velocity at $\mathrm{Re}_h < 1$ (Darcy's law). For $\mathrm{Re}_h > 1$, a non-linear flow regime is observed and to account for it, a squared fluid velocity term is added to match the experimental results [7, 16].

A mathematical model has been presented by Miguel A.[38] considering the momentum conservation equation and developed in terms of method of volume averaging. The resulting non-linear differential equation has been deemed valid for flows through media with circular pores upto large openings.

2.1.1. The equation of motion by conservation of momentum

For a general flow field, the equation of motion for a single-phase flow is given by:

$$\rho \delta u/\delta t + (\rho u.\nabla)u = -\nabla P + \mu \nabla^2 u \tag{2.1}$$

where u is the vector velocity, P is the total pressure and μ is dynamic viscosity.
Miguel A suggests that the application of eq. 2.1 has several drawbacks as the the equation considers the very local characters of the state variable. A detailed description of the proous media is absent from the equation as it is only valid inside the pores. Hence, the method of volume averaging can be applied to transform eq. 2.1 into an expression that is valid over small volumetric elements representing the medium of study. Four major assumptions can be made for testing the validity of the approach:

- the medium is homogeneous at macroscopic scale
- the solid matrix or the perforated plate is rigid
- the solid matrix and the fluid have no chemical interaction
- isothermal conditions

2.1.2. The equation of motion by method of volume averaging

By averaging the terms of eq. 2.1 in a control volume, as shown in Figure 2.1, through the procedure listed in Appendix A (eq. A.3), the intrinsic phase average is expressed as:

$$< \rho \frac{\delta u}{\delta t} >_i + < (\rho u.\nabla)u >_i = - < \nabla P >_i + < \mu \nabla^2 u >_i \tag{2.2}$$

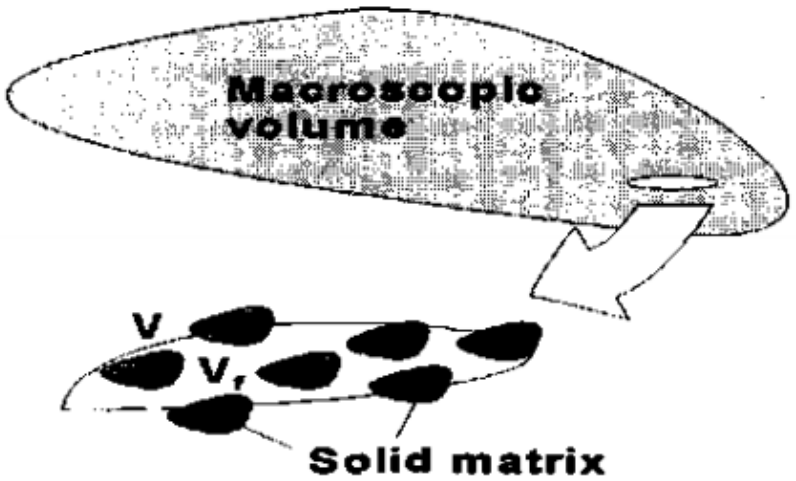

Figure 2.1: Macrscopic domain and averaging volume for solid-fluid system [38]

The porosity, density and dynamic viscosity are assumed to be constants in the averaging volume. In line with eq. A.5 of Appendix A, the first left-hand side term of eq. 2.2 can be transformed as:

$$\rho\frac{\delta < u >_i}{\delta t} + \rho\frac{\delta(\tilde{u})}{\delta t} \tag{2.3}$$

And by eq. A.7 of Appendix A, the second-left had side term of eq. 2.3 becomes:

$$\rho(< u >_i .\nabla < u >_i + \tilde{u}.\nabla < u >_i + < u >_i .V_f^{-1}\int n.\tilde{u}dA + \tilde{u}.V_f^{-1}\int n.\tilde{u}dA) \tag{2.4}$$

The right hand side term is given as:

$$-\nabla < P >_i - V_f^{-1}\int \tilde{P}dA + \mu\nabla^2 < u >_i + \mu V_f^{-1}\int n.\nabla\tilde{u}dA \tag{2.5}$$

The terms $\tilde{P}$ and $\tilde{u}$ need to be represented as a function of flow field to obtain a closed form. So, the spatial deviation is expressed as a linear function of a phase-averaged quantity [56]. Therefore, the spatial deviation of the velocity and pressure are converted into intrinsic averaging velocity, given by:

$$\tilde{u} = \Gamma. < u >_i \tag{2.6}$$

$$\tilde{P} = \mu\Phi. < u >_i \tag{2.7}$$

where Γ and Φ are tensors that relate the intrinsic phase average velocity to spatial deviation of velocity and pressure, respectively. Substituting the above representations in the eq. 2.2 again yields,

$$\begin{aligned}\rho\frac{\delta < u >_i}{\delta t} + \rho\frac{\delta(\Gamma. < u >_i)}{\delta t} + \rho[< u >_i .\nabla < u >_i + \Gamma. < u >_i .\nabla < u >_i + \\ < u >_i . < u >_i .(V_f^{-1}\int n.\Gamma dA + V_f^{-1}\Gamma.\int n.\Gamma dA)] \\ = \\ -\nabla < P >_i + \mu\nabla^2 < u >_i + \mu < u >_i (V_f^{-1}\int n.\nabla\Gamma dA - V_f^{-1}\int I.\Phi dA) + \\ \mu\nabla < u >_i (V_f^{-1}\int n.\Gamma dA)\end{aligned} \tag{2.8}$$

where I is the unit tensor[38].
The values of spatial deviation of velocity and pressure are minuscule compared to average values of intrinsic phase so Γ and Φ can be considered as small parameters. As $< u >_i \rightarrow \Gamma < u >_i$ and $< u >= \epsilon < u >_i$, where ϵ is the porosity (Appendix A.4), eq. 2.8 becomes:

$$\begin{aligned}\frac{\rho}{\epsilon}\frac{\delta < u >}{\delta t} + \frac{\rho}{\epsilon^2} < u > .\nabla < u > \\ = \\ -\nabla < P >_i + \mu < u > .[\frac{1}{\epsilon}(V_f^{-1}\int n.\nabla\Gamma dA - V_f^{-1}\int I.\Phi dA)] - \rho < u > . < u > .[\frac{1}{\epsilon^2}(V_f^{-1}\int n.\Gamma dA)] + \\ \mu\nabla < u > .[\frac{1}{\epsilon}(V_f^{-1}\int n.\Gamma dA] + \frac{\mu}{\epsilon}\nabla^2 < u >\end{aligned} \tag{2.9}$$

Eq. 2.9 is the key equation derived from volume averaging method that accounts for both: inertia effects ($\frac{\rho}{\epsilon^2} < u > .\nabla < u >$) and viscous effects ($\frac{\mu}{\epsilon}\nabla^2 < u >$) as well as newer terms accounting for effects of interaction between fluid and the matrix:
$(\rho < u > . < u > .[\frac{1}{\epsilon^2}(V_f^{-1}\int n.\Gamma dA)])$, $(\mu\nabla < u > .[\frac{1}{\epsilon}(V_f^{-1}\int n.\Gamma dA])$ and
$(\mu < u > .[\frac{1}{\epsilon}(V_f^{-1}\int n.\nabla\Gamma dA - V_f^{-1}\int I.\Phi dA)])$

2.1.3. Extrapolation of model for Darcy domain and Forchheimer domain

If the flow is considered to be in-compressible ($\nabla < u >= 0$) and the volume of solid matrix is considerably larger that volume occupied by fluid ($\frac{\mu}{\epsilon}\nabla^2 < u >\approx 0$)[33], then the second left-had side term and last right-hand side term of eq. 2.9 can be neglected. So a steady flow is defined by:

$$\rho < u > . < u > .[\frac{1}{\epsilon^2}(V_f^{-1}\int n.\Gamma dA)] = -\nabla < P >_i +\mu < u > .[\frac{1}{\epsilon}(V_f^{-1}\int n.\nabla\Gamma dA - V_f^{-1}\int I.\Phi dA)] \quad (2.10)$$

Darcy domain

In Darcy domain, the velocities are very small so the squared fluid velocity term can be considered negligible compared to linear velocity term, so the eq. 2.10 can be given as:

$$\mu < u > .[\frac{1}{\epsilon}(V_f^{-1}\int n.\nabla\Gamma dA - V_f^{-1}\int I.\Phi dA)] = \nabla < P >_i \quad (2.11)$$

The term in square brackets is the viscous resistance force due to momentum transfer at matrix-fluid interface and is defined as [33, 56]:

$$\frac{1}{\epsilon}(V_f^{-1}\int n.\nabla\Gamma dA - V_f^{-1}\int I.\Phi dA) = \frac{1}{K} \quad (2.12)$$

where K is the permeability of matrix (m^2).
Permeability can be defined as the ability of a medium to allow the transmission of fluid across it. According to kinetic gas theory [33], permeability is the reciprocal of collision frequency particles against the solid matrix and kinematic fluid viscosity.

Forchheimer domain

In the Forchheimer domain [7], the rate of change of differential pressure or pressure gradient is proportional to linear expression of fluid velocity and a squared velocity term (eq. 2.10). The linear expression is defined by the eq. 2.12 while the expression relating to the inertial effects (or non-linear effects) of the pores is given as [13, 16]:

$$\frac{1}{\epsilon^2}(V_f^{-1}\int n.\Gamma dA) = \frac{Y}{\sqrt{K}} \quad (2.13)$$

where Y is a porous inertia factor.

2.2. Numerical Modelling of Transpiration flow

The governing equations for a steady, isothermal, in-compressible and laminar fluid flow through a perforated plate are given by [6]:

$$\nabla . U = 0 \tag{2.14}$$

$$(U.\nabla)U = -\frac{1}{\rho}\nabla P + \nu\nabla^2 U \tag{2.15}$$

where ν is kinematic viscosity. The gravitational effects are considered to be negligible. Fig. 2.2 displays the configuration of flow through perforations in a plate.

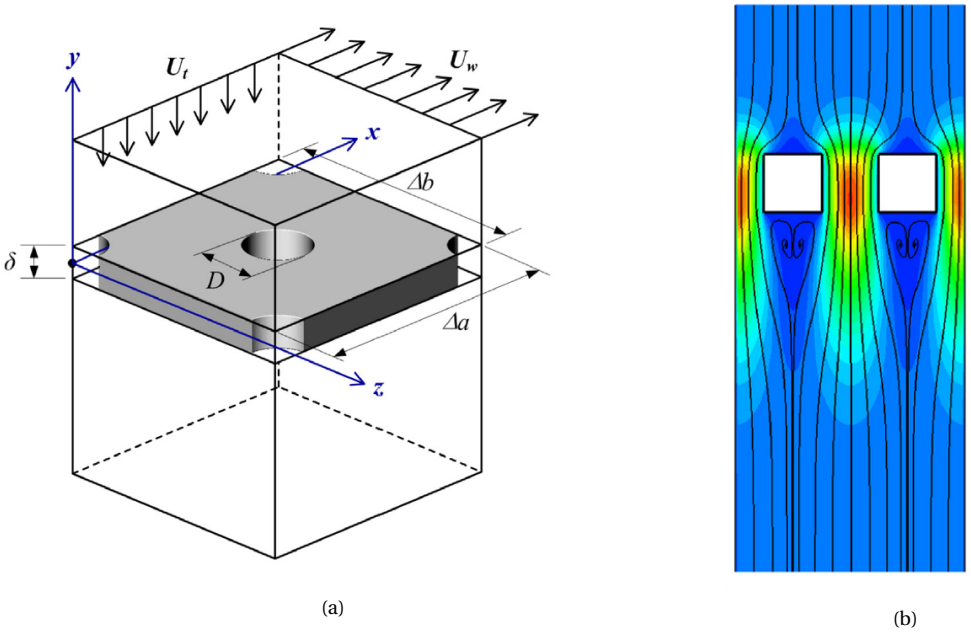

(a) (b)

Figure 2.2: The plate considered for DNS calculations by Bae; (a): Schematic of a perforated plate with cylindrical pores; and (b): Transpiration flow pattern [6]

The domain of the computational model extends 10D upstream and 20D downstream and the cross-section considered is Δa x Δb.

2.2.1. Expression for Darcy-Forchheimer drag

The method of Volume Averaging (Section 2.1) is also utilized by Vafai et al [55] to establish a momentum equation for interstitial flow in porous media, popularly know as Brinkman-Forchheimer equation. It is expressed as:

$$-\nabla P = \frac{\mu}{K}\bar{U} + \rho C|\bar{U}|\bar{U} - \mu_e\nabla^2\bar{U} \tag{2.16}$$

where C is the Form factor or non-Darcy coefficient, ρ is fluid density and μ_e is the effective viscosity of medium. This expression is considered to be a more complete version of the general flow equation as it includes the Brinkman term (diffusion term) accounting for boundary effect and the Forchheimer term (non-linear drag term) accounting for the inertial effects as well. Eq. 2.16 can also be expressed for a Darcy-Forchheimer drag, given by

[34]:

$$\frac{D^2}{K} + \epsilon CDRe_h = \frac{\Delta P D^2}{\mu \delta U_t} \tag{2.17}$$

where ΔP is differential pressure across plate (pressures difference between inlet and downstream of domain),ϵ is porosity and U_t is the superficial velocity (uniform).
The hole-level Reynolds number utilized in eq. 2.17 is defined as :

$$Re_h = \rho U_t \frac{D}{\mu \epsilon} \tag{2.18}$$

After performing computational analysis of transpiration flow through application of eq. 2.17, Bae et al [6] suggested that with increase in plate thickness to hole diameter ratio and porosity, the permeability (K) also increases but the form factor (C) decreases. Numerical modelling also displayed that pressure drop increases with increasing plate thickness while it goes down with increasing porosity. The Darcy regime considered for the transpiration flow across a perforated plate are at $Re_h < 5$ where inertial effects are almost absent and flow can be modelled with just linear terms. The Forchheimer domain is at $Re_h > 5$ where relation between pressure drop and superficial velocities deviates from a linear dependence or Darcy's law.

2.2.2. Expression for Flow Permeability based on geometric parameters

The directional flow permeability of the perforated plate depicted in Figure 2.2 can be predicted numerically based on results from Bae et al [6]. Therefore, neglecting the influence of hole arrangement and expressing the permeability only in terms of geometric parameters, K is defined as:

$$K_{geometric} = \frac{\epsilon D^2 \delta}{32\delta + 15D} \tag{2.19}$$

The flow permeability expression is proposed and valid for only uniform flow channels with no internal tortuosity, i.e., $\Gamma = 1$ and at hole-level Reynolds number $Re_h < 25$.

2.3. Pressure losses due to flow in pipe

The pressure losses that happen with fluid flow in a pipe or closed conduits due to resistance or friction are accounted for in the Darcy-Weisbach equation. The fluid friction between two locations in a straight pipe or duct can be quantified with empirical extension of Bernoulli principle of energy equation given as [8]:

$$h_l = (\frac{V_1^2}{2g} + \frac{p_1}{\rho g} + z_1) - (\frac{V_2^2}{2g} + \frac{p_2}{\rho g} + z_2) \approx (\frac{p_1}{\rho g} + z_1) - (\frac{p_2}{\rho g} + z_2) \tag{2.20}$$

where h_l is the fluid friction or head loss between locations 1 & 2, V is the average superficial velocity, g is the acceleration of gravity, p is the fluid pressure, ρ is the fluid density and z is the elevation of pipe.
Subsequently, the equation for calculating head-loss, as proposed by Weisbach, is given as:

$$h_l = \frac{fL}{D} \frac{V^2}{2g} \tag{2.21}$$

where L is the pipe length, D is the pipe diameter and f is the friction factor [8]. Equation 2.21 can also be re-written for pressure loss or major loss as:

$$\Delta p_{majorloss} = \frac{fL}{D}\frac{\rho V^2}{2} \tag{2.22}$$

Equation 2.21 and 2.22 only predict the losses due to friction on the pipe wall and effect of fluid viscosity and doesn't cover the minor losses at inlets, elbows or other fittings. The equation is valid for fully developed, steady state and in-compressible flow. The friction factor f is dependant on the fluid flow regime and is given as [8]:

$$\textbf{Laminar regime (Re}_p\textbf{ < 2300)} : f = \frac{64}{Re_p} \tag{2.23}$$

$$\textbf{Transition regime (2300<Re}_p\textbf{<4000)} : \frac{1}{\sqrt{f}} = 1.14 - 2log(\frac{h_{rough}}{D} + \frac{9.35}{Re_p\sqrt{f}}) \tag{2.24}$$

$$\textbf{Turbulent regime (Re}_p\textbf{>4000)} : \frac{1}{\sqrt{f}} = 2log(Re\sqrt{f}) - 0.08 \tag{2.25}$$

This research work deals with fairly Laminar regime in the pipe-level fluid flow of Re_p < 2380, therefore, eq. 2.23 has been generally utilized in later calculations.

2.4. Expression for experimental calculations

In this study, a non-linear least square fit function is employed to calculate the flow permeability, flow resistivity and form factor of the permeable specimen. The Hazen-Dupuit-Darcy equation [42] given by eq. 2.26 is fit with experimentally recorded data of velocity of fluid flow and subsequent differential pressure across the sample.

$$\frac{\Delta p}{\delta} = \frac{\mu}{K}U_t + \rho C {U_t}^2 \tag{2.26}$$

where δ is thickness of sample, ρ is fluid density, μ is the dynamic viscosity and U_t is the superficial velocity or velocity at inlet. $\frac{\Delta p}{\delta}$ is the pressure drop normalized to the thickness of the sample δ. Here K is the permeability of the material which correlates to the pressure drop across the sample due to viscous effects and C is the form factor that correlates to pressure drop due to inertial effects. The superficial velocity is measured as $U_t = \frac{Q}{A}$ where Q is the volumetric flow rate of channel (m^3/s) that is inputted to the permeability rig in the form of linear incremental mass flow rate (Kg/s) and A is the cross-section area of the channel (m^2). The resistivity of the of the sample can be theoretically defined as follows [19, 24]:

$$R = \frac{\mu}{K} \tag{2.27}$$

where μ is obtained via Sutherland's law [54] as:

$$\mu = \frac{C_1 T^{3/2}}{T + S} \tag{2.28}$$

where T is the absolute temperature, C_1 = 1.458$x10^{-6}$ Kg/ms-$\sqrt{K}$ for air and S = 110.4 K. At room temperature, T = 293.1 K which leads to μ = 1.813 x 10^{-5} Kg/m-s.

2.5. Summary of Mechanics of transpiration flow

This chapter presented the background knowledge employed in this research to characterize transpiration flow across the perforated specimens designed for turbulent boundary layer reduction. The volume averaging method was introduced to designate the linear and non-linear effects in the Darcy and Forchheimer domain and its relation to flow permeability of matrix, albeit for a steady & in-compressible fluid flow through perforated disks. The derived expressions, further extrapolated to interstitial flow in porous media, rendered an illustration for the Darcy-Forchheimer drag that is imperative to characterize the dependence of viscous and inertial drags on geometry of the perforated inserts. The relations of hole depth -to- diameter δ/D of inserts and porosity ϵ with the Flow Permeability K and Form Factor C, as discussed in this chapter, are also demonstrated experimentally as part of this study. Also, the Darcy-Weishbach equation, introduced in this chapter has been exercised later in this study to estimate hydraulic diameter for a semi-closed hole orientation. This strategy produced close estimates of effective porosity, after neglecting minor losses in the fluid flow.

Therefore, chapter 2 suggests an engineering framework that can be applied to describe the transpiration flow across perforated plates, thereby, assisting in the design of effective semi-permeable inserts for an airfoil.

3

Experimental Set-up

This chapter displays the apparatus used for the pressure-drop experiments conducted as part of this research. It briefly explains the surface geometry design of the perforated disks along with the purpose behind splitting permeability experiments into two phases - static and dynamic configurations. The chapter also includes an assembly of the perforated disks for each configuration and general schematics of hole closure orientations for a Middle-Disk Shift mechanism. In Section 3.4, the chapter discusses the design parameters for the selection of actuation mechanism in this research as well as the challenges faced in manufacturing the CNC milled actuation mount.

3.1. Permeability Test Rig

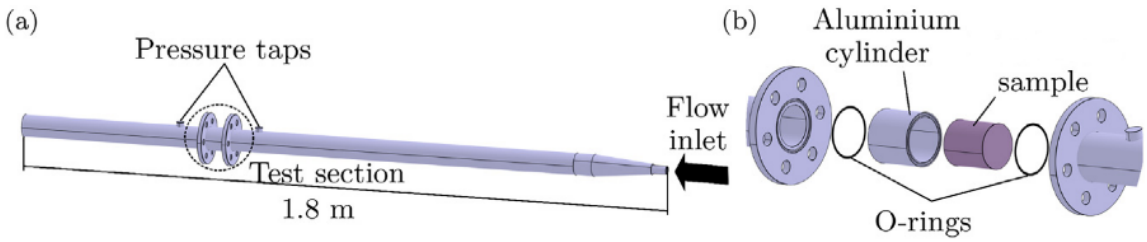

Figure 3.1: (a) Sketch of the rig used to characterize the permeability/resistivity of the perforated samples during the static configuration tests; (b) Detail of the test section [49]

The permeability measurements were done using the apparatus shown in Figure 3.1. The rig was specifically built for this purpose and was supplied by air from an external source at 10 bar. Two pressure taps were placed 5 cm upstream and downstream of the test section. Both the pressure taps could be connected to two different sensors: Mensor 2101 differential pressure sensor (range: -1.2 to 15 kPa; accuracy: ±2 Pa) and Honeywell differential pressure sensor (range: < 200 kPa). The volumetric flow rate was controlled using an Aventics pressure regulator and measured by a TSI 4040 volumetric flow meter (range: 0 - 2.5 m/s; accuracy: 2% of reading) located upstream of the pipe.
Figure 3.1(b) displays the detailed sketch of the test section in the rig. An aluminium cylinder of internal diameter 55 mm and outer diameter 65 mm was used to hold the cylindrical

perforated samples in place. The aluminum cylinder was fitted air-tight into the two pipes of the rig through a couple of O-rings and then clamped with four bolts. The apparatus also had a mechanical control valve to control inlet pressure of the rig. It was observed that pressure losses of the magnitude of 0.8 bar were present upstream of the apparatus. This loss was delegated to the fluid pressure losses due to flow through multiple control valves and a flow meter before entering the actual permeability rig. All test were performed at inlet pressure from mechanical control valve at 2 bar to maintain uniformity.

3.2. Perforation arrangement of 3-D printed disks

The perforated disks for the pressure-drop tests in both static and dynamic configurations were 3-D printed via stereolithography (SLA) and the polymer used was R5. It is liquid photopolymer that gives rise to robust, precise, and functional parts [12]. Appendix B catalogues the material properties of the polymer.

The 3-D printed disks had perforated cylindrical channels that were arranged in a 60^0 staggered hole arrangement as shown in Figure 3.2. All the holes were equidistant and the perforated plates were printed for two hole spacing's, l_h = 1.5 mm and 3 mm. The diameter of holes was kept constant at d_h = 0.8 mm. In the past researches on trailing edge inserts, employment of similar hole arrangements [50] was done to ensure that channels were open after printing process and to avoid low-frequency acoustic tones during noise testing. Since this research is an advancement of the work previously completed on passive trailing edge inserts, superficial hole arrangement patterns were kept similar. The porosity for a 60^0 staggered hole arrangement is given by:

$$\epsilon = \frac{\pi d_h^2}{2\sqrt{3} l_h^2} \tag{3.1}$$

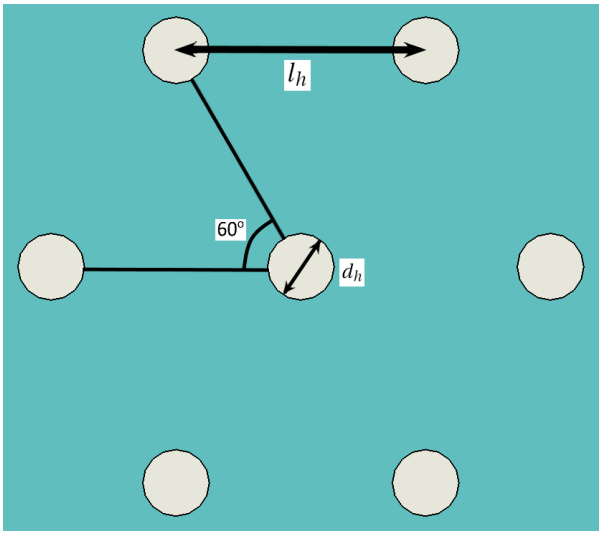

Figure 3.2: (a) Sketch of the rig used to characterize the permeability/resistivity of the perforated samples during the static configuration tests; (b) Detail of the test section

3.3. Static Configuration

The first phase of experiments, that is, for static configuration were conducted to authenticate the extent of application of a middle-disk shift mechanism which could potentially modify the overall flow permeability of the perforated system. Since, it was already established that controlled changes in permeability of a system directly alter its noise attenuation characteristics (Figure 1.2), proceeding with static configuration tests to gauge the extent of middle-disk shift required by the system for effective flow permeability variations was imperative. The tests were conducted on two sets of 3-D printed samples as explained in the following section.

3.3.1. Design of perforated samples for static configuration

Each cylindrical sample was divided into three different disks - top, middle and bottom disk. The top and bottom disk had the following dimensions - diameter: 55 mm & thickness: 25 mm. The middle disk had an eccentricity of 0.8 mm along with diameter: 55 mm & thickness: 10 mm. The middle disk was given the eccentricity in order to accommodate for the lateral shift during experiments. Due to this eccentricity, the diameter for middle disk effectively became: 54.2 mm in the lateral direction (x-axis) and 55 mm in the transverse direction (y-axis). Figure 3.3 and Figure 3.4 display the top disk, middle disk and bottom disk of l_h = 1.5 mm and 3 mm sample, respectively.

As shown in both the figures, two holes of R1.25 were drilled in opposite sides of the disk to install tightening bolt in order to keep the disks together under high air-pressure. For top and bottom disks, space for incorporating screw head on the top (R2.0 shown in Figure 3.3(a) and 3.4(a)) and nut in the bottom (Figure 3.3(c) and 3.4(c)) was also given. The middle-disks had bolt holes with a lateral extension of 0.8 mm in the middle to accommodate for lateral shift of middle disk. And the cause of this middle-disk shift mechanism was the orientation pin holes drilled on the other two sides of the disk (x-direction). 9 orientation pin holes, on either side, were responsible to take the perforated sample from 0% closed hole orientation to 100% closed hole orientation or 0 mm to 0.8 mm shift with a step size of 0.1 mm. At a time, two pins were installed, one on each set of orientation holes, to lock the orientation and minimize any uncontrolled motion or slippage of middle-disk during experiments at high pressure. The following sections help visualize the mechanism more understandably.

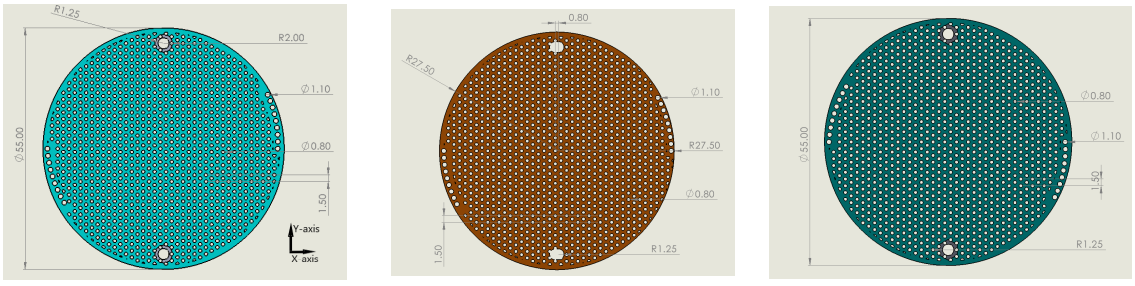

(a) (b) (c)

Figure 3.3: 3-D printed Perforated disks for l_h = 1.5 mm hole spacing; (a): Top disk; (b) Middle disk; and (c) Bottom disk (all dimensions are in mm)

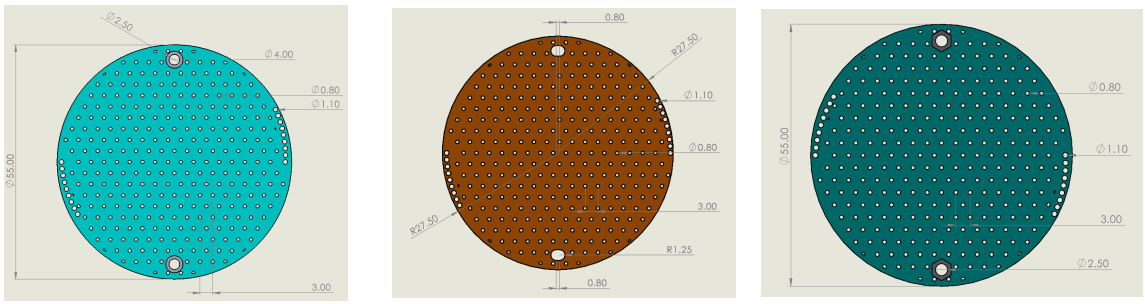

(a) (b) (c)

Figure 3.4: 3-D printed Perforated disks for l_h = 3 mm hole spacing; (a): Top disk; (b) Middle disk; and (c) Bottom disk (all dimensions are in mm)

3.3.2. Assembly of static configuration system

Figure 3.5 presents the assembled perforated disks for both hole spacing. The orientation pins, on each side, are visible which are responsible for laterally shifting the middle disk with the help of calculatively drilled orientation holes on either side. The tightening bolts, with their heads placed inside the sample, are also visible. The three-disk assembly was covered with a white acrylic paste from the sides before positioning it inside an aluminium cylinder, as shown in Figure 3.1(b). The acrylic paste was used to minimize air-leakage from the sides of the sample. Also, the middle-disk was rubbed with Dow Corning®high vacuum grease to better seal/mate the surface to the top and bottom disks and reduce surface friction.

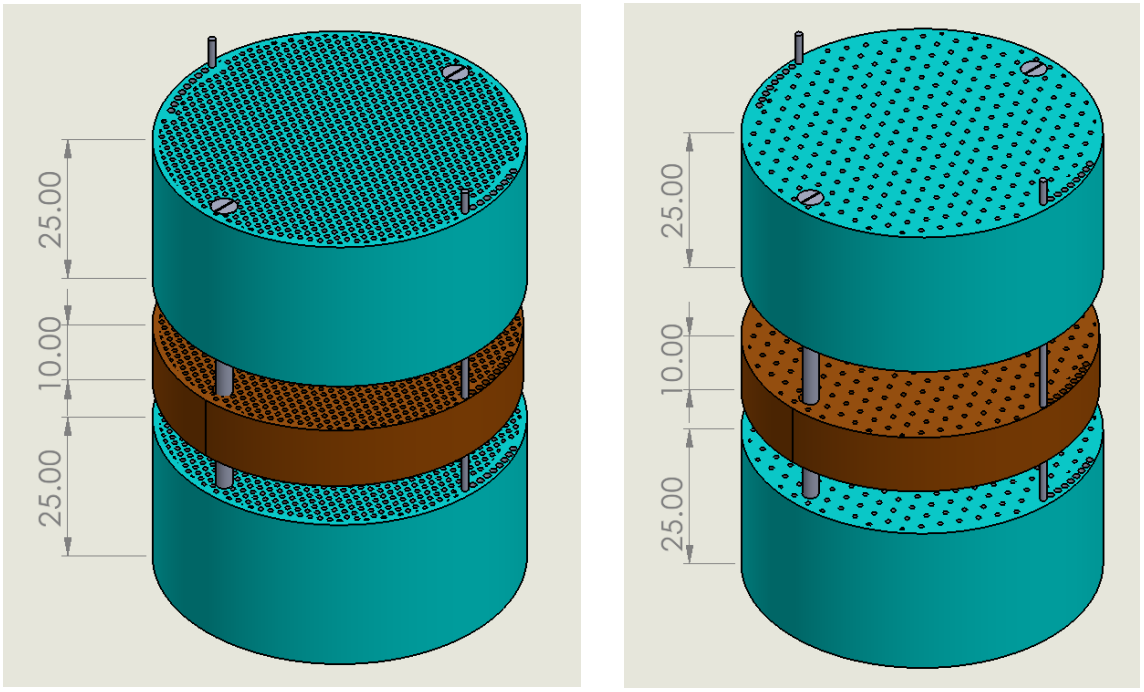

(a) (b)

Figure 3.5: Assembly of the three perforated samples; (a): l_h = 1.5 mm sample; and (b): l_h = 3 mm sample (all dimensions are in mm)

3.3.3. Schematics of middle disk shift mechanism

Figure 3.6 is a representative image to annotate the orientation holes. Each set of orientation holes, on either side, represent a single perforated channel hole closure orientation. For example, in order to shift the middle-disk by 0.4 mm, orientation pins had to be placed in 50% closed hole orientation hole on either side. The shift-steps are at an increment of 0.1 mm.

Figure 3.7 shows the bird's eye view of the middle-disk shift mechanism for all the orientations. The hydraulic diameter calculated from this view later came to be know as D_{BEV}, as explained in section 5.1.

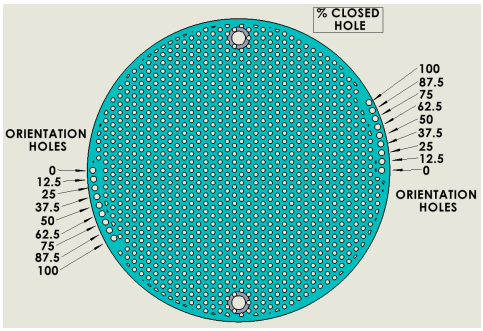

Figure 3.6: Representation of perforated channel hole closure for each orientation hole

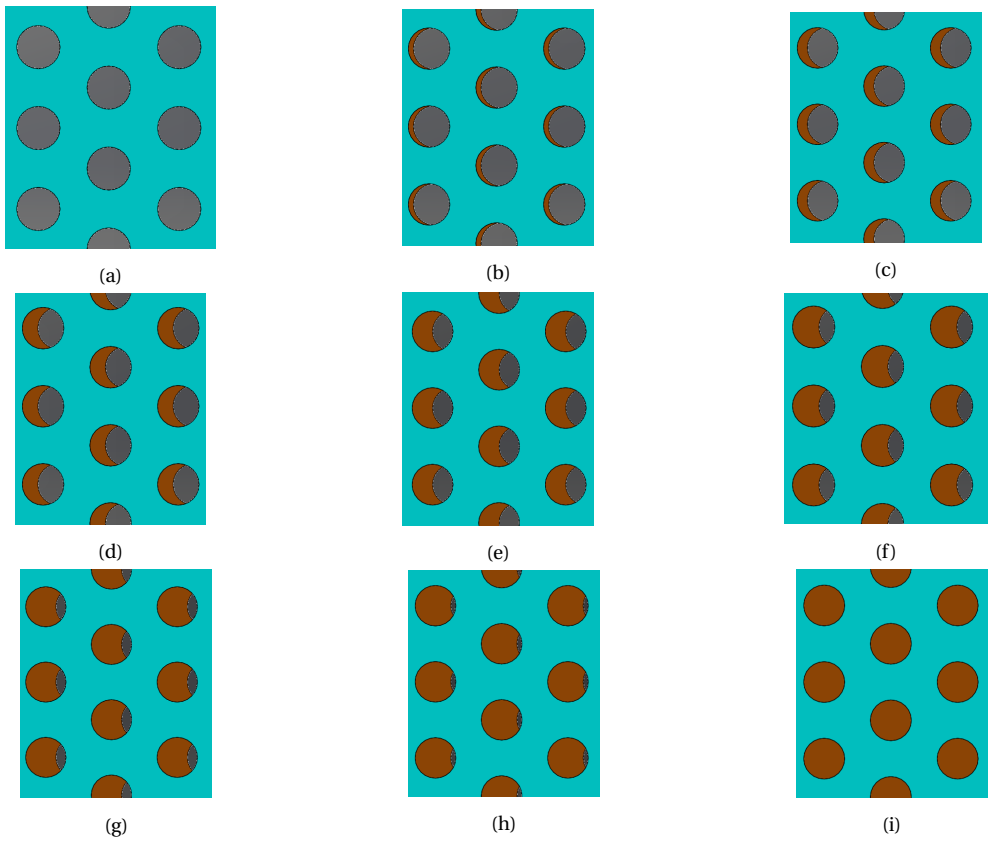

Figure 3.7: The Bird's Eye View of hole closure for Middle-Disk Shift mechanism; (a): 0% closed;(b): 12.5% closed;(c): 25% closed;(d): 37.5% closed;(e): 50% closed;(f): 62.5% closed;(g): 75% closed;(h): 87.5% closed;(i): 100% closed;

3.3.4. Microscopic images

The perforated disks were polished at the automatic polishing machine, in the Faculty of Aerospace Engineering, with sand paper of grit size: # 1000 to # 4000, to achieve a smooth surface for easy motion of middle disk as well as air-tight mating of the surfaces together. Figure 3.8 shows shows the microscopic images of the perforated plates for both samples, post-polishing. The dimensions of the hole spacing l_h and diameter d_h were within an accuracy of: $\pm$ 35 μm.

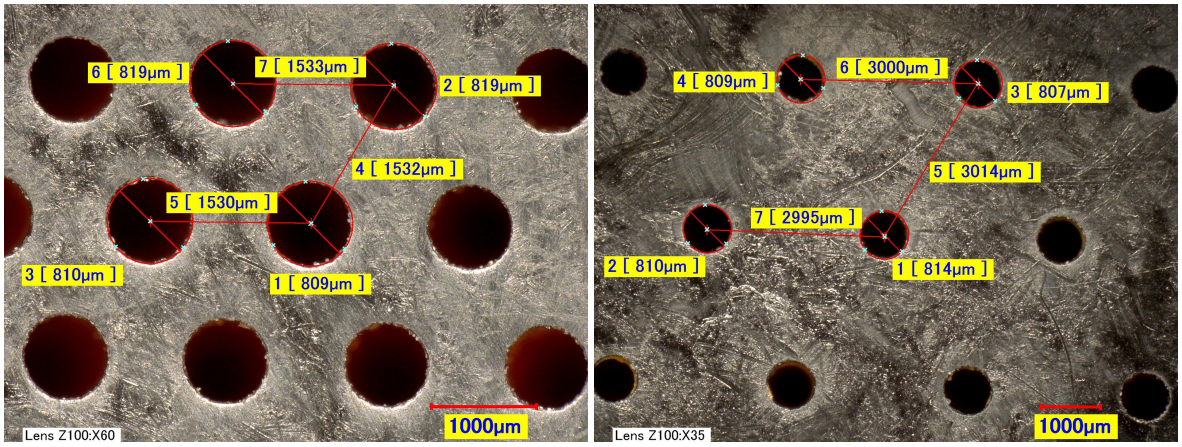

(a) (b)

Figure 3.8: Microscopic images of perforated disks post-polishing; (a): l_h = 1.5 mm sample; and (b) l_h = 3 mm sample

The results obtained from static configuration experiments are included in chapter 4: Results. Post-completion of static phase experiments, a comprehension of the viability of Middle-Disk Shift mechanism and its extent was formed. This new found knowledge was taken further to the second phase of experiments, that is, dynamic configuration. The following section explains the motive, challenges and design of the dynamic set-up, in detail.

3.4. Dynamic Configuration

The purpose of dynamic tests was to provide a proof of concept of actuation of the Middle-Disk Shift mechanism. After manually shifting the middle disk to obtain varying permeabilities and air-flow resistivities over the course of static configuration tests, a system was created to actively control the permeability of the test sample. For this, results from static configuration were studied to come up with a relevant actuation system that can fulfill the requirements of a practical and reliable shift-disk mechanism.

3.4.1. Selection of Actuator

An actuation system had to be designed for shifting the middle disk of the perforated sample. For this, several actuation systems including micro-pneumatic actuator[9], vacuum actuated muscle inspired pneumatic actuator[57], electrically tunable dielectric elastomer[35] were researched. Table 3.1 shows the main criteria for selecting an actuator:

Table 3.1: Minimum requirement of parameters for an actuator

Parameter	Requirement	Unit
Stroke	>500	μm
Design resolution	<5	μm
Linear velocity	>1	mm/s
Drive screw type	Lead screw	-
Drive tip	Non-rotating	-
Linear force (push/pull)	>50	N
Operating temperature	-10 to 40	^{o}C
Mass	<1	Kg

Considering the above mentioned parameters, it was observed that micro-pneumatic actuator had a low linear force of 10 mN @ 150 Hz, vacuum actuated muscle inspired pneumatic actuator had poor accuracy due to it being an air-powered system and electrically tunable dielectric elastomer had a low stroke of <50 μm as well as hole spacing requirement of l_h >5 mm. Keeping these parameters and short-comings of the researched actuation systems in mind, a linear stepper motor M-229.26S, from PI motion | positioning was selected along with its controller C-663.12 [41]. The specifications of parameters of the actuator and the controller are provided in the Appendix C. PI MikroMove was used to control the motion of the motor and receive feedback on its live location. Figure 3.9 displays the drawings of M-229.26S actuator with its dimensions.

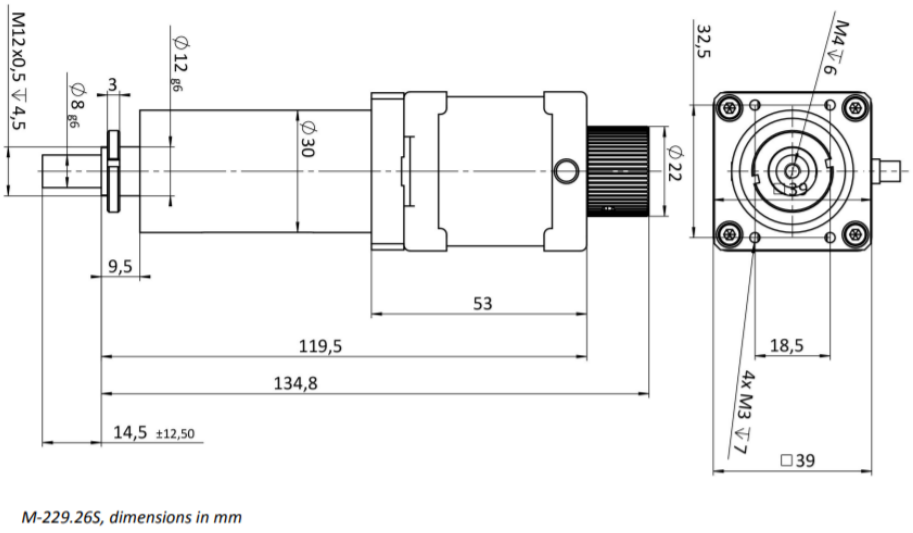

Figure 3.9: M-229.26S Linear Stepper Motor from PI motion|positioning [41]

3.4.2. Design of actuator mount

The next step was to replace the aluminium cylinder used for encasing static configuration samples, as shown in Figure 3.1(b), with a custom-made mount that can incorporate the actuator along with the perforated disks and can be accurately positioned in the permeability test rig, as shown in Figure 3.1(a). The design had to be air-leak proof and provide easy installation/un-installation of perforated disks along with the actuator. It was also imperative to keep the top and bottom disks in place, that is, stationary so that the overall

alignment of the perforated channels doesn't change in an uncontrolled fashion. Figure 3.10 shows a half-sliced SolidWorks model of the custom made metal block that acted as an actuator-cum-sample mount for the permeability rig experiments. It was milled with a 6-axis CNC machine with appropriate tolerances. The actutor mount was made from two half-sliced pieces of model shown in following figure to ease the mounting of stepper motor with the perforated samples. The figure includes numbering around important features of the mount. They are as follows:

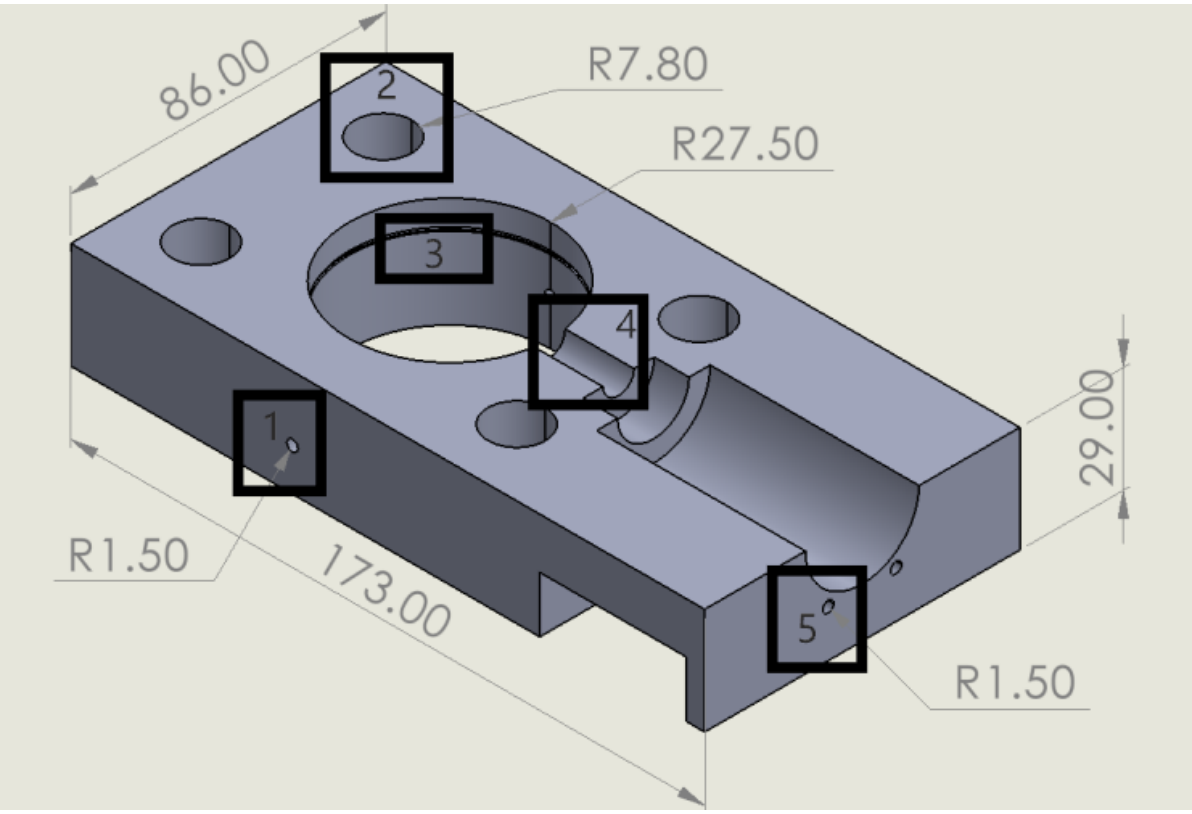

Figure 3.10: Half-sliced CAD model of actuator mount (all dimensions are in mm)

1. *Block Orientation holes*: Two threaded block orientation holes on opposite sides of the block were drilled of R1.5 mm. Their purpose was to hold the top and bottom perforated disks in place through screws. Since alignment of holes was core to the set-up, the orientation holes were played an imperative to the precise arrangement of perforated channels.

2. *Clamping holes*: Four un-threaded holes ran through the two half-sliced metal blocks. They provided space for clamping screws with nuts on both sides of the clamp. They were used to hold the actuator mount block in place and connect it to the apparatus (Figure 3.1 displays the clamping screws in the permeability rig).

3. *Internal O-ring groove*: An internal groove was made on each block to position an O-ring of dimensions: 54 x 2 mm in it. The depth of the groove was 1.7 mm and they were positioned at a distance of 6.75 mm from the middle surface. O-rings were installed right below the junction of bottom disk and middle disk to minimize air leakage from the sides of perforated sample during actuation of middle disk. In the

top half of actuator mount, the O-ring was place just above the junction of top disk and middle disk.

4. *Actuator push-rod casing*: The casing was designed to give appropriate clearance for the placement of stepper motor. The region around push-rod was given extra clearance, of 1 mm, for the easy back and forth movement of the push-rod. Two small O-rings of dimension: 18 x 1 mm, were installed on the body of actuator, through a metal billet, to impede the leakage of air from the this region. The grooves of the small O-rings were made on the billet which was then installed over the stepper motor.

5. *Actuator installation holes*: Four un-threaded holes (two on each block) were made to install the actuator on the mount block. Figure 3.9 shows the four threaded holes built in the stepper motor that were aligned with installation holes of the mount block.

Figure 3.11 shows the complete actuator mount with both blocks attached together. Like the last figure, it also includes important features of the mount. They are as follows:

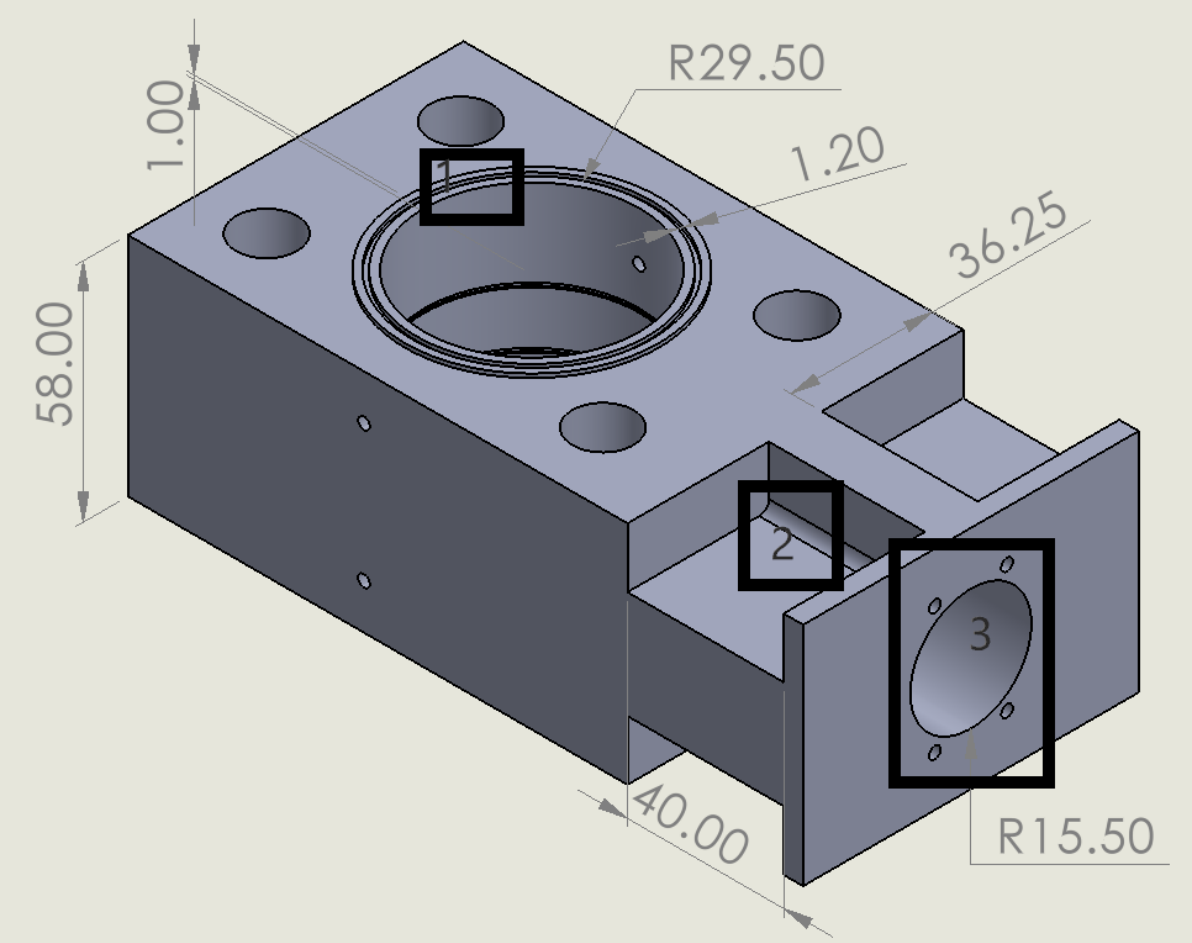

Figure 3.11: Full CAD model of actuator mount (all dimensions are in mm)

1. *External O-ring groove*: The two O-ring grooves (one each on either mount block) were created at an elevation of 1 mm from the top surface and bottom surface of the block. These O-rings were mainly used to seal the junction between actuator mount and the permeability rig.

2. *Efficient weight reduction and space creation*: A space of 40 mm depth and 36.25 mm width was cut out from the block. It served dual purpose- (a) reduced overall weight of the metal block and (b) provided space for the use of allen keys to tighten screws in the actuator installation holes. Fillets on each side were made for easy access of the screws when using allen keys.

3. *Stepper motor's rear side*: Almost half of the stepper motor/actuator's rear body hung out of the mount. The wire connecting stepper motor to the controller was attached to the aft end of the motor, therefore, it had to be kept outside the actuator mount.

3.4.3. Design of perforated samples for dynamic configuration

The perforated disks for the dynamic configuration were also made from R5 thermoset photo-polymer. They were 3-D printed via the stereolithography (SLA) process. The disks were perforated with 0.8 mm pore size (d_h) and line spacing (l_h) of 1.5 mm and 3 mm.
Sample preparation

- *Polishing*: The common surfaces of the disks, that is, mating surfaces were polished in a similar fashion as the static setup disks, with #1000, #2000 and #4000 grit size in the ascending order, respectively. An automated polishing machine was used to provide even and smooth finish to the surface planes.

- *Waxing*: The surfaces were subsequently waxed with a Dow Corning®high vacuum grease. It was done to improve the mating of common sliding surfaces better and also to ease the motion while reducing friction.

- *Turning on lathe*: The top and bottom disks of both samples were turned on lathe and their diameters were reduced to 54.6 mm. The lathe was applied till a height of 11 mm for both the disks. This was done to ease the installation of top and bottom disks in the actuator mount with internal O-rings (54 x 2 mm) attached.

Modelling of perforated disks

Figure 3.12 and Figure 3.13 display the l_h = 1.5 mm and 3 mm perforated disks with their top view, side view and front view. The lathed section for the top and bottom disks are visible in each figure with a reduced diameter ϕ = 54.6 mm. The *Block Orientation Holes*, as displayed in Figure 3.10, were also drilled for the top and bottom disks for diameter ϕ = 3 mm and depth of 2.5 mm. The middle disk for both the samples had a M4x0.5 threaded socket inserted with a depth of 6.4 mm. The threaded socket was used to connect the disk with the stepper motor push-rod via a threaded stud, further visualized in Figure 3.14.

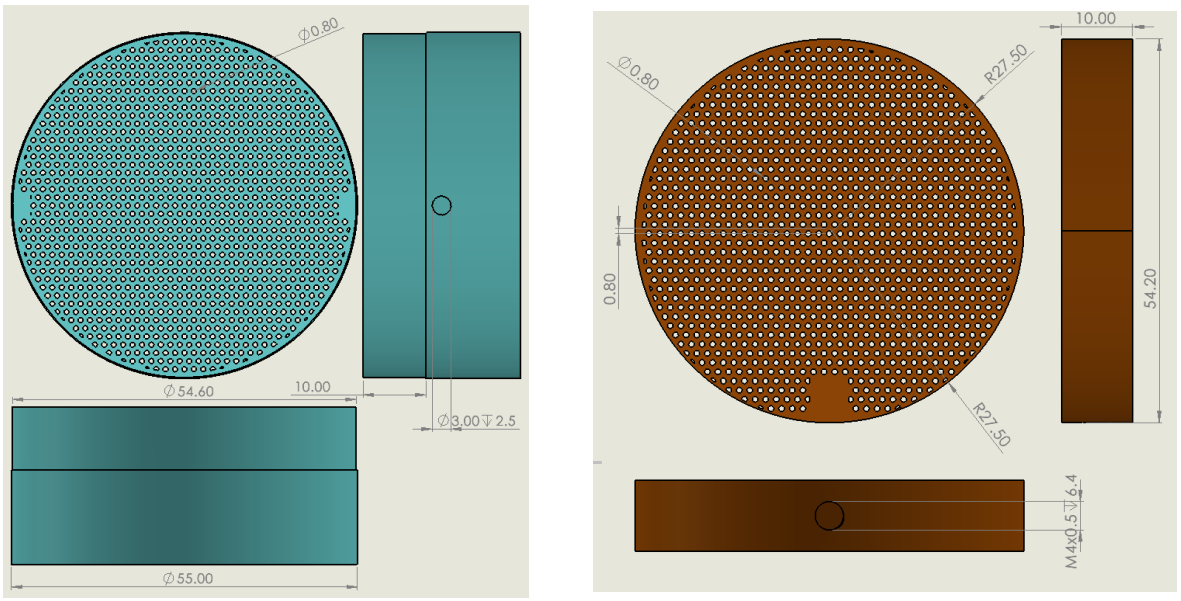

(a) (b)

Figure 3.12: 3-D printed Perforated disks for l_h = 1.5 mm hole spacing; (a) Top and Bottom disk; and (b): Middle disk (all dimensions are in mm)

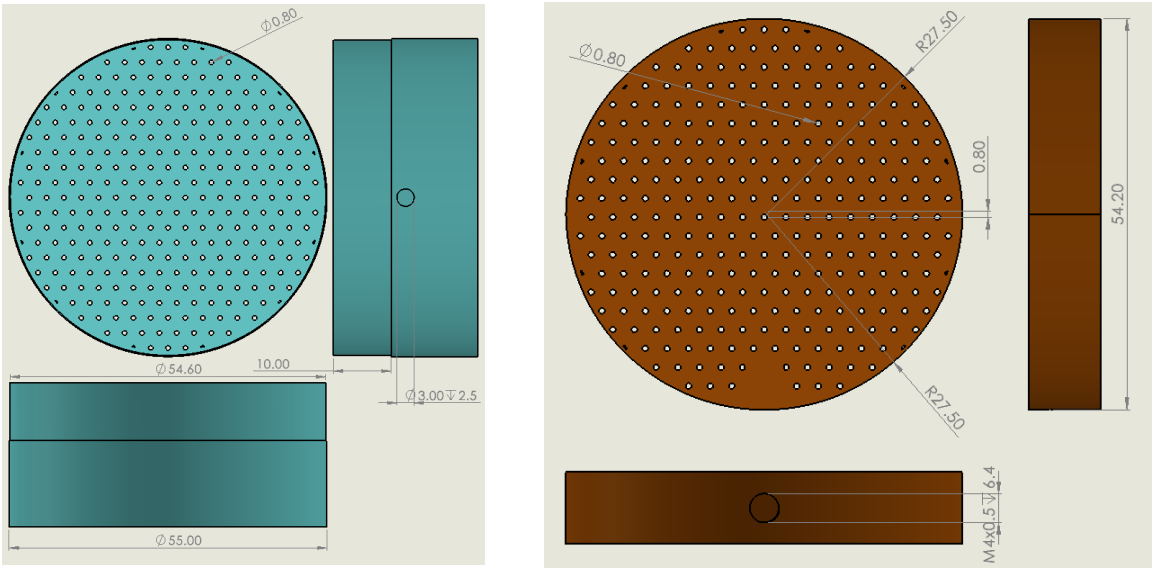

(a) (b)

Figure 3.13: 3-D printed Perforated disks for l_h = 3 mm hole spacing; (a) Top and Bottom disk; and (b): Middle disk (all dimensions are in mm)

3.4.4. Assembly of Dynamic configuration system

Figure 3.14 displays the isometric view of the exploded configuration of the actuation system with l_h = 1.5 mm disks installed (for representation). The middle disk was aligned in-plane with the actuator's push-rod. Dow Corning®high vacuum grease was used on the mating surfaces of each block and the outer edge of the mating surfaces was taped to seal air-gaps and impede air leakage. Key features of the assembly are as follows:

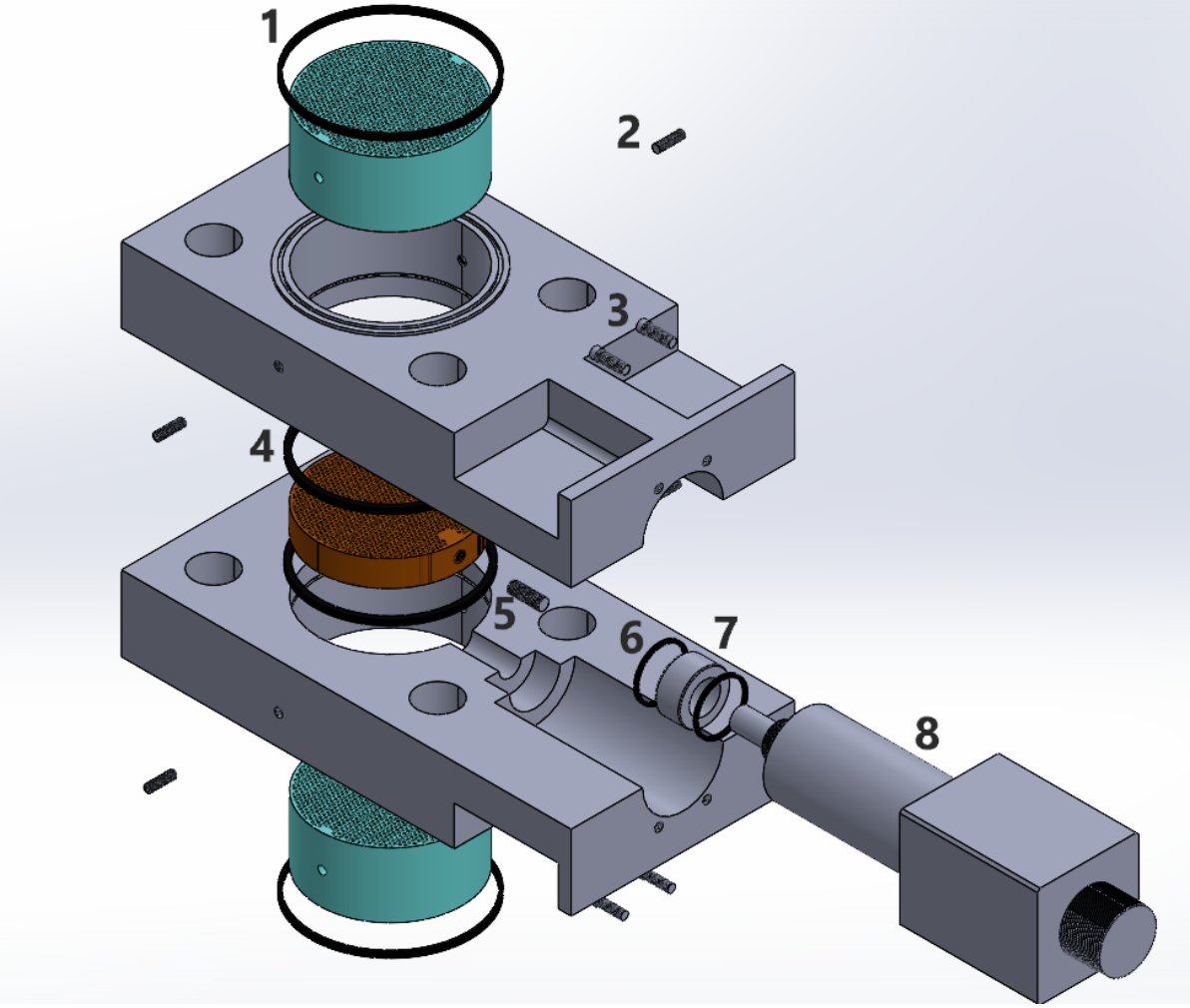

Figure 3.14: Complete assembly of the Dynamic Configuration set-up

1. *External O-rings*: Placed on the groove to seal the main source of air-flow leakage from the rig's pipe.

2. *Orientation screws*: Four M3 grub screws were tightened to hold the top and bottom disk in correct alignment and prevent their uncontrolled rotation or displacement in vertical direction.

3. *Actuator mount screws*: Four M3x0.25 screws were used to mount the rear body of actuator to the metal casing.

4. *Internal O-rings*: Two internal O-rings were installed to prevent air-leakage from the sample while the middle disk was actuated linearly.

5. *Threaded stud*: A 10 mm stud of $\phi = 4$ mm was used to connect the middle disk to the actuator push-rod.

6. *Actuator O-rings*: They were installed over a billet to seal the passage of air.

7. *Billet*: It was used provide location for O-ring grooves.

8. *Actuator body*: The body of stepper motor was tightly enclosed within the block casing and Dow Corning®high vacuum grease was applied to seal any air-gaps.

Figure 3.15 presents an actual image of the half-block actuator mount with the stepper motor connected to the middle disk via the threaded stud and the mating surface greased.

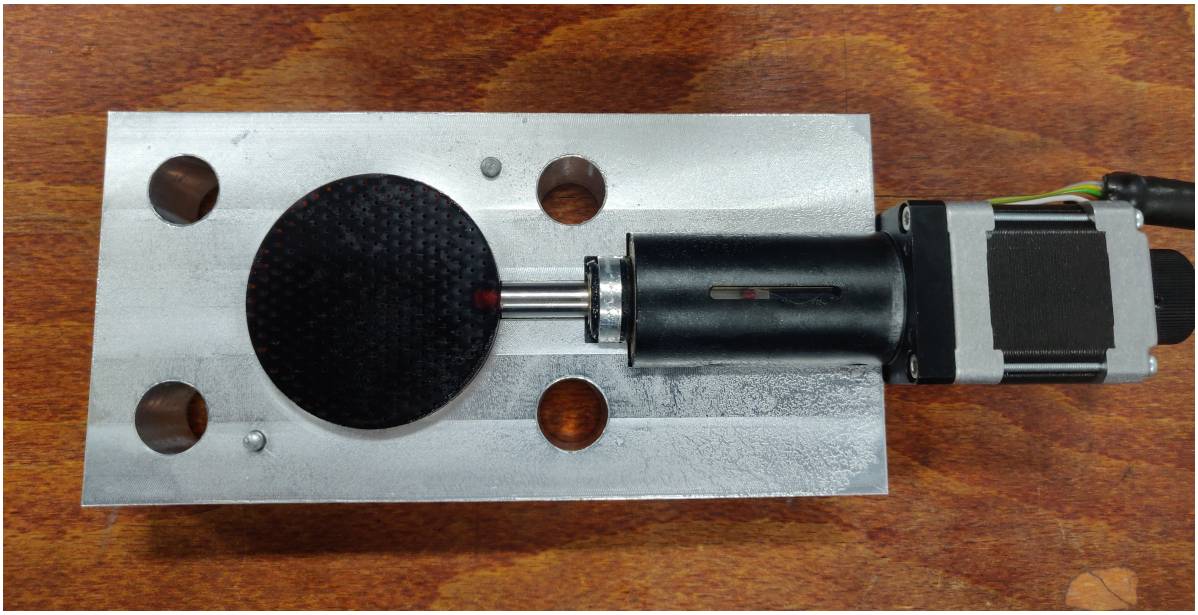

Figure 3.15: Real image of CNC milled actuator mount with perforated disk and Stepper Motor installed

3.5. Challenges of Dynamic configuration set-up over Static configuration set-up

The Dynamic configuration phase experiments were primarily designed to replicate the results obtained in the static configuration experiments. But due to inherent differences in the design of middle-disk shift mechanism for each case as well as notable changes in the pattern of perforated disks itself, the dynamic set-up faced multiple challenges which this study also aimed to address. The challenges were as follows:

- The perforated disks printed for dynamic set-up lacked tightening bolts. The tightening bolts were used to clasp the three disks together and prevent any movement or wobble of middle-disk during the static set-up experiments. This issue was partially solved by the use of four *orientation screws* that were installed on the sides of the disks. They held the top and bottom disks together and prevented any misalignment. Also, the positioning of *internal O-rings* helped mitigate possible air-leakage originating from the mating surfaces of the middle-disk due to them not being secured enough owing to the absence of tightening bolts.

- The unavailability of orientation pins in the dynamic set-up meant that determining the exact hole closure orientation or the position of middle disk was difficult while the setup was installed in the permeability rig. This issue was solved by creating a standard operating procedure (SOP) for the dynamic set-up:

1. Top and bottom disks were installed in their respective half-sliced actuator mount with help of *orientation screws*. The actuator mounts already had the *external* and *internal O-rings* placed in their respective grooves.
2. Stepper motor was connected to the middle-disk via a threaded stud in such a way that the tip of motor's push-rod touched the middle disk.
3. The actuator + middle disk assembly was placed in the bottom half-sliced actuator mount (also shown in Figure 3.15).
4. The stepper motor was signalled via the controller to push the middle-disk to the aft side of the inner cylinder. This position, by design, was the 0% closed hole orientation.
5. The mating surfaces of both mount blocks were greased and the top half-sliced actuator mount was placed over it and *Actuator mount screws* were tightened. In the end, it was taped from the edges.

In this way, the initial location or zero-point with reference to the stepper motor was always set. This strategy helped in maintaining precision in the location of middle-disk online while continuing permeability experiments.

- Since the mating surfaces of the two mount blocks were large, the possibility of air leaking out from their junction was higher as compared to static configuration where the external aluminum casing was one solid piece. To overcome the air-leakage, Dow Corning®high vacuum grease was applied in sufficient amounts on the mating surface and the outer edge of the junction of two blocks was taped end-to-end.

3.6. Summary of Experimental Set-up

This chapter presented, in detail, the apparatus this research work utilized for calculating flow permeability and other important parameters. It discussed, thoroughly, the need for static configuration experiments and the path to achieve variation in flow permeability through the novel Middle-Disk Shift mechanism. Subsequently, the approach for selecting an actuation system for the dynamic configuration was introduced and its incorporation with relevant modifications in the system were discussed. Therefore, keeping in mind all the challenges addressed for a dynamic configuration set-up to achieve an accurate and precise actuation system for variation in flow permeability, this report now proceeds to exhibit the raw and processed results ,thus, obtained from each configuration in the following chapter.

4

Results

This chapter presents the data collected from various tests done at the permeability rig of Low Speed Laboratory at TU Delft. Section 4.1 displays the pressure drop data at incremental flow velocities for various orientations of the middle disk. Section 4.3, 4.4 and 4.5 exhibit the calculated flow permeability, form factor and flow resistivity for each hole orientation, respectively. Appendix D presents the the mass flow rates at which the specimens were tested and their corresponding Reynolds number.

4.1. Pressure Drop tests

4.1.1. Variable hole depth to diameter ratio (δ / D)

Figure 4.1 presents the pressure drop across perforated disks of variable hole depth to diameter ratio. The pressure drops are plotted against pipe-level Reynolds number in fairly laminar flow regime. An error bar for each data point is incorporated that reflects the 2% measurement error in the TSI volumetric flow meter (as mentioned in section 3.1). Eq. 2.17 and eq. 2.26 predict that the pressure drop ΔP across a sample increases with increase in hole depth δ keeping other geometric parameters constant. Figure 4.1 closely follows the predictions for perforated disks of l_h = 3 mm and d_h = 0.8 mm. The increase in pressure drops can be associated to larger internal contact surface, at channel level, for thicker samples that leads to higher viscous drag or frictional resistance (eq. 2.22). These viscous drags are the source of pressure losses across the perforated sample.

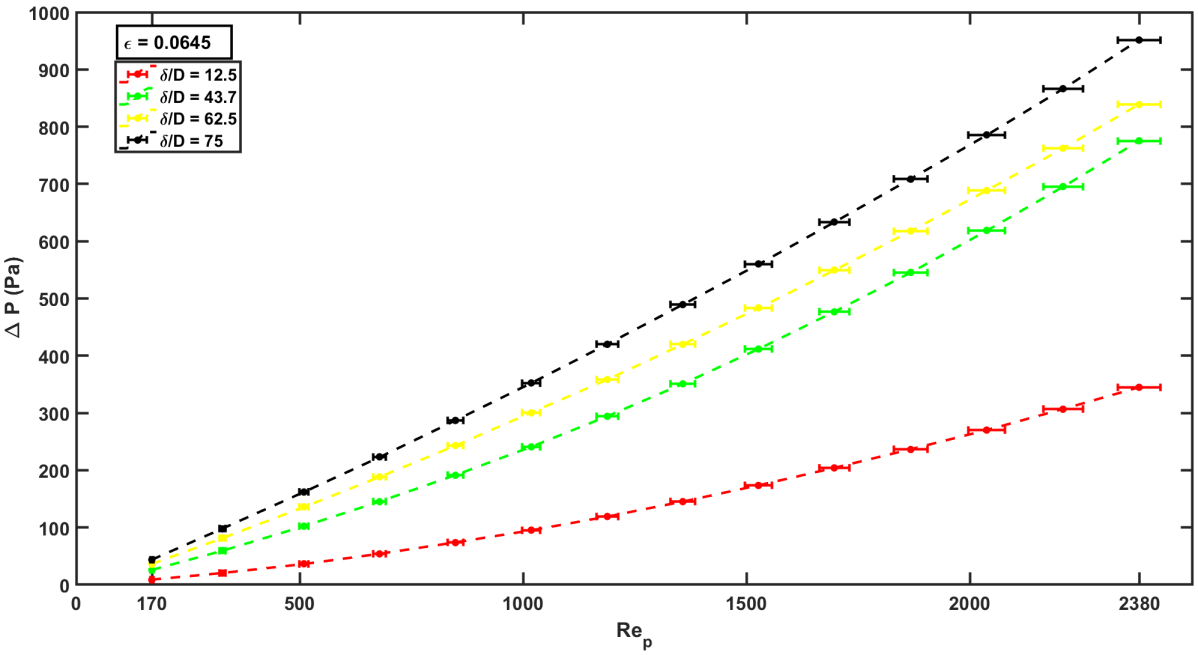

Figure 4.1: Pressure Drop v/s Pipe level Reynolds Number for variable δ/D

4.1.2. Static Configuration

The graphs for pressure drop or pressure losses across the 1.5 mm and 3 mm hole spacing were displayed in Figure 4.2 and Figure 4.3. The 100% closed hole orientation is for the system when holes are completely shut so effectively the the pressure drop observed across the sample at these orientations is air-leakage. The pressure drops for- 87.5% and 75% closed hole orientation in 1.5 mm sample and only- 87.5% closed hole orientation in 3 mm sample show drastic variations for increasing mass flow rate. The absolute magnitude of differential pressure is different for both perforated samples because the effective porosity varies.

The non-linear effect of the curve is also more prevalent if compared to rest of the less-closed orientations. The inertial effects that relate to the Form factor or so-called non-Darcy coefficient are more visible at higher Reynolds number of 87.5% and 75% closed hole orientation.

The pipe-level flow remains laminar throughout the test regime and reaches a maximum $\mathrm{Re}_p = 2380$ at $m^* = 0.017$ kg/s. At the hole level, maximum Reynolds number $\mathrm{Re}_h = 1212$ was achieved for $l_h = 3$ mm sample at 87.5% closed hole orientation. For $l_h = 1.5$ mm sample, maximum Reynolds number was $\mathrm{Re}_h = 301$, also at 87.5% closed hole orientation.

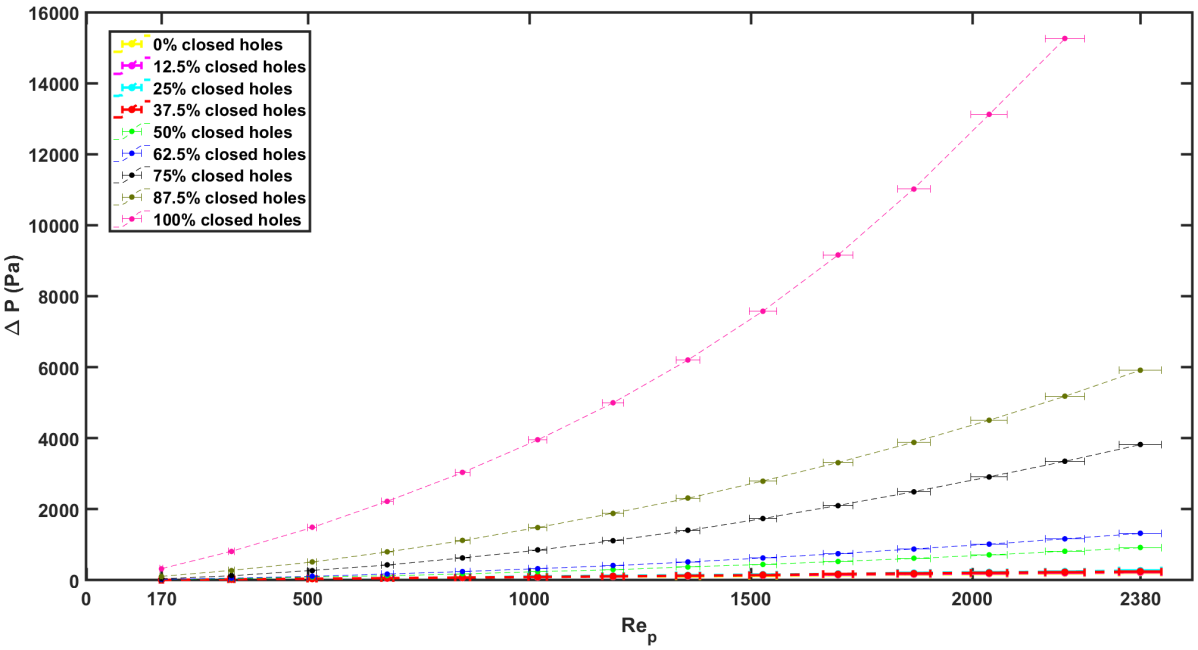

Figure 4.2: Pressure Drop v/s Pipe level Reynolds number for l_h = 1.5 mm in Static configuration

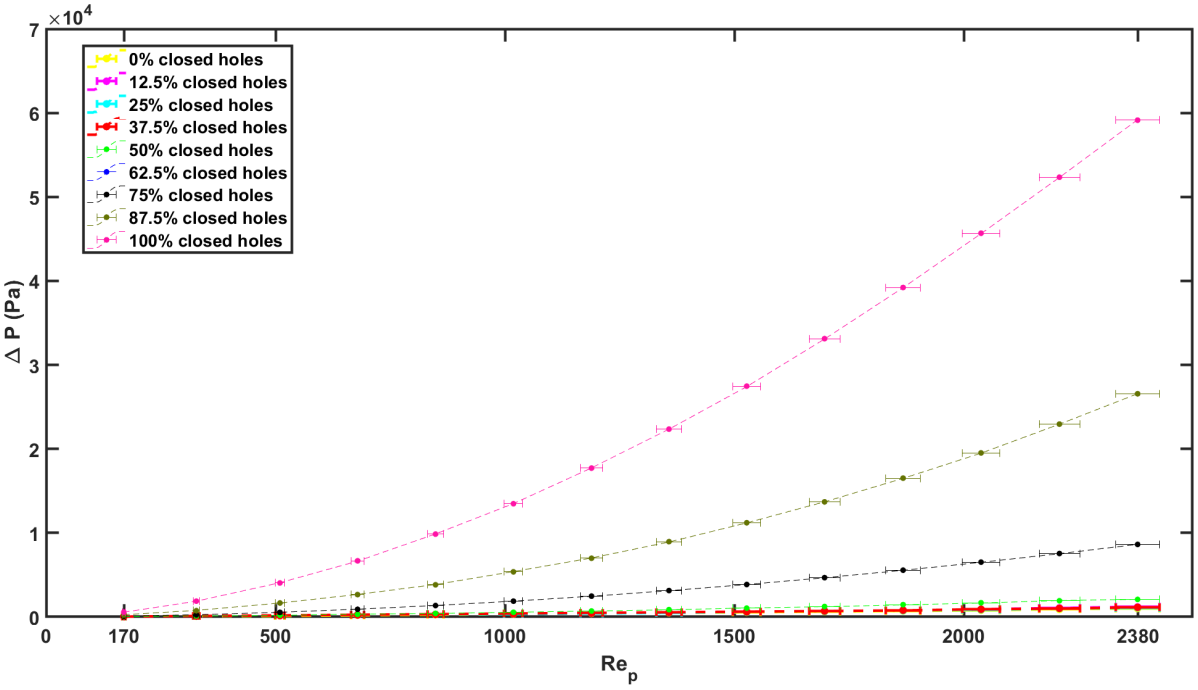

Figure 4.3: Pressure Drop v/s Pipe level Reynolds number for l_h = 3 mm in Static configuration

4.1.3. Dynamic Configuration

The trend-lines of dynamic configuration results in Figure 4.4 and Figure 4.5 followed that of static configuration as the differential pressure dropped substantially for 87.5% and 75% orientations while the gap between pressure drops of subsequent orientations mellowed down. The absolute magnitude of differential pressure for dynamic configuration was slightly lower as compared to that of static configuration because of possible air-leakage from the

mating surfaces of the three disks as they weren't bolted together like the static configuration. It is interesting to note that 100% closed hole orientation shows a curve which doesn't follow the ideal quadratic slope as given by eq. 2.26 for both the samples. The research safely ignores this trend-line because the air-leakage originating from possible air-gaps between mating surfaces at completely shut hole orientation doesn't ideally follow a set trend-line.
The non-linearity of each curve is prevalent at higher mass flow rates (or Reynolds number) but is more visible for more closed configurations due to higher magnitudes of absolute pressure drops.

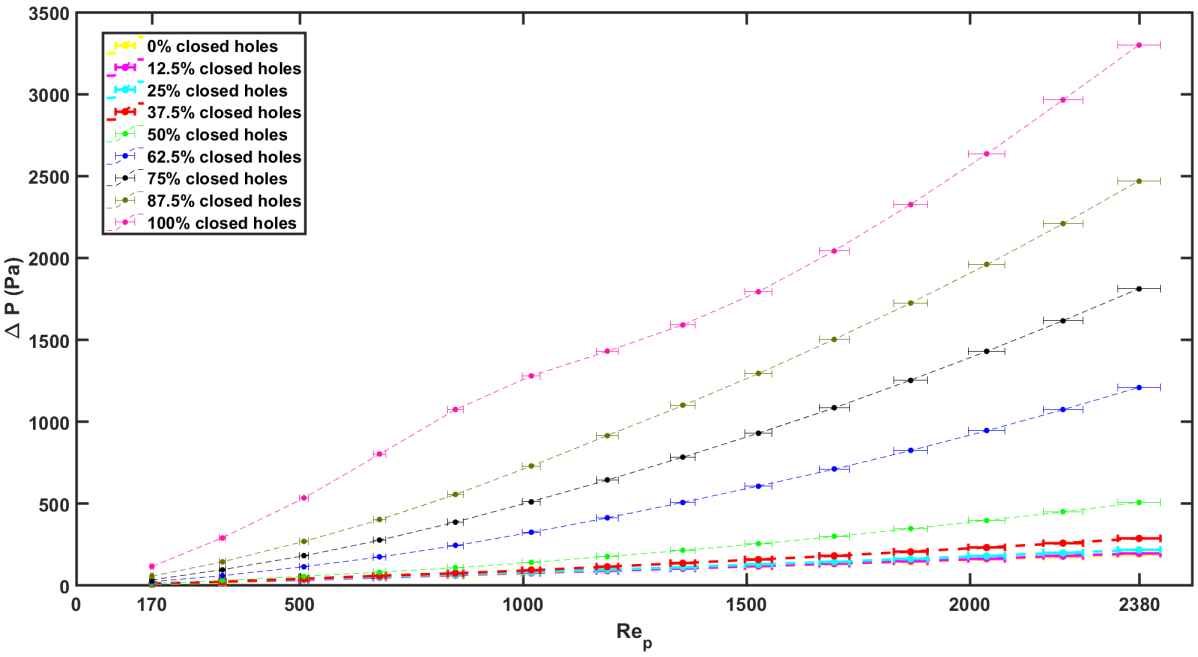

Figure 4.4: Pressure Drop v/s Pipe level Reynolds number for l_h = 1.5 mm in Dynamic configuration

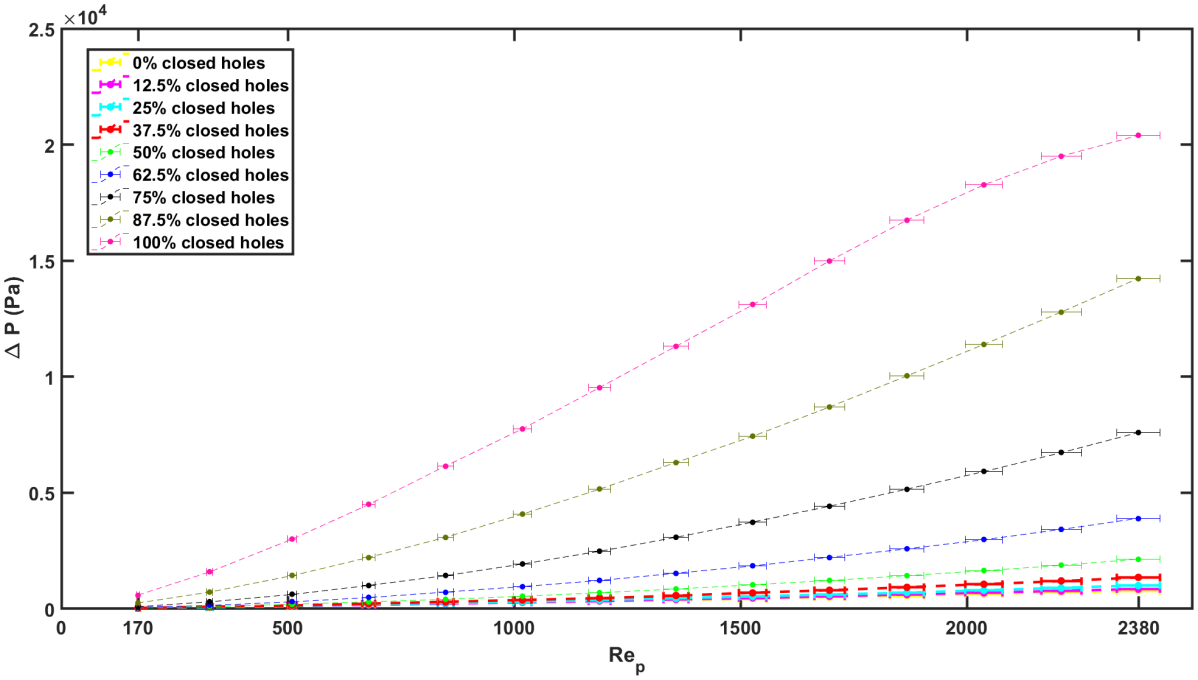

Figure 4.5: Pressure Drop v/s Pipe level Reynolds number for l_h = 3 mm in Dynamic configuration

4.2. Flow Permeability

4.2.1. Static Configuration

The flow permeability (K) was calculated using a non-linear least square fitting function for the pressure drops and the mass flow rates. Subsequently. the values were computed through Hazen-Dupuit-Darcy expression (eq. 2.25) . The average Rsq value for each orientation was >0.9980. From Figure 4.6 and Figure 4.7 we can see that permeability varies extensively from 87.5% closed hole orientation to 50% closed hole orientation and stabilizes subsequently. This trend can be understood from the fact that the non-linearity was very small for <37.5% closed hole orientation which correlates to the inertial forces being less dominant at more open orifice holes. Also, the pressure drop curves virtually converged as the hole effectively opened more than half. Effectively, the low difference in pressure losses at < 37.5% closed hole orientation was reflected by a virtually-uniform permeability curve after half open position of middle disk.

The permeability (K) for 100% closed hole orientation should ideally have been 0 since the three disks should have behaved like one solid impermeable cylinder but we observed small permeabilities due to air-leakage of the order of K = 2.66x10^{-10} and K = 7.48x10^{-11} for 1.5 mm and 3 mm hole spacing sample, respectively.

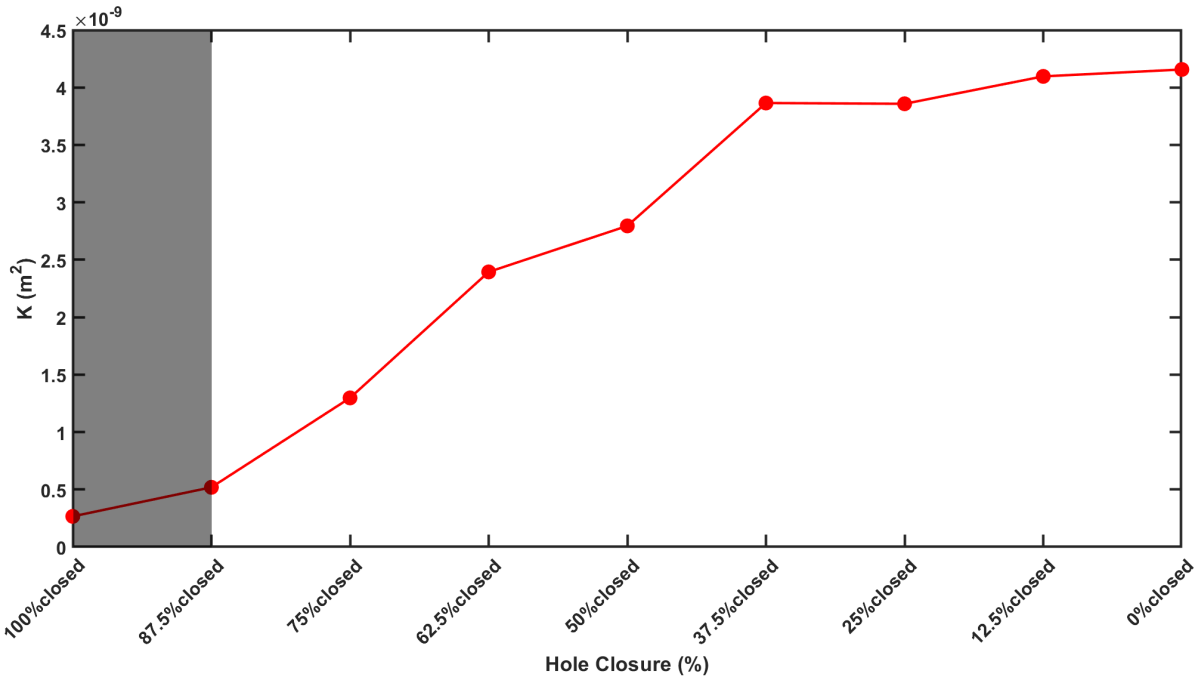

Figure 4.6: Flow Permeability v/s Hole Closure for l_h = 1.5 mm in Static configuration

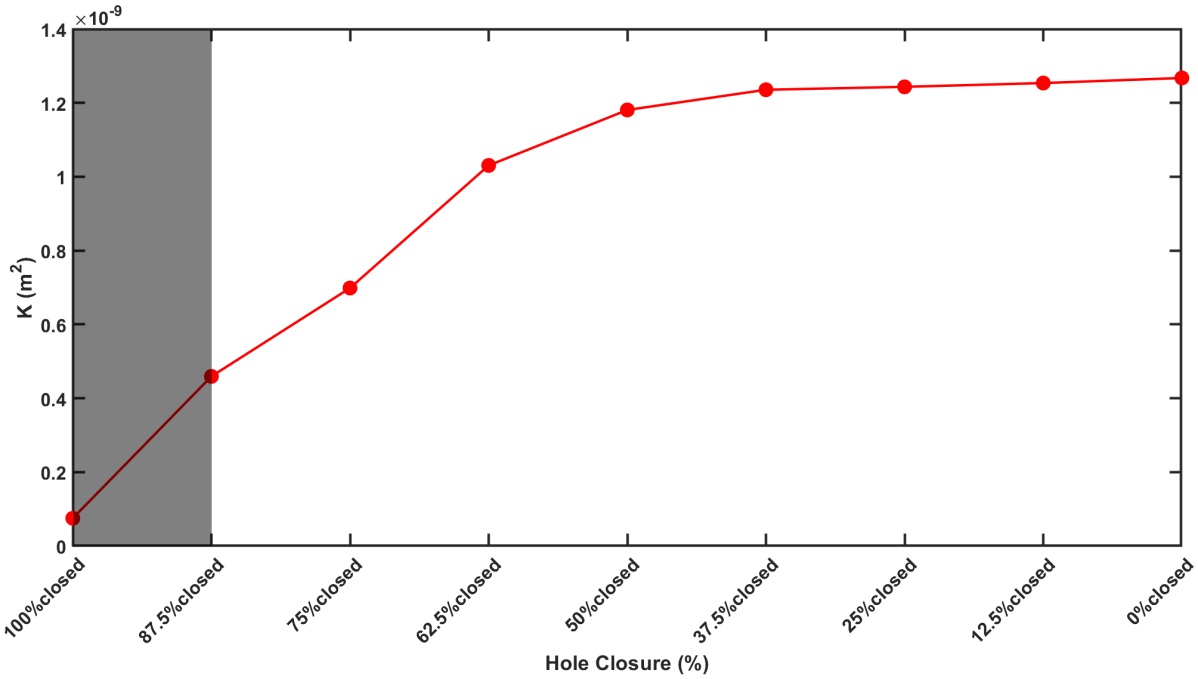

Figure 4.7: Flow Permeability v/s Hole Closure for l_h = 3 mm in Static configuration

4.2.2. Dynamic Configuration

During the dynamic configuration tests, multiple cycles were performed for l_h = 3 mm sample and permeability was calculated from close to open holes orientation and open to close holes orientation (Figure 4.9). Close to Open cycle meant the actuation rod of the stepper motor "pushed" the middle disk 0.8 mm and Open to Close cycle meant the actuation rod

"pulled" the middle disk 0.8 mm back. The 1^{st} iteration was conducted from close to open holes orientation after which set-up was dismounted from the permeability test rig. After every cycle, the set-up was dismounted and re-installed, so error is more visible between different cycles. For l_h = 1.5 mm sample, only one iteration from Close to Open hole orientation is presented in Figure 4.8 because the threaded socket inserted in the middle disk of l_h = 1.5 mm sample faced a pull-out by the stepper motor while proceeding with Open to Close hole orientation. This effectively meant that the middle disk didn't get actuated and only the threaded socket was pulled-out by the stepper motor. It was a manufacturing defect as the threaded scoket wasn't glued properly to the insides of the middle disk.
In line with the results from the static configuration, the permeability increases substantially from 87.5% closed - 37.5% closed orientation and then stabilizes for both the samples. For l_h= 3 mm sample it was also observed that permeability of each hole orientation increased slightly for the open to close cycles. The possible reason could be mis-alignment of perforated holes on the way back due to minor deviation in the transverse axis of motion. This deviation was caused by two reasons:

- By the improper alignment of the threaded stud in the middle disk. Ideally it should be in line and in plane with the axis of actuation rod of the stepper motor whereas during the tests it was observed that the threaded stud was at an angle $<1^o$ from the axis of actuation rod.

- Middle disk also shifted transversely due to it being designed with an eccentricity of 0.8 mm. As discussed in chapter 3, the geometry of middle disk when assembled inside a circular cylinder of diameter 55 mm left gaps between the disk and inner wall of cylinder in shape of arcs on both sides of the disk. These geometric gaps allowed certain rotation of the middle disk while it travelled laterally. The mis-alignment arising from this geometric feature could have given rise to an increase of air-leakage in Open to Close cycle.

An error of 2μm is introduced which refers to the positioning error of the stepper motor as mentioned in Appendix C.

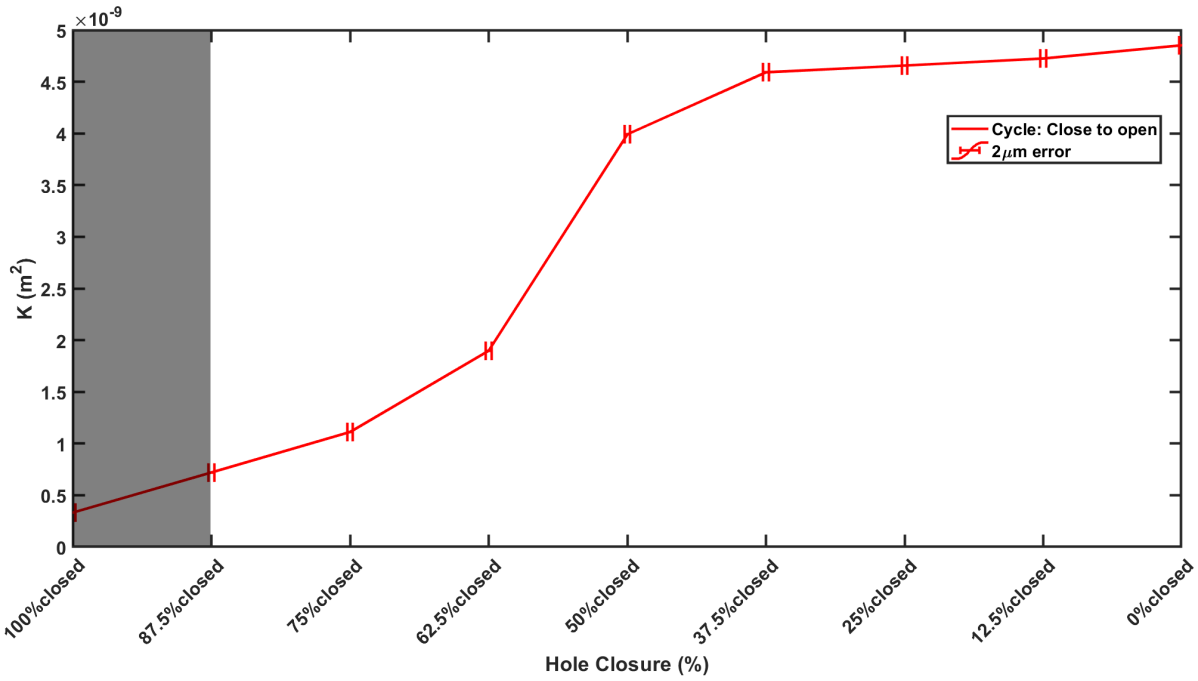

Figure 4.8: Flow Permeability v/s Hole Closure for l_h = 1.5 mm in Dynamic configuration

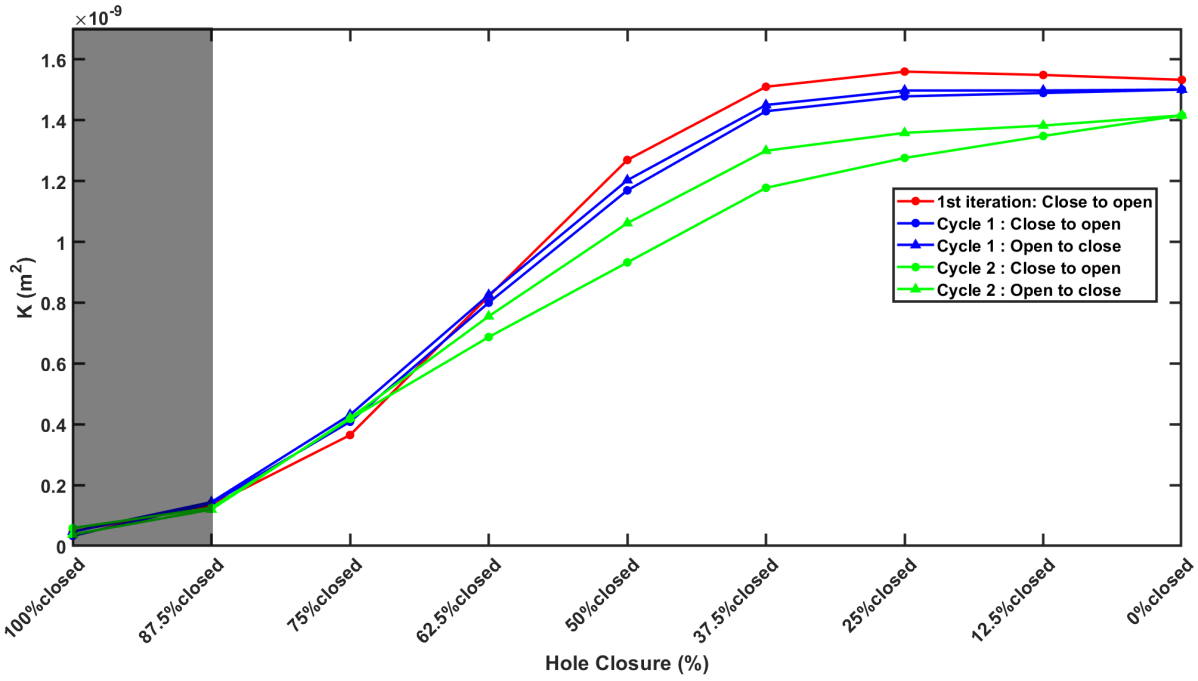

Figure 4.9: Flow Permeability v/s Hole Closure for l_h = 3 mm in Dynamic configuration

4.3. Form factor

4.3.1. Static Configuration

The Form factor or the Forchheimer coefficient is related the non-linear effects of the flow at non-Darcy regime. The inertial effects of the fluid particles were accounted for at variable Reynolds number. It is was also calculated by non-linear least-square fitting of the

pressure drops while also taking into account the temperature dependant density of air.
For both the samples (Figure 4.10 and Figure 4.11), the form factor increased substantially post-37.5% hole closure. This was also reflected in the increase in slope of differential pressure values post-37.5% closure. The non-linearity of the pressure drop curves was observed to increase significantly as the effective closure of perforated holes happened. The Forchheimer coefficient is responsible for the non-linear effects and the non-linear drag in the flow regime.
The inertial effects can also be visualized by considering a fluid particle that tends to travel in a straight line if external parameters aren't acted on it. If the flow path is changed, in other words, Tortousity Γ is induced in the flow path, in our case, by introducing a middle disk shift, then the flow particle will be acted on by a normal force. This normal force will effectively deviate the flow and induce inertia dependant drag on the channel. As seen from the curve, at 100% closed hole orientation, the Form factor should ideally be infinite due to availability of no flow path but in this case due to air-leakage, a finite but substantive value of C was observed at shut hole orientation. The curves of both samples also reflect on the fact that flow path virtually remains unchanged for 0% - 37.5% closed holes orientation. So the shift of middle disk doesn't affect the flow pattern effectively for the first four steps. This was also visible in the Permeability curves of Section 4.2.

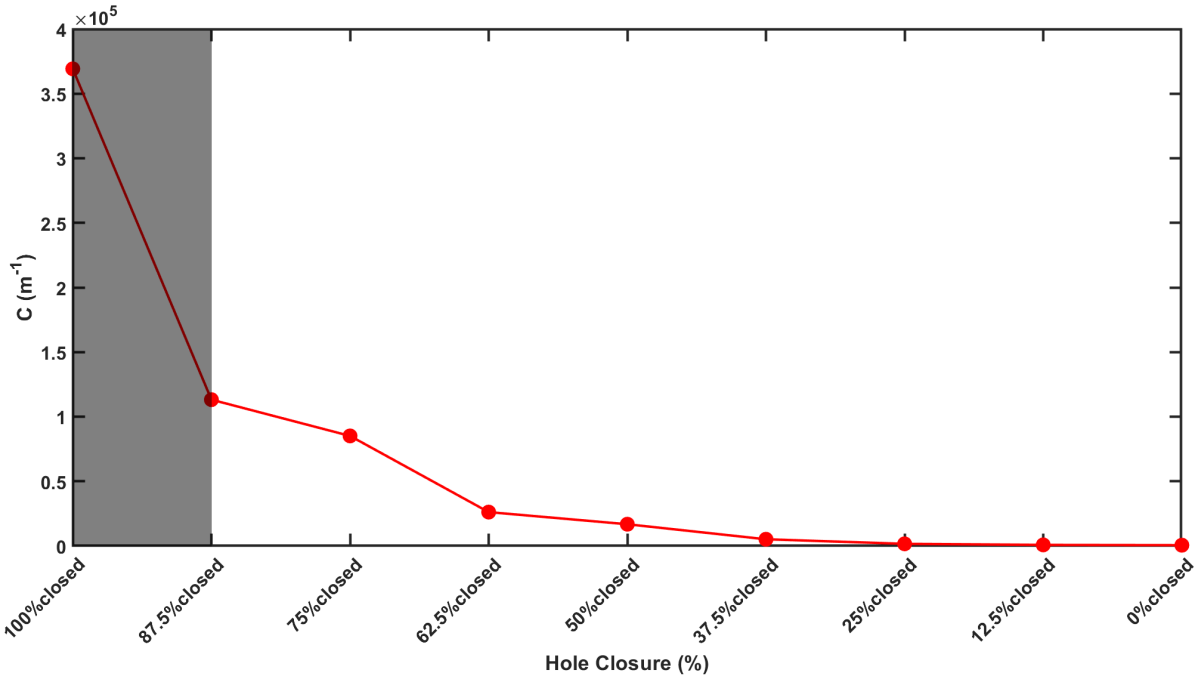

Figure 4.10: Form Factor v/s Hole Closure for l_h = 1.5 mm in Static configuration

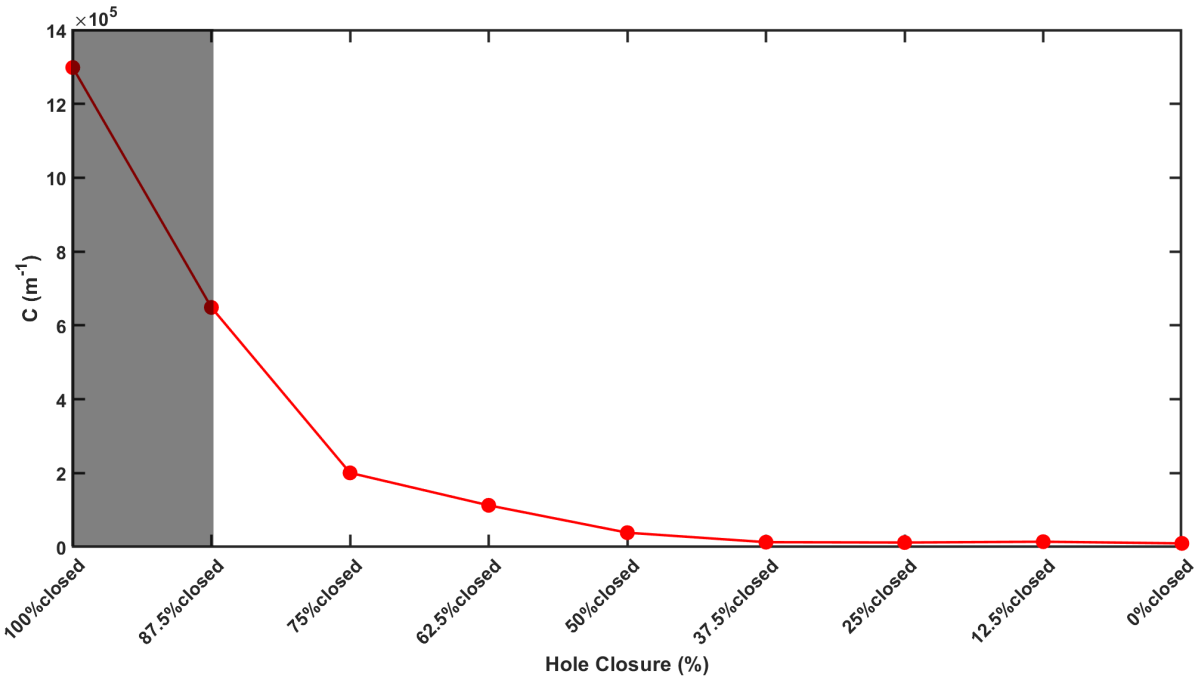

Figure 4.11: Form Factor v/s Hole Closure for l_h = 3 mm in Static configuration

4.3.2. Dynamic Configuration

The trend line for form factor of the dynamic set-up in Figure 4.12 and Figure 4.13 effectively follows that of static set-up from 0% closed hole configuration to 87.5% closed hole orientation although the absolute magnitude of non-Darcy coefficient C is not the same. The difference between absolute magnitude of form factor for tests conducted in static configuration setup and dynamic configuration set-up grows as hole closure is increased. The C_{static} is higher than $C_{dynamic}$ in all cases but two. The reason for it could potentially be the middle-disk not holding onto its position firmly at higher hole level Reynolds number Re_h (for 50% - 87.5% closed hole orientation) in dynamic setup when compared to static setup due to absence of orientation holes and tightening bolts. Since form factor is a measure of inertial effects of flow, which is also dependant on straightness of the path of fluid flow or tortuosity Γ, it can be concluded that potential disturbances in the position of middle disk at higher Re_h lead to normal forces induced by middle-disk(in transverse direction) acting on a fluid particle travelling in a straight path through the hole to be less in magnitude. The reduction in normal forces lead to a diminished form-factor for dynamic configuration.

Also, perforated disks for static and dynamic set-ups had a few changes in design to incorporate orientation holes (in static setup) and push-rod connector hole (in dynamic set-up) (Section 3.3.1 and 3.4.3) which contributed to difference in form factor overall in both the setups. At the 100% closed hole orientation the curves split in multiple directions for both l_h = 1.5 mm and l_h = 3 mm sample. The form factor relating to this orientation is ideally infinite but due to air-leakage the curvature at this orientation cannot be predicted. Therefore, in this paper this region has been safely ignored. As evident from Figure 4.13, the form factor values for all five iterations closely follow each other but are more precise for a given cycle in both directions. The error between cycles is related to human factor since the set-up is opened and installed again in the test rig for each cycle.

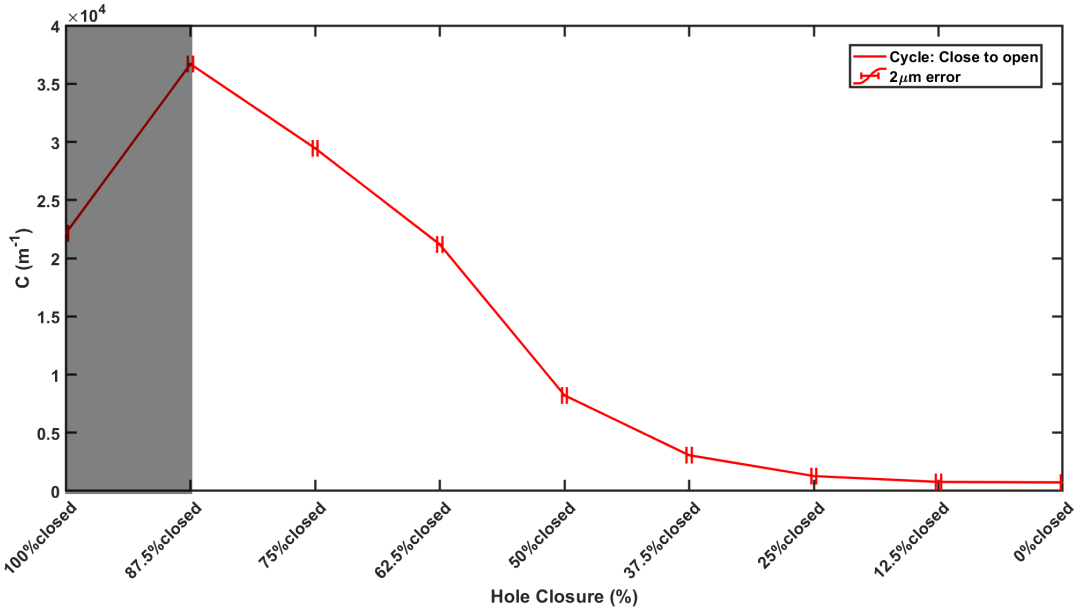

Figure 4.12: Form Factor v/s Hole Closure for l_h = 1.5 mm in Dynamic configuration

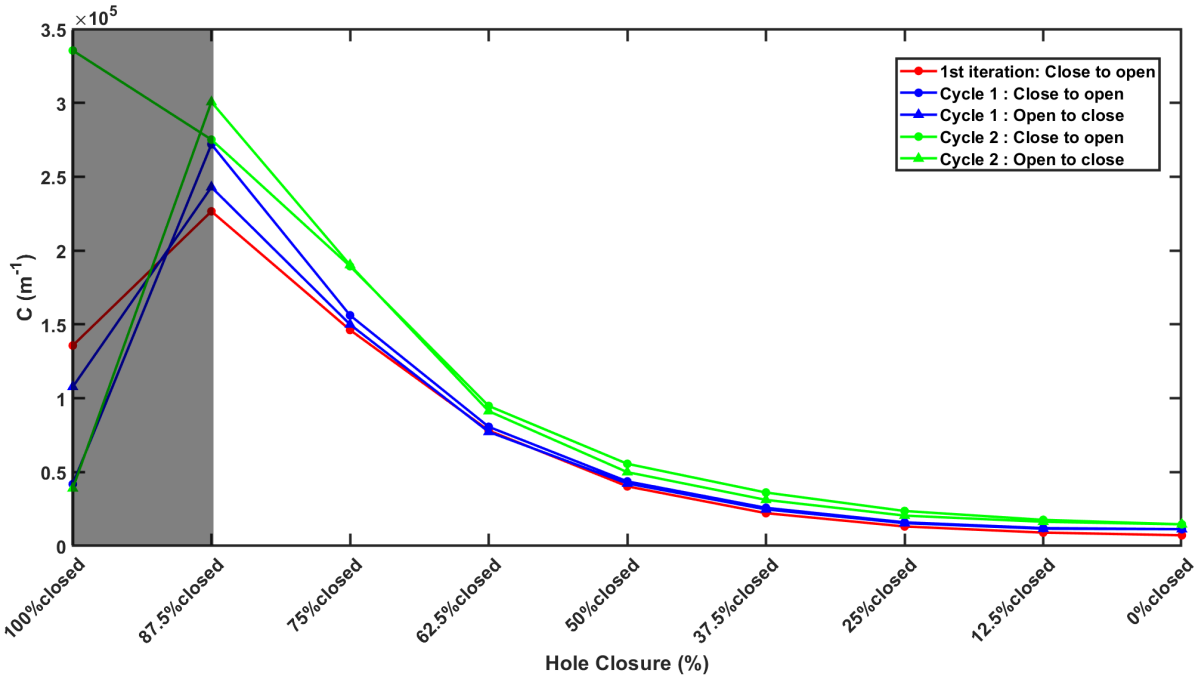

Figure 4.13: Form Factor v/s Hole Closure for l_h = 3 mm in Dynamic configuration

4.4. Flow Resistivity

4.4.1. Static Configuration

The Flow resistivity (R) was defined as the ratio of temperature dependant dynamic viscosity μ and the flow permeability K. It is the resistance offered by the porous medium to the flow of fluid particle. The curves for both l_h = 1.5 mm and l_h = 3 mm in Figure 4.14 and

Figure 4.15, respectively, can be explained by the reasoning that the hydraulic diameter of the flow channel doesn't effectively reduce uniformly from 0% closed hole orientation to 37.5% closed hole orientation even though the disk shifts 0.1 mm in each step. The closure of hole only takes actual effect post 37.5% closed hole orientation when hydraulic diameter starts decreasing rapidly, thus resulting in an increase in the Flow Resistivity of the porous medium. For 100% closed hole orientation the resistivity should have been ideally infinite since the Flow Permeability is expected to be zero but as explained in Section 4.3, air leakage from the middle disk surfaces or the mating surfaces lead a non-infinite magnitude of Flow Resistivity. The Flow Resistivity for l_h = 3 mm perforated disks is larger due to lesser porosity in the sample.

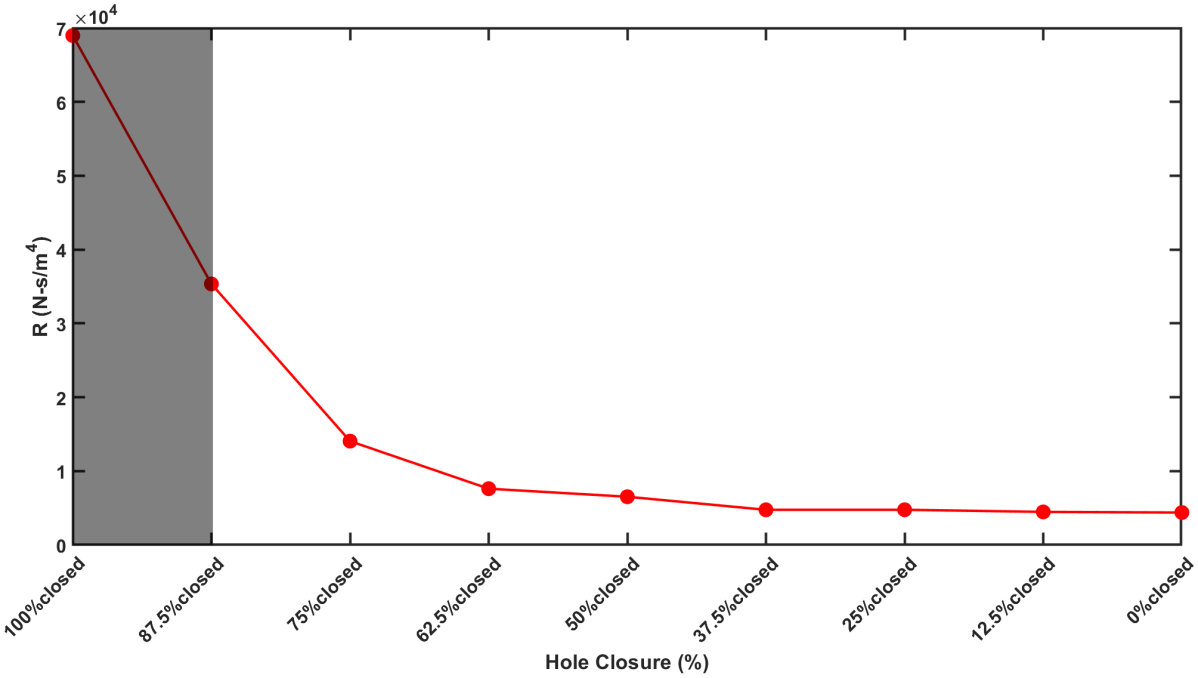

Figure 4.14: Flow Resistivity v/s Hole Closure for l_h = 1.5 mm in Static configuration

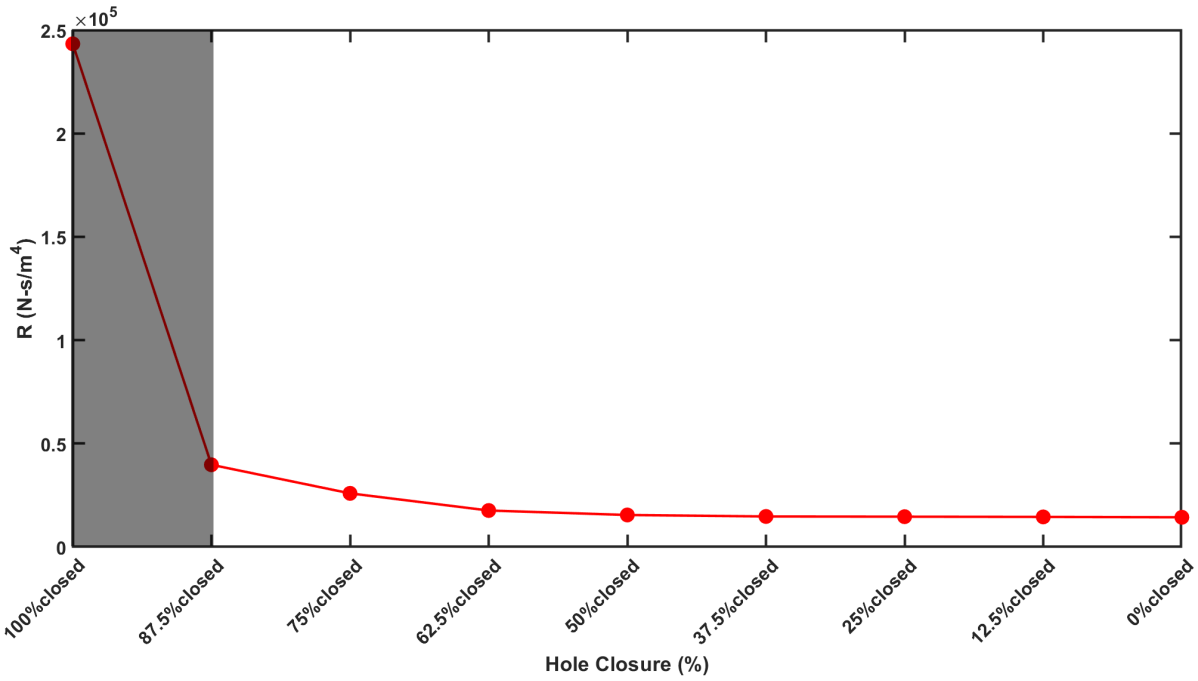

Figure 4.15: Flow Resistivity v/s Hole Closure for l_h = 3 mm in Static configuration

4.4.2. Dynamic Configuration

The results of dynamic configuration setup followed the same trend-line as that of static configuration setup. The Flow Resistivity starts jumped post-50% closed hole orientation pointing towards a model where the effective hydraulic diameter D_{eff} starts varying drastically post 37.5% closed hole orientation. The absolute values of Flow Resistivity in dynamic configuration relate closely to their static counter-parts. Figure 4.17 depicts that R for each cycle of l_h = 3 mm sample virtually coincides up-til 87.5% orientation. Post that air-leakages reduced the absolute Resistivity magnitude to a finite value that varies for each cycle because flow mechanics of leaked air in shut hole configuration doesn't lie within the bounds of parameters fixed within this research.

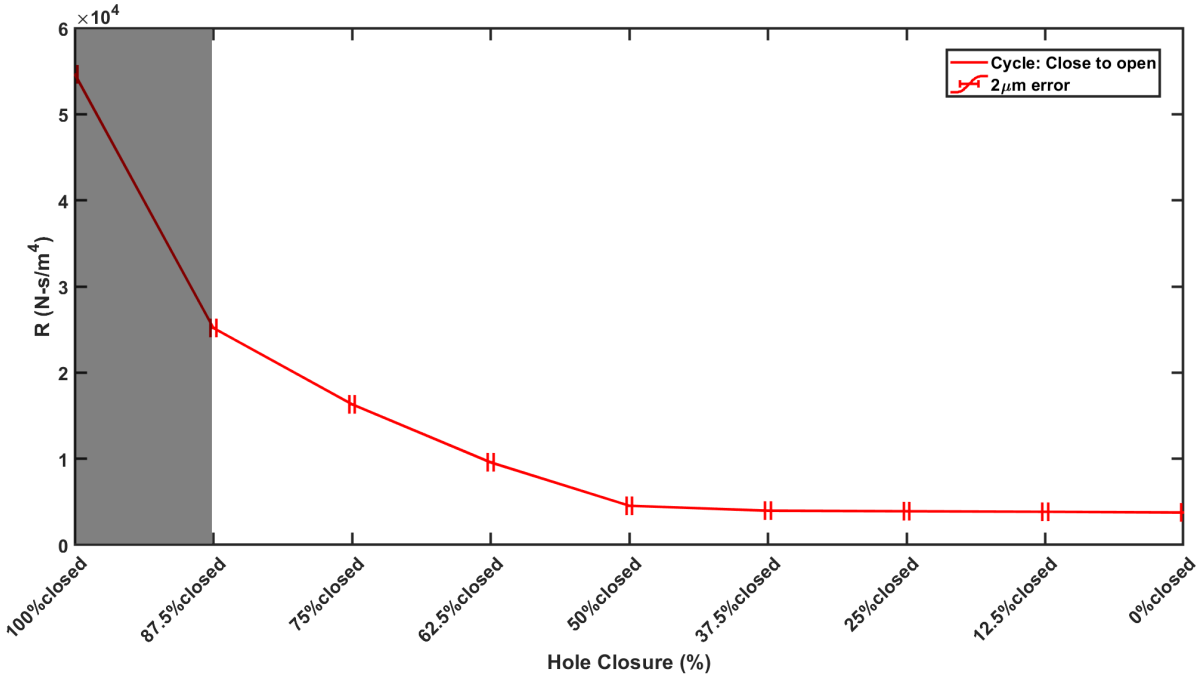

Figure 4.16: Flow Resistivity v/s Hole Closure for l_h = 1.5 mm in Dynamic configuration

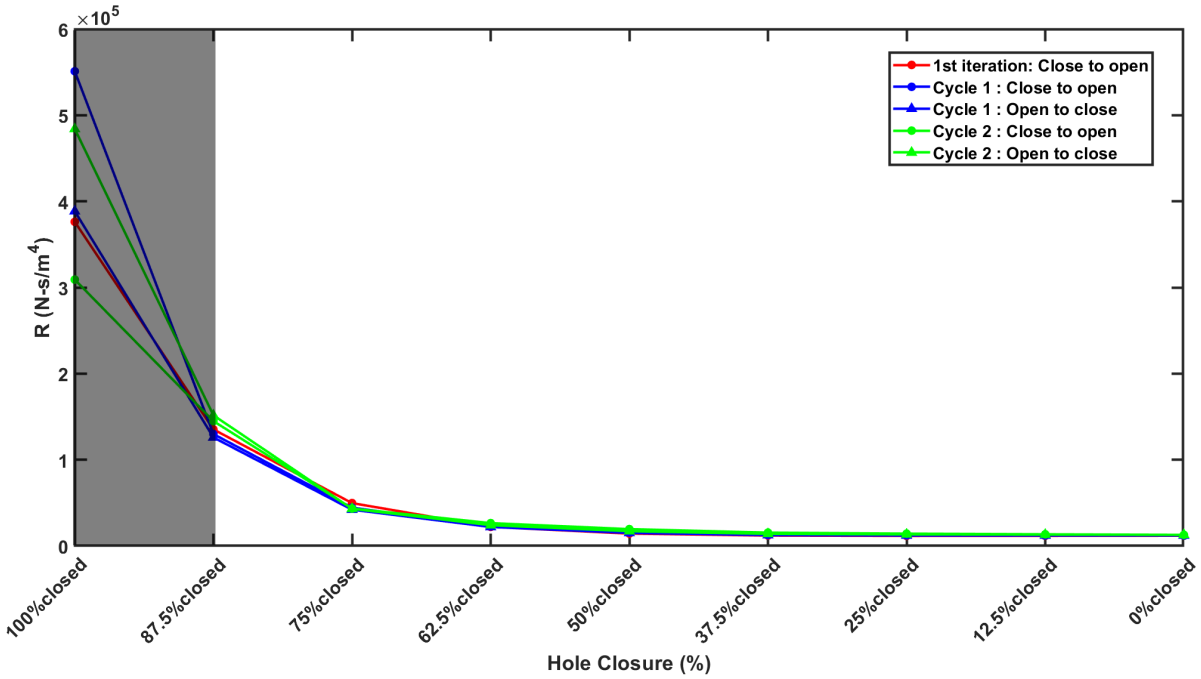

Figure 4.17: Flow Resistivity v/s Hole Closure for l_h = 3 mm in Dynamic configuration

5

Discussions

This chapter develops arguments for the observations recorded in the previous chapter. It takes cognizance of the pressure drop trends and the flow parameter variations observed during the test phase of this project and extracts crucial information regarding the working and efficacy of Middle-Disk Shift mechanism. The following section lists the parameters dependant on hole closure which is followed by a discussion on the Darcy-Forccheimer drag and its relation to some geometric parameters. This chapter also weighs into the degree of repeatability of the novel actuation device by presenting comparison curves for static and dynamic configurations. Lastly, a new parameter is introduced to assess the variation of flow permeability and effective porosity with incremental displacement of middle disk.

5.1. Effect of Hole Closure on other parameters

5.1.1. Hydraulic diameter

Bird's eye view diameter (D_{BEV})

The bird's eye view diameter is the characteristic length of the fluid flow as seen from the top view of the model. Its given by the formula: $D_{BEV} = \frac{4 * A}{P}$ where A is the cross-section of pipe and P is the wetted perimeter. Since the closure in the middle disk lead to a non-circular cross-section of the channels, a D_{BEV} for each configuration was determined. Figure 5.1(a) visualizes the bird's eye view diameter for a middle disk shift mechanism.

Effective Hydraulic diameter (D_{eff})

The effective hydraulic diameter was distinguished from the Bird's eye view diameter as the effective pore space which varied after shifting the perforated plates in the middle. Figure 5.1(b) displays how the fluid flows in a partially closed hole achieved by middle-disk shift principle. The calculation of a effective hydraulic diameter was done by using Darcy-Weisbach equation for pressure losses (eq. 22 & eq. 2.23). For ease of calculation, a single perforated channel was considered with pressure drop across it due to viscous forces. The effective hydraulic diameter was then back-calculated (presented in Table 5.1) for different values of mass flow rates m^* and pressure drop ΔP variations. Table 5.1 lists the non-linear variations in effective hydraulic diameter with respect to linear increments in Bird's eye view diameter and middle-disk position.

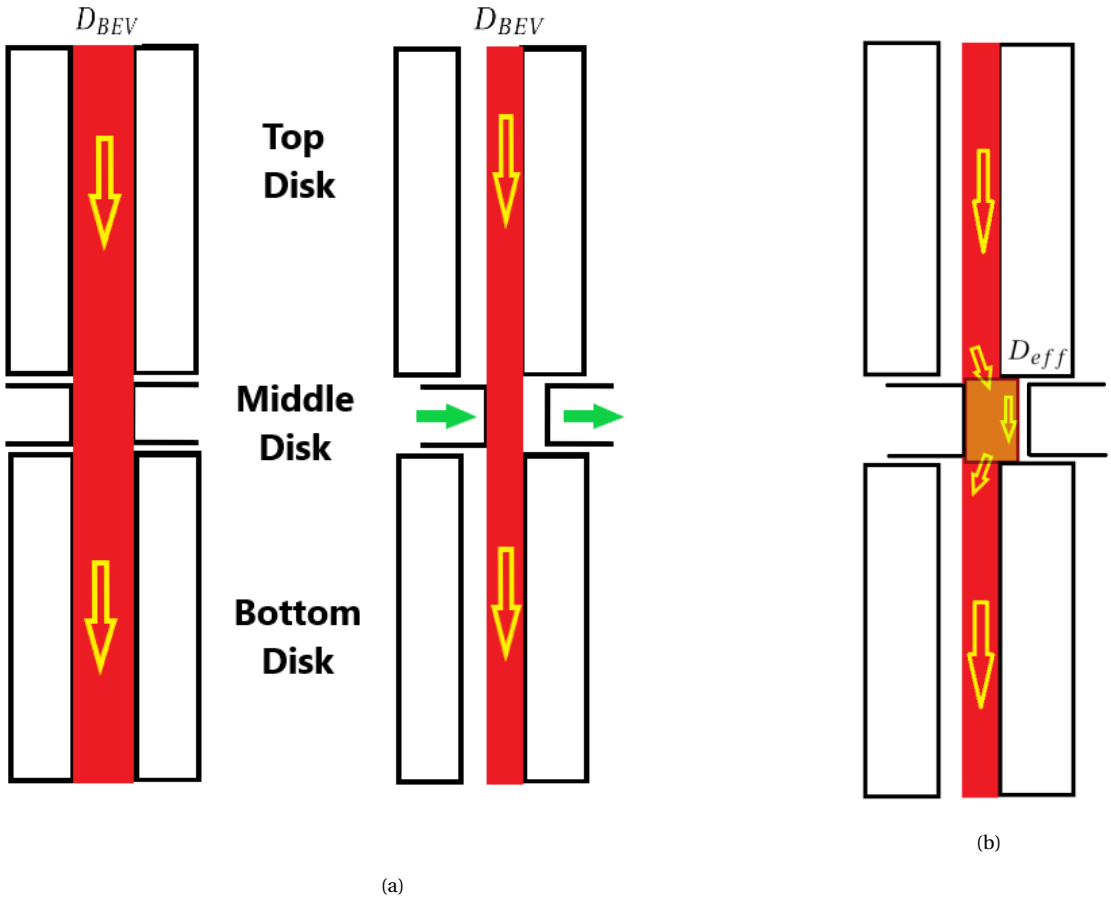

Figure 5.1: Schematics of air-flow through a single pore with Middle-Disk Shift mechanism (a) Bird's Eye View diameter; and (b) Effective Hydraulic diameter

5.1.2. Porosity

The porosity ϵ of a material is the measure of void spaces in it. It is the ratio of open area to the total area of the segment and ranges between 0 and 1. The porosity for a 60^o offset staggered arrangement is discussed and presented in eq. 3.1 of section 3.2.

Two porosities were calculated for the middle-disk shift mechanism model pertaining to D_{BEV} and D_{eff}: $\epsilon_{BEV} = \frac{\pi D_{BEV}^2}{2\sqrt{3}l_h^2}$; $\epsilon_{eff} = \frac{\pi D_{eff}^2}{2\sqrt{3}l_h^2}$ Fig. 5.2 shows the non-linear increment in Effective Porosity ϵ_{eff} with respect to linear changes in Bird's eye view Porosity ϵ_{BEV} for l_h = 1.5 mm sample. The data for ϵ_{eff} for l_h = 3 mm sample follows similar trend-line but is not included in the report.

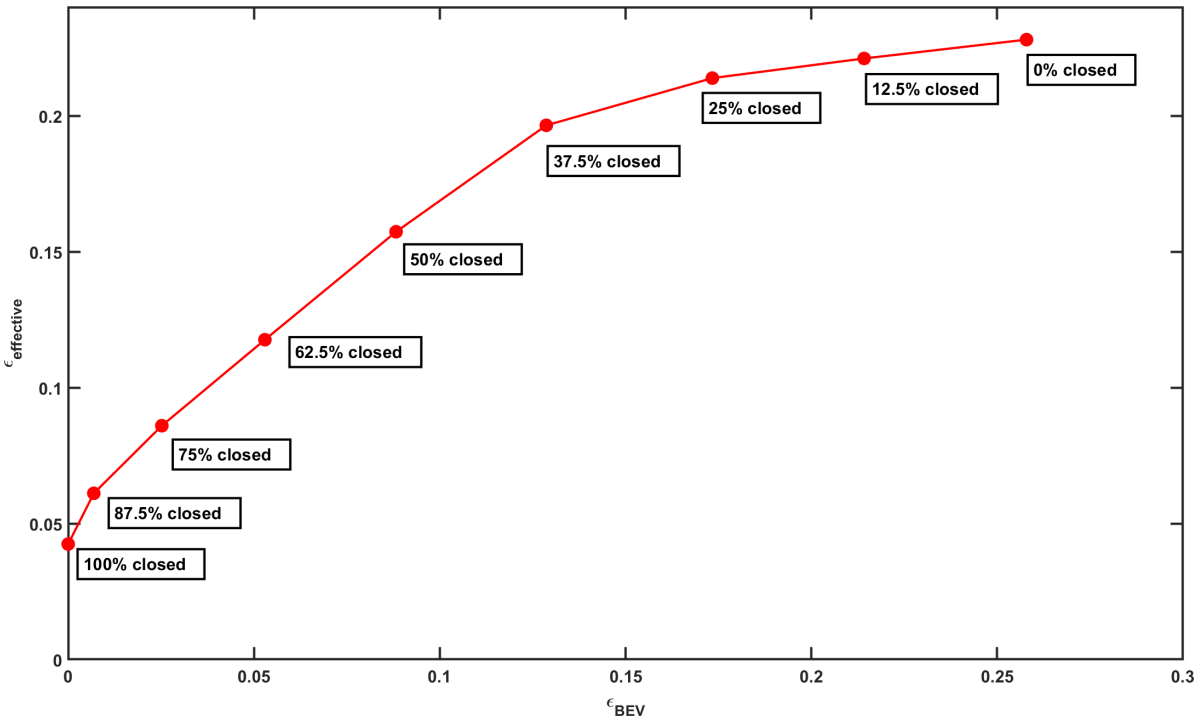

Figure 5.2: Relation between linear increments in Bird's eye view porosity and Effective porosity for l_h = 1.5 mm

5.1.3. Tortuosity

Tortuosity τ is a geometrical property of the travel path. It is unit-less and commonly used to describe diffusion and fluid flow in porous media. In this research, the calculation for tortuosity was done assuming a 2-D fluid flow channel with all air particles taking the longest route possible to flow across the disk. Fig. 5.3 displays the route assumed for fluid particle flow during calculations. The formula for tortuosity is given as: $\tau = \frac{L}{L_o}$ where L is the actual distance travelled by a fluid particle and L_0 is the shortest possible distance between the two points.

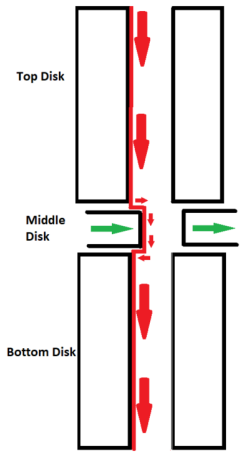

Figure 5.3: Geometric Toruostiy of the Middle-Disk Shift mechanism

Table 5.1: The relationship of Hole orientation with other parameters

Hole Orientation (%)	**Hydraulic Diameter**		**Porosity**				**Tortuosity (τ)**
	Bird's eye view Diameter (D_{BEV})	**Effective Hydraulic Diameter (D_{Eff})**	$\epsilon_{1.5mm}$		ϵ_{3mm}		
			ϵ_{BEV}	ϵ_{Eff}	ϵ_{BEV}	ϵ_{Eff}	
100 % closed	0	0.325	0	0.042	0	0.010	-
87.5 % closed	0.130	0.389	0.006	0.061	0.001	0.015	1.023
75 % closed	0.250	0.462	0.025	0.086	0.006	0.021	1.02
62.5% closed	0.362	0.540	0.052	0.117	0.013	0.029	1.016
50 % closed	0.467	0.625	0.088	0.157	0.022	0.039	1.013
37.5 % closed	0.565	0.698	0.128	0.196	0.032	0.049	1.01
25 % closed	0.655	0.728	0.173	0.213	0.043	0.053	1.006
12.5 % closed	0.729	0.741	0.214	0.221	0.053	0.055	1.003
0 % closed	0.800	0.752	0.257	0.228	0.064	0.057	1

The net effective change in porosity $\Delta\epsilon_{Eff}$ for each sample is given as:

$$\Delta\epsilon_{Eff} = \frac{\epsilon_{Eff-0\%} - \epsilon_{Eff-100\%}}{\epsilon_{BEV-0\%} - \epsilon_{BEV-100\%}} x100 \tag{5.1}$$

For l_h = 1.5 mm, $\Delta\epsilon_{Eff}$ = 72.37%; & for l_h = 3mm, $\Delta\epsilon_{Eff}$ = 73.43%. Ideally, from a 0% closed hole orientation to completely shut hole orientation, the net porosity change of the perforated disks should be 100%. But due to air-leakage from the edges of the sample and from the mating surfaces, a reduced net effective change in porosity is observed.

5.2. Effect of hole depth on Darcy-Forchheimer Drag

The ratio of hole depth to diameter δ/D plays an imperative role in determining the flow characteristics through the perforated medium. Figure 5.4 presents the Darcy-Forchheimer drag in relation to the hole level Reynolds number Re_h for l_h = 3 mm sample. The hole diameter D = 0.8 mm is kept constant (0% closed hole orientation) and samples are tested for pressure drops (Section 4.1.1) at variable thickness δ = 10, 35, 50 and 60 mm corresponding to δ/D = 12.5, 43.7, 62.5 and 75 respectively. Eq. 2.17 describes the dependence of Darcy-Forchheimer drag on the pressure drop ΔP and Re_h [6]. It is recognized that the linear term of equation 2.17 or Darcy drag D^2/K increases with decrease in hole depth to diameter ratio δ/D at a constant porosity. Also, the increase in non-linear Forchheimer drag $\epsilon CDRe_h$, which is the slope of the curves in Figure 5.4 becomes less significant at higher δ/D ratios. When the curves are extrapolated back to Re_h = 0, a theoretical Darcy drag D^2/K is estimated for each δ/D configuration. Subsequently, Darcy-drag Flow Permeability $\mathrm{K}_{Darcy-drag}$ is back-calculated for each orientation and compared to Geometric Flow Permeability $\mathrm{K}_{geometric}$ from eq. 2.24. Table 5.2 lists out the extrapolated K from Darcy drag, the Geometric K and the absolute difference. The case for δ/D = 62.5 is considered to be an outlier due to possi-

ble misalignment of perforated channels due to absence of orientation pins in these experiments. It is observed that $K_{Darcy-drag}$ is higher than $K_{geometric}$ at all δ/D ratios. Potential reasons for the difference are:

- The formula for $K_{geometric}$ only predicts accurately for Re_h <25 whereas in current study its comparison is being drawn with $K_{Darcy-drag}$ that has been extrapolated back from a curve extending till Re_h = 590.
- Air-leakages from the edge of perforated disks lead to lower pressure losses across the sample, resulting in higher $K_{Darcy-drag}$.

Also, the $K_{Darcy-drag}$ for δ/D = 75 is exceptionally high in comparison to $K_{geometric}$. A possible reasoning for this is that δ/D = 75 orientation had three perforated disks assembled together (regular configuration) instead of one solid disk or two disks. In such cases, the possibility of seepage of air from the mating surfaces increases, thereby, increasing the flow permeability as well.

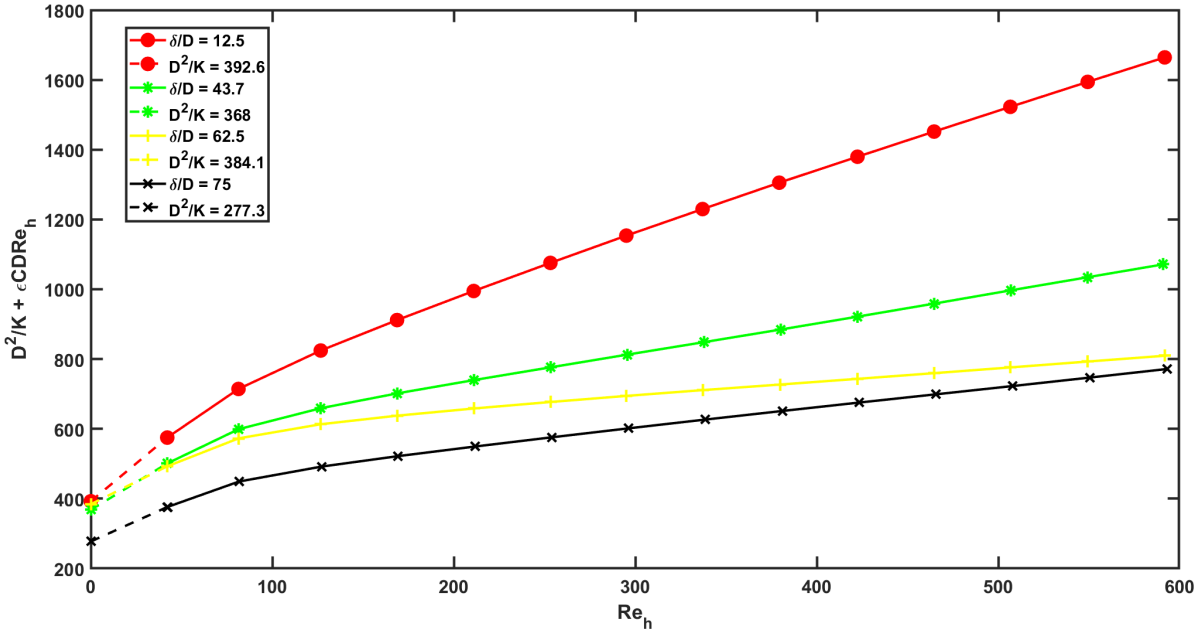

Figure 5.4: Variation of Darcy-Forchheimer drag with hole-level Reynolds number for different hole depth to diameter ratio (ϵ = 0.064)

Table 5.2: List of $K_{Darcy-drag}$ & $K_{geometric}$ for variable δ/D

δ/D	$K_{Darcy-drag}$	$K_{geometric}$	**Difference** (Δ)
75	2.307x 10^{-9}	1.282x10^{-9}	1.025
62.5	1.666x10^{-9}	1.28x10^{-9}	0.38
43.7	1.739x10^{-9}	1.276x10^{-9}	0.463
12.5	1.630x10^{-9}	1.243x10^{-9}	0.387

5.3. Variation of Flow Permeability with ϵ_{BEV} & ϵ_{Eff}

Figure 5.5 presents the Flow Permeability K for the Porosities ϵ calculated in Section 5.1.2 and listed in Table 5.1. As seen in the graph, the ϵ_{Eff} contracts the whole curve to smaller x-axis bounds. The ϵ_{Eff} for 100% closed hole orientation is calculated to be 0.042 which was initially presumed zero due to the premise of ϵ_{BEV} (See Table 5.1). Also, an important observation is that the upper bounds of ϵ_{Eff} are found to be lower than ϵ_{BEV}. The reason for this lies in Table 5.1 where the D_{Eff} for 0% closed hole orientation was calculated to be approx. 50μm lower than D_{BEV}. The cause of $D_{Eff} \neq D_{BEV}$ at 0% closed hole orientation is attributed to minor semi-closure of few holes at 0% closed hole orientation due to mis-positioning of the middle-disk while testing.

Another observation from Figure 5.5 is that the ϵ_{Eff} doesn't change much from 0% - 50% closed hole orientation and thereof doesn't reflect in significant changes of Flow Permeability K. This phenomenon was also observed in Section 4.3 and 4.4 wherein the Form Factor and Flow Resistivity remained fairly uniform till 50% hole closure.

Therefore, it can be concluded that significant variation in Flow Permeability and Effective Porosity can only be gauged at post-50% closure of holes in a Middle-Disk Shift mechanism.

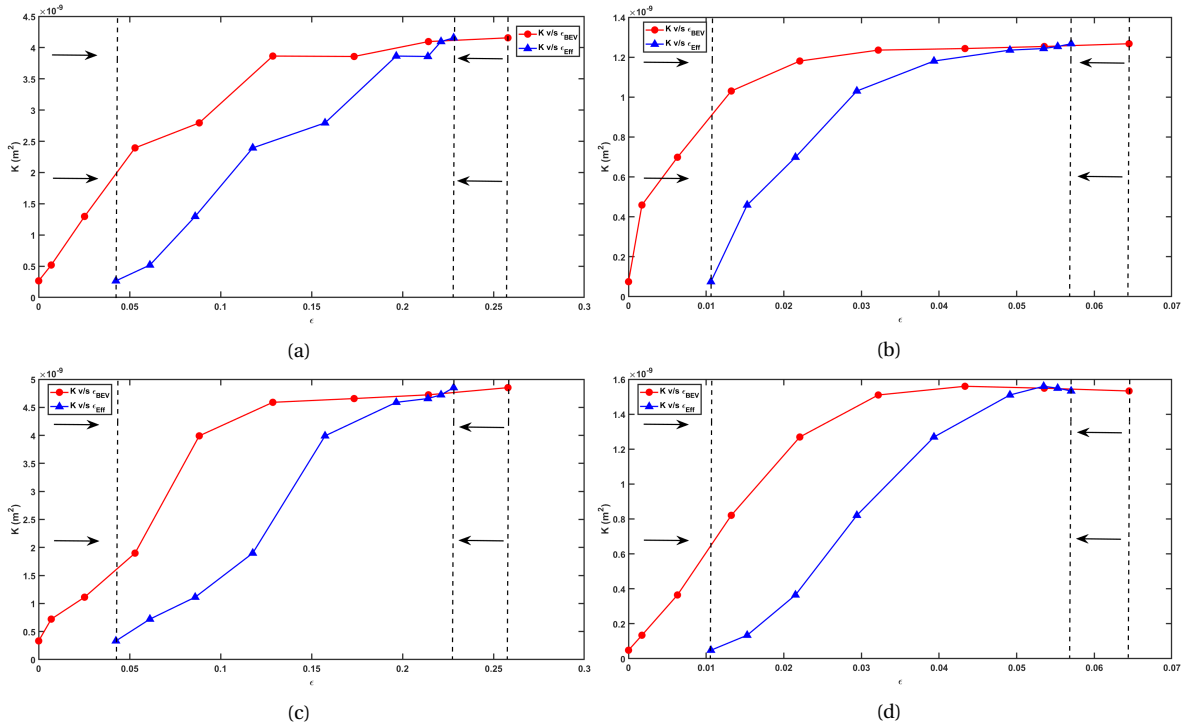

Figure 5.5: Flow Permeability v/s Bird's Eye View Porosity & Effective Porosity; (a) l_h = 1.5 mm Static configuration; (b) l_h = 3 mm Static configuration; (c) l_h = 1.5 mm Dynamic configuration; and (d) l_h = 3 mm Dynamic configuration

5.4. Static configuration v/s Dynamic configuration

5.4.1. l_h = 1.5 mm and 3 mm sample

Figures 5.6 and 5.7 present a comparison between the Flow Permeability K variations in the static and dynamic set-up for the l_h = 1.5 mm and 3 mm perforated disks plotted against the effective porosity ϵ_{Eff}. In Figure 5.6, the permeability is closely related to each other

for both set-up from ϵ_{Eff}≈0.04 up until ϵ_{Eff}≈0.12 or 62.5% closed hole orientation. Subsequently, the permeability for dynamic setup increases compared to its counter-part and remains higher at large by an average magnitude of ΔK≈0.6 x 10^{-9} m^2. This was expected since there are potentially more regions of air-leakages in the actuation device manufactured for dynamic configuration set-up, as discussed in section 3.5. For both set-ups, the curve effectively starts flattening at $\epsilon_{Eff} \approx 0.2$ or 37.5% closed hole orientation. As discussed in Table 5.1, the effective hydraulic diameter stays constant post-37.5% stage and hence a flattening of K curve is expected.
In Figure 5.7, K_{static} shows higher permeability in the region of ϵ_{Eff}≈0.01 to ϵ_{Eff}≈0.04, after which the trend reverses. According to the assumptions of this paper, this trend is an outlier since the static setup is considered to be more effective in blocking air-leakage resulting in lower Flow Permeability K. All but one curve of the $K_{dynamic}$ flatten out post-37.5% closed hole orientation ($\epsilon_{Eff} \approx 0.05$), thereby following the trend set by other perforated disks in previous graphs.
Therefore, by application of Middle-Disk Shift mechanism, a variation of Flow Permeability of $\Delta K_{1.5mm}$ >4.5x10^{-9} m^2 and ΔK_{3mm} >1.4x10^{-9} m^2 can be achieved.

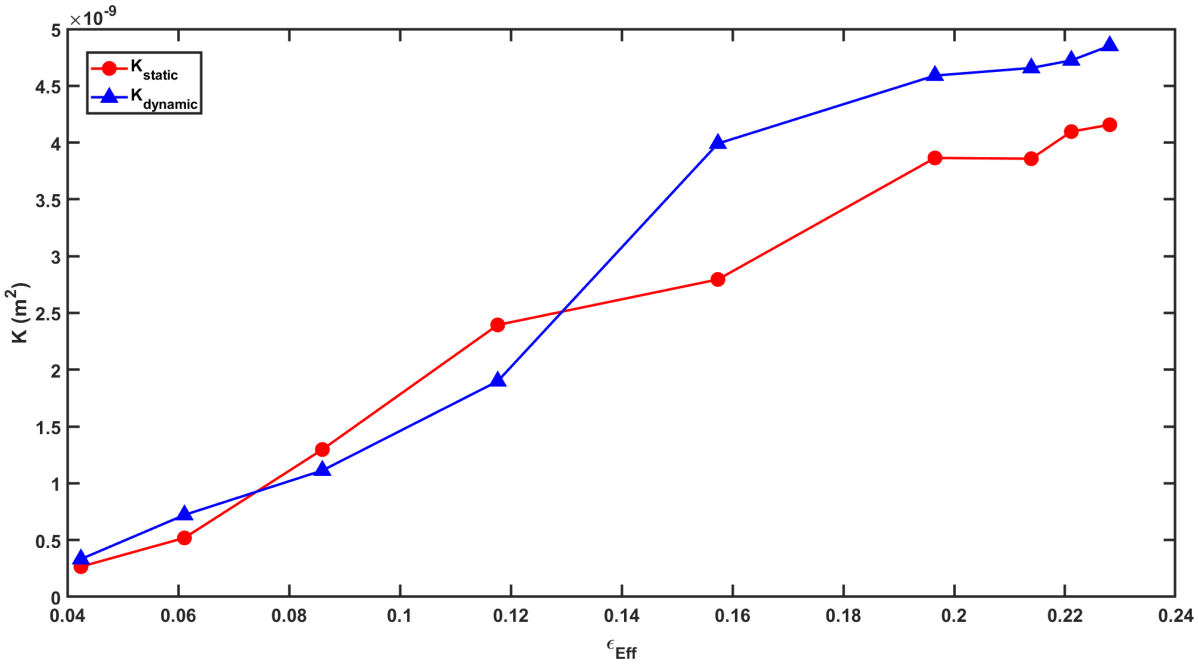

Figure 5.6: Flow Permeability v/s Effective Porosity of l_h = 1.5 mm for Static and Dynamic configuration

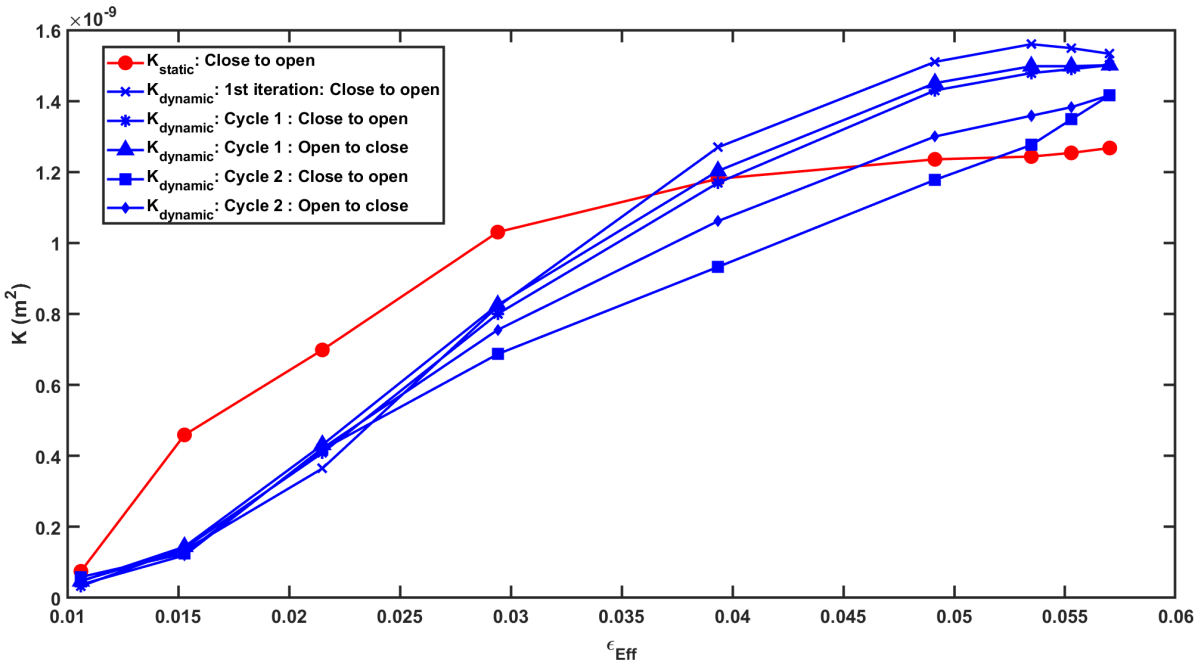

Figure 5.7: Flow Permeability v/s Effective Porosity of l_h = 3 mm for Static and Dynamic configuration

5.4.2. Master plot

The combined plot for the variations in Flow Permeability (K) with the Effective Porosity (ϵ_{Eff}) for each perforated sample is displayed in Figure 5.8. It is evident that the effect of middle -disk shift mechanism is more pronounced in l_h = 1.5 mm sample but an important observation is made for the domain of $\epsilon_{Eff} \approx 0.04$ to 0.06. This is the sole region where $K_{1.5mm}$ and K_{3mm} lie in the same porosity domain. Although the ϵ_{Eff} is found to be similar in both cases but the calculated Permeability K varies by an approximate magnitude of $0.7x10^{-9}$. There are multiple reasons for different K values for each curve:

- The $K_{1.5mm}$ is calculated for the 87.5% - 100% closed hole orientation whereas K_{3mm} belongs to 0% - 50% closed hole orientation. Due to changes in orientation, the effect of tortuosity Γ comes into play which can't be completely mapped or characterized in the present scope of work. Although it can be acknowledged that more tortuosity certainly existed for $K_{1.5mm}$, as listed in Table 5.1 which made the perforated medium less permeable.

- Due to a higher level of tortuosity in the system for l_h = 1.5 mm sample, the inertial effects of the fluid flow are potentially stronger as seen by the Form factor in Section 4.3. These inertial parameters play a major role in semi-closed or almost-closed hole orientations due to deviation of fluid-flow from a straight path, thereby, affecting the flow permeability of the model.

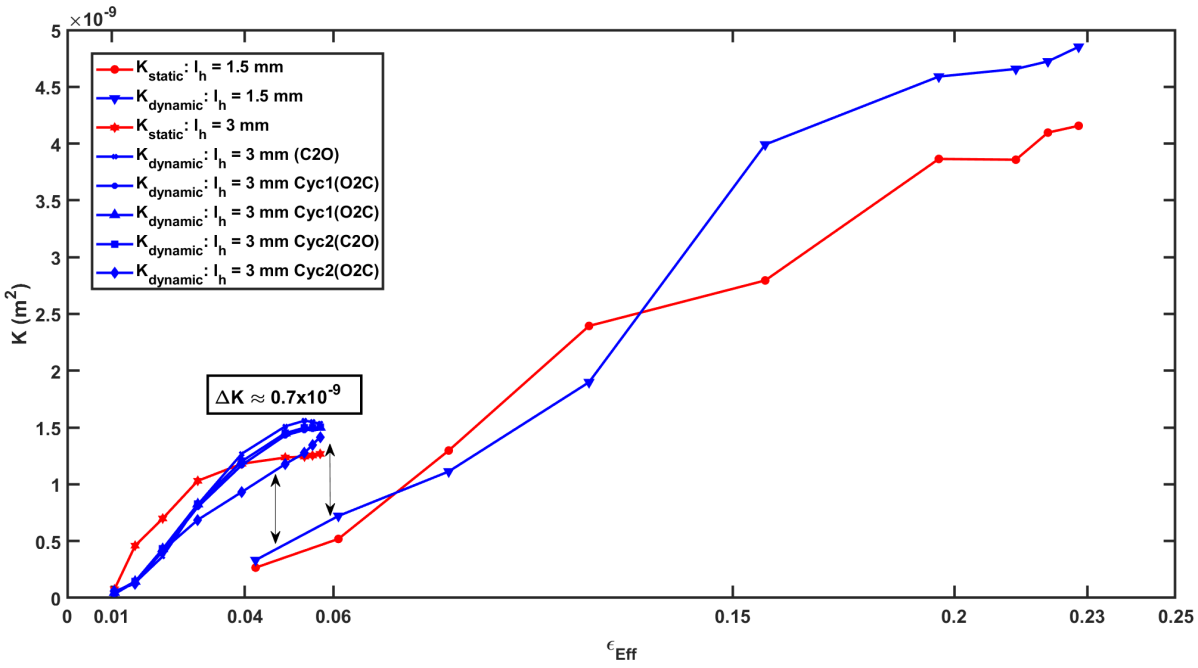

Figure 5.8: Flow Permeability v/s Effective Porosity combined plot

5.5. Relation of K/ϵ_{Eff} with hole closure

Figure 5.9 presents a parameter K/ϵ_{Eff} that maps the change in Flow Permeability and Porosity at each hole closure orientation. The said parameter weighs the effect of hole closure orientation (geometric middle-disk position) on actual variation in K and ϵ_{Eff}. From 100% closed hole orientation - 50% closed orientation, divergence in K is greater than effective contrast in porosity of the system. This is translated to a larger rate of drop in K with respect to ϵ_{Eff} for post-50% hole closure. On the other hand, in the pre-50% hole closure domain, the alteration in K is equally balanced out by changes in ϵ_{Eff} that suggest an overall uniformity in the K/ϵ_{Eff} of the system even though the middle-disk shifts 0.4 mm.
A deviation in the trendline is observed for the curve of K_{static}: l_h = 3 mm. The three data points (87.5%,75% and 62.5% closed hole) are considered to be an outlier.
Therefore, Figure 5.9 advocates that Middle-Disk Shift mechanism plays a conclusive role in the post-50% closed hole orientation for a system of circular perforated hole plates. Therefore, if applied to real-life structures, that is, on trailing edge of an airfoil, the disposition of the middle disk should be at half-closed orientation. The finding throws light on the stroke and force required for an actuation system to operated the Middle-Disk Shift mechanism in real-life structures.

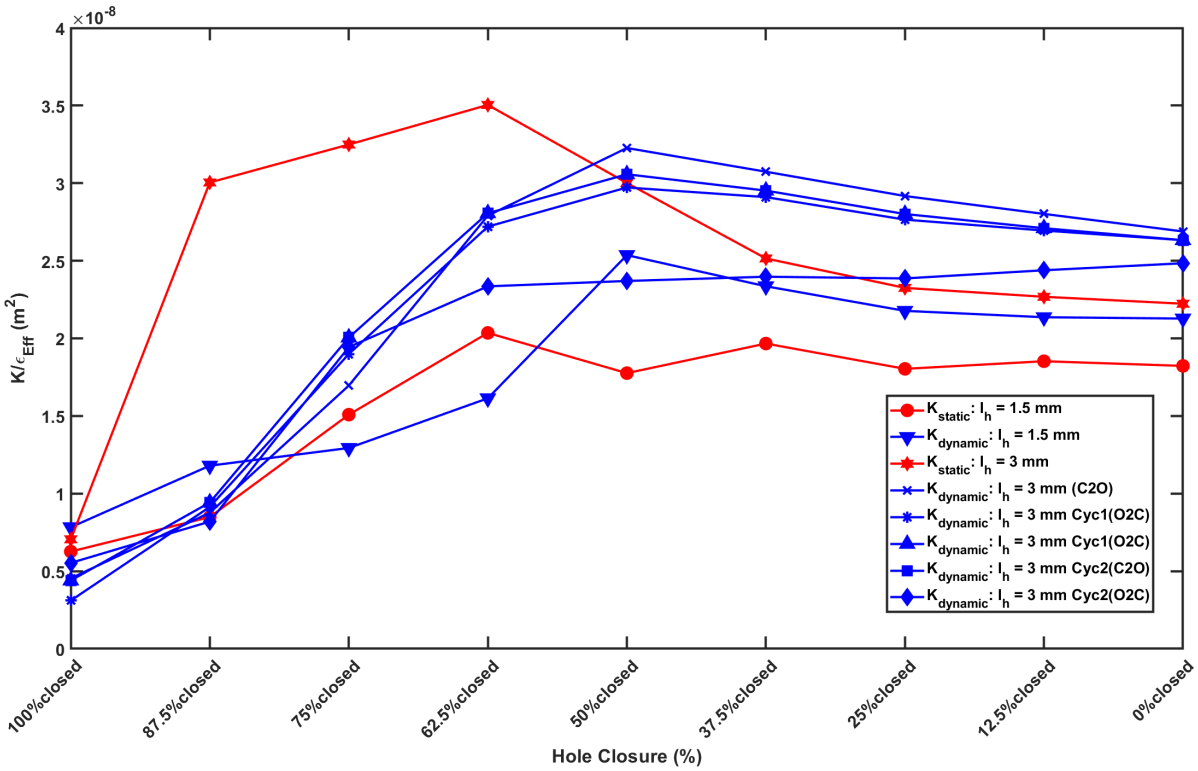

Figure 5.9: Variation of Flow Permeability & Effective Porosity with hole closure

6

Conclusion and Future Recommendations

The broader intent of this research was to demonstrate that an actuation system can alter the flow permeability and porosity of semi-permeable inserts. Thus, was achieved by employing a Middle-Disk shift mechanism. Section 6.1 summarizes the findings from this report and reflects on the extent of completion of research objectives. And, section 6.2 provides recommendations to diversify this research in the future.

6.1. Conclusion

In principle, the active control of perforated channel trailing edge inserts was demonstrated. A novel static set-up for 3-D perforated disks with orientation pins was devised that implemented the concept of Middle-Disk Shift mechanism. The results of pressure drop tests ΔP, flow permeability K, flow resistivity R and form factor C in the laminar regime suggested a non-linear decrease in the flow parameters with respect to hole closure in Middle-Disk Shift mechanism. A comprehension of the trend-line for each parameter was approached through multiple directions to improve characterization of the mechanics of fluid flow across perforated plates. Post-analysis of the fluid flow, a dynamic set-up was designed and constructed which could, in essence, replicate the results of the static set-up experiments. The selection of a suitable actuation system for dynamically changing the flow parameters and the challenges faced in developing the actuation devices were addressed in the research. The dynamic system was tailored to have the potential to be upgraded to real structures, that is, trailing edge of aircraft and wind turbines with suitable modifications. The flow parameters calculated from the dynamic set-up closely followed that of static set-up which established a good degree of repeatablity of the actuation system. It was important to note that flow permeability K, in general, was found to be higher for dynamic set-up due to more chances of air-leakage from the set-up. The following paragraphs lists the imperative inferences drawn from this research regarding the transpiration flow across perforated plates at varying porosity.

The non-linear increase in differential pressure ΔP obtained for linearly incremental flow velocity was addressed. Also, the non-linear drop in ΔP for subsequent hole closure orientations, obtained by linear displacement of middle-disk, was studied. The characteristics of fairly undermined viscous effects and the overwhelming inertial effects of fluid flow at higher hole level Reynolds number, Re_h, and smaller effective hydraulic diameters D_{Eff} were postulated. They non-Darcian effects, for Re_h>5 were demonstrated to be greatly

responsible for non-linearity of fluid flow. The viscous and inertial effects and their dependence on the hole depth to diameter ratio δ/D were further illustrated with the help of Darcy-Forchheimer drag. It was confirmed experimentally that the linear Darcy drag D^2/K showed higher significance at lower δ/D at constant porosity ϵ while the rate of increase of non-linear Forchheimer drag $\epsilon CDRe_h$ became smaller at higher δ/D ratios. Additionally, a virtual $K_{Darcy-drag}$, that ignores the effects of Forchheimer constant, was computed and compared to $K_{geometric}$ to understand the viscous and geometric effects on the Flow Permeability K in a transpiration flow.
The non-linear decrease in pressure drops ΔP and Flow Permeability K with respect to hole closure were ascribed to a non-linear reduction in effective porosity ϵ_{Eff}. Although, ϵ_{Eff} was back-calculated assuming only major losses in the pipe due to wall friction, it proved to be a good estimate for characterizing the uniformity in flow parameters in the 0% to 50% closed hole orientation. A major conclusion drawn from this observation was that Middle-Disk Shift mechanism works effectively in the range of 50% closed hole to completely shut hole orientations.
Another important observation made from the application of Middle-Disk Shift mechanism was that it was effective in reducing the overall porosity of the semi-permeable system by 72%. The rest was accounted as air-leakage. Another factor, Tortuosity Γ, was geometrically calculated but wasn't directly linked to flow permeability K or form factor C but it was theorized that increase in tortuosity of the perforated channel led to a higher normal/transverse forces on the fluid flowing through a straight line. This resulted in significant increase in the form factor of the sample.
Lastly, a new parameter was introduced called K/ϵ_{Eff} that combined the ratio of non-linear changes in flow permeability K & effective porosity ϵ_{Eff} with linear changes in middle-disk positions. The variation in K/ϵ_{Eff} parameter postulated that the divergence in K is higher than that of ϵ_{Eff} for 100% to 50% closed hole orientation after which they neutralize each other out. Hence, it reinstated the proposal that Middle-Disk Shift mechanism plays a conclusive role post-50% closed hole orientation for circular perforated channel plates.
Therefore, it can be concluded that the Middle-Disk shift mechanism was effective in varying flow parameters and porosity of perforated channel samples in both static and dynamic configuration set-ups with good degree of precision. Thus, the mechanism proposed has, in principle, a potential to be upgraded to real structures after further optimization.

6.2. Future Recommendations

The study on creating semi-permeable trailing edge inserts has several dimensions that were unexplored by this research. Following are some areas of work that can possibly throw more light on the design of inserts:

- The acoustic measurements for an actively controlled semi-permeable insert based on the current mechanism will be crucial to the future of this field of work. It would be interesting to observe if the results of active semi-permeable inserts match that of passive inserts shown in Figure 1.12 of this report.

- The current study focused on shifting a mid-plane to achieve overall variation in porosity of the insert. Instead, meta-materials or elastomers can be deployed to change the hydraulic diameter, end-to-end, of the perforated channel by contracting and expanding the holes. This would possibly be more effective in varying the

porosity and flow parameters of an insert but could be limited by the geometrical hole spacing l_h.

- The use of non-circular perforated holes was out of the scope of this research. It would be interesting to observe the trend of variation in flow parameters for a square- or triangle- shaped perforated channels.

- The characteristics of boundary layer and re-circulation zones in the perforated holes weren't incorporated in the present field of work. Describing the boundary layer formation and its variation with a middle-disk shift mechanism would throw more light on change in the flow parameters- permeability, resistivity and form factor.

- The application of middle-disk shift mechanism for a turbulent flow regime, Re_p>4000 can be the next step for this research. It can be proposed, from current knowledge, that the effectiveness of middle-disk shift could increase for turbulent regime due to eddy formations in the mid-plane, thereby, reducing the overall D_{Eff} of the flow better than in a laminar regime.

- Instead of using a single mid-plane to reduce the hydraulic diameter D_{Eff} of the insert, a set of multiple mid-planes could be deployed that could work in a synchronized manner and vary their position in incremental steps. For example: Mid-disk A shifts by 0.1 mm, Mid-disk B shifts by 0.2 mm etc., thereby, creating steps within the perforated insert. This could potentially improve the porosity variation of the insert as compared to a single mid-disk.

- If research is continued further on using a single middle-disk, then varying the ratio of thickness of middle-disk to top & bottom disk will be crucial to the potency of this mechanism. It can be predicted that higher the ratio, better will be the control over porosity variation.

Bibliography

[1] J. Adams. Transport planning: vision and practice. 1981. ISSN 00018392. doi: https://doi.org/10.2307/2392332.

[2] F. Allard and Y. Utsumi. Airflow through large openings. *Energy and Buildings*, 18(2): 133 – 145, 1992. ISSN 0378-7788. doi: https://doi.org/10.1016/0378-7788(92)90042-F.

[3] C. Arce León, D. Ragni, S. Pröbsting, F. Scarano, and J. Madsen. Flow topology and acoustic emissions of trailing edge serrations at incidence. *Experiments in Fluids*, 57 (5):1–17, 2016. ISSN 07234864. doi: https://doi.org/10.1007/s00348-016-2181-1.

[4] B. Arnold, T. Lutz, and E. Krämer. Design of a boundary-layer suction system for turbulent trailing-edge noise reduction of wind turbines. *Renewable Energy*, 123(January): 249–262, 2018. ISSN 18790682. doi: https://doi.org/10.1016/j.renene.2018.02.050.

[5] F. Avallone, W. C.P. van der Velden, and D. Ragni. Benefits of curved serrations on broadband trailing-edge noise reduction. *Journal of Sound and Vibration*, 400(April): 167–177, 2017. ISSN 10958568. doi: https://doi.org/10.1016/j.jsv.2017.04.007.

[6] Y. Bae and Y. In Kim. Numerical modeling of anisotropic drag for a perforated plate with cylindrical holes. *Chemical Engineering Science*, 149:78 – 87, 2016. ISSN 0009-2509. doi: https://doi.org/10.1016/j.ces.2016.04.036.

[7] J. Bear. *Dynamics of fluids in porous media*. 1972. ISBN 9780486656755. URL `https://books.google.nl/books?id=lurrmlFGhTEC`.

[8] G. Brown. The history of the darcy-weisbach equation for pipe flow resistance. *Proc. Environ. Water Resour. Hist.*, 38, 10 2002. doi: https://doi.org/10.1061/40650(2003)4.

[9] S. Bütefisch, V. Seidemann, and S. Büttgenbach. Novel micro-pneumatic actuator for MEMS. *Sensors and Actuators, A: Physical*, 97-98:638–645, 2002. ISSN 09244247. doi: https://doi.org/10.1016/S0924-4247(01)00843-3.

[10] T. P. Chong and A. Vathylakis. On the aeroacoustic and flow structures developed on a flat plate with a serrated sawtooth trailing edge. *Journal of Sound and Vibration*, 2015. ISSN 10958568. doi: https://doi.org/10.1016/j.jsv.2015.05.019.

[11] I. A. Clark. Bio-Inspired Control of Roughness and Trailing Edge Noise Bio-Inspired Control of Roughness and Trailing Edge Noise. 2017. URL `http://hdl.handle.net/10919/77531`.

[12] EnvisionTEC. EnvisionTEC R5 polymer technical data. URL `https://envisiontec.com/3d-printing-materials/micro-materials/r5/`. [Online; accessed 20-October-2020].

[13] S. Ergun. Fluid flow through packed columns. *Chemical Engineering Progress*, 48:89–94, 1986. URL http://dns2.asia.edu.tw/~ysho/YSHO-English/1000%20CE/PDF/Che%20Eng%20Pro48,%2089.pdf.

[14] J. M. Fields. Effect of personal and situational variables on noise annoyance in residential areas. *Journal of the Acoustical Society of America*, 93(5):2753–2763, 1993. ISSN NA. doi: https://doi.org/10.1121/1.405851.

[15] A. Finez, E. Jondeau, M. Roger, and M. C. Jacob. Broadband noise reduction with trailing edge brushes. *16th AIAA/CEAS Aeroacoustics Conference (31st AIAA Aeroacoustics Conference)*, pages 1–13, 2010. doi: https://doi.org/10.2514/6.2010-3980.

[16] P. Forchheimer. Wasserbewegung durch boden zeit. *Ver. Deut. Ing.*, page 45, 1782-1788. URL https://ci.nii.ac.jp/naid/10010395788/en/.

[17] L. Garcillán, M. Fisher, K. Koegler, and T. Maeder. Sirocco: Silent rotors by acoustic optimisation. *Second International Meeting on Wind Turbine Noise, Lyon, France*, 1:596–606, 2007. URL https://repository.tudelft.nl/view/tno/uuid%3Add5d1290-3095-45f8-a170-d24c64bcddf8.

[18] T. Gerhard, S. Erbslöh, and T. Carolus. Reduction of airfoil trailing edge noise by trailing edge blowing. *Journal of Physics: Conference Series*, 524(1), 2014. ISSN 17426596. doi: https://doi.org/10.1088/1742-6596/524/1/012123.

[19] T. Geyer and E. Sarradj. Trailing edge noise of partially porous airfoils. *20th AIAA/CEAS Aeroacoustics Conference*, (June), 2014. doi: https://doi.org/10.2514/6.2014-3039.

[20] T. Geyer and E. Sarradj. Self Noise reduction and aerodynamics of airfoils with porous trailing edges. *Inter-Noise 2018 - 47th International Congress and Exposition on Noise Control Engineering: Impact of Noise Control Engineering*, pages 393–409, 2018. ISSN 2624-599X. doi: https://doi.org/10.3390/acoustics1020022.

[21] T. Geyer, E. Sarradj, and C. Fritzsche. Porous airfoils: Noise reduction and boundary layer effects. *International Journal of Aeroacoustics*, 9(6):787–820, 2010. doi: https://doi.org/10.1260/1475-472X.9.6.787.

[22] R. Hedayati, A. Rubio Carpio, S. Luesutthiviboon, D. Ragni, F. Avallone, D. Casalino, and S. van der Zwaag. Role of polymeric coating on metallic foams to control the aeroacoustic noise reduction of airfoils with permeable trailing edges. *Materials*, 12 (7), 2019. ISSN 19961944. doi: https://doi.org/10.3390/ma12071087.

[23] M. Herr. Design criteria for low-noise trailing-edges. *13th AIAA/CEAS Aeroacoustics Conference (28th AIAA Aeroacoustics Conference)*, pages 1–14, 2007. doi: https://doi.org/10.2514/6.2007-3470.

[24] M. Herr, K. S. Rossignol, J. Delfs, M. Mößner, and N. Lippitz. Specification of porous materials for low-noise trailing-edge applications. *20th AIAA/CEAS Aeroacoustics Conference*, (June):1–19, 2014. doi: https://doi.org/10.2514/6.2014-3041.

[25] M. S. Howe. Aerodynamic noise of a serrated trailing edge. *Journal of Fluids and Structures*, 5(1):33–45, 1991. ISSN 10958622. doi: https://doi.org/10.1016/0889-9746(91)80010-B.

[26] F. Howes and S. Whitaker. The spatial averaging theorem revisited. *Chemical Engineering Science*, pages 1387–1392, 07 1985. doi: https://doi.org/10.1016/0009-2509(85)80078-6.

[27] D. Rosen I. Gibson and B. Stucker. Additive manufacturing technologies. *Springer New York*, 2015. doi: https://doi.org/10.1007/978-1-4939-2113-3.

[28] N. Lippitz M. Lummer M. M¨oßner L. M¨uller K. Rurkowska J. Delfs, B. Faßmann and S. Uphoff. Sfb 880: Aeroacoustic research for low noise take-off and landing. 2014. doi: https://doi.org/10.1007/s13272-014-0115-2.

[29] R. F.S. Job. Community response to noise: A review of factors influencing the relationship between noise exposure and reaction. *Journal of the Acoustical Society of America*, 83(3):991–1001, 1988. doi: https://doi.org/10.1121/1.396524.

[30] L. E. Jones and R. D. Sandberg. Acoustic and hydrodynamic analysis of the flow around an aerofoil with trailing-edge serrations. *Journal of Fluid Mechanics*, 706:295–322, 2012. ISSN 00221120. doi: https://doi.org/10.1017/jfm.2012.254.

[31] R. F. Jones, C. J. Doolan, and M. D. Teubner. Minimization of trailing edge noise by parametric airfoil shape modifications. *17th AIAA/CEAS Aeroacoustics Conference 2011 (32nd AIAA Aeroacoustics Conference)*, (June):5–8, 2011. doi: https://doi.org/10.2514/6.2011-2782.

[32] A. Kisil and L. J. Ayton. Aerodynamic noise from rigid trailing edges with finite porous extensions. *Journal of Fluid Mechanics*, 836:117–144, 2018. doi: https://doi.org/10.1017/jfm.2017.782.

[33] G. Lebon and A. Cloot. A thermodynamical modelling of fluid flows through porous media: application to natural convection. *International Journal of Heat and Mass Transfer*, 29(3):381 – 390, 1986. ISSN 0017-9310. doi: https://doi.org/10.1016/0017-9310(86)90208-5.

[34] S.L. Lee and J.H. Yang. Modeling of darcy-forchheimer drag for fluid flow across a bank of circular cylinders. *International Journal of Heat and Mass Transfer*, 40(13):3149 – 3155, 1997. ISSN 0017-9310. doi: https://doi.org/10.1016/S0017-9310(96)00347-X.

[35] Z. Lu, M. Shrestha, and G. K. Lau. Electrically tunable and broader-band sound absorption by using micro-perforated dielectric elastomer actuator. *Applied Physics Letters*, 110(18), 2017. ISSN 00036951. doi: https://doi.org/10.1063/1.4982634.

[36] E. Maris, P. J. Stallen, R. Vermunt, and H. Steensma. Noise within the social context: Annoyance reduction through fair procedures. *The Journal of the Acoustical Society of America*, 121(4):2000–2010, 2007. ISSN 0001-4966. doi: https://doi.org/10.1121/1.2535507.

[37] A. L. Marsden, M. Wang, J. E. Dennis, and P. Moin. Trailing-edge noise reduction using derivative-free optimization and large-eddy simulation. *Journal of Fluid Mechanics*, 572:13–36, 2007. ISSN 00221120. doi: https://doi.org/10.1017/S0022112006003235.

[38] A.A.F. Miguel. *Transport phenomena through porous screens and openings: from theory to greenhouse practice*. 1998. ISBN 0-5485-847-8. URL `https://edepot.wur.nl/212243`.

[39] D. J. Moreau and C. J. Doolan. Noise-reduction mechanism of a flat-plate serrated trailing edge. *AIAA Journal*, 51(10):2513–2522, 2013. ISSN 00011452. doi: https://doi.org/10.2514/1.J052436.

[40] S. Moreau, B. Dignou, P. Jaiswal, G. R. Yakhina, Y. Pasco, M. Sanjose, B. Alstrom, and N. Atalla. Trailing-edge noise of a flat plate with several liner-type porous appendices. 2018. doi: https://doi.org/10.2514/6.2018-3119.

[41] PI Motion|Positioning. High-resolution linear actuator with stepper motor (m-228.m-229). URL `https://static.pi-usa.us/fileadmin/user_upload/physik_instrumente/files/datasheets/M-228-Datasheet.pdf`. [Online; accessed 18-October-2020].

[42] A. Nakayama. A unified treatment of darcy-forchheimer boundary-layer flows. In *Transport Phenomena in Porous Media*, pages 179 – 204. Pergamon, Oxford, 1998. ISBN 978-0-08-042843-7. doi: https://doi.org/10.1016/B978-008042843-7/50008-8.

[43] S. Oerlemans. *Detection of aeroacoustic sound sources on aircraft and wind turbines*. PhD thesis, University of Twente, Netherlands, 9 2009.

[44] S. Oerlemans, P. Sijtsma, and B. Méndez López. Location and quantification of noise sources on a wind turbine. *Journal of Sound and Vibration*, 299(4):869 – 883, 2007. ISSN 0022-460X. doi: https://doi.org/10.1016/j.jsv.2006.07.032.

[45] J. Ortmann and J. Wild. Effect of acoustic slat modifications on aerodynamic properties of high-lift systems. *Journal of Aircraft*, 44(4):1258–1263, 2007. ISSN 00218669. doi: https://doi.org/10.2514/1.26307.

[46] J. Piet, R. Davy, G. Elias, H. Siller, L. Chow, C. Seror, and F. Laporte. Flight test investigation of add-on treatments to reduce aircraft airframe noise. 05 2005. doi: https://doi.org/10.2514/6.2005-3007.

[47] A. Rubio Carpio, F. Avallone, D. Ragni, M. Snellen, and S. van der Zwaag. 3D-printed Perforated Trailing Edges for Broadband Noise Abatement. pages 1–13, 2019. doi: https://doi.org/10.2514/6.2019-2458.

[48] A. Rubio Carpio, F. Avallone, D. Ragni, M. Snellen, and S. van der Zwaag. Mechanisms of broadband noise generation on metal foam edges. *Physics of Fluids*, 31(10):105–110, 2019. doi: https://doi.org/10.1063/1.5121248.

[49] A. Rubio Carpio, R. M. Martínez, F. Avallone, D. Ragni, M. Snellen, and S. van der Zwaag. Experimental characterization of the turbulent boundary layer over a porous

trailing edge for noise abatement. *Journal of Sound and Vibration*, 443:537–558, 2019. ISSN 10958568. doi: https://doi.org/10.1016/j.jsv.2018.12.010.

[50] A. Rubio Carpio, F. Avallone, D. Ragni, M. Snellen, and S. van der Zwaag. Quantitative criteria to design optimal permeable trailing edges for noise abatement. *Journal of Sound and Vibration*, 485:115596, 2020. ISSN 0022-460X. doi: https://doi.org/10.1016/j.jsv.2020.115596.

[51] E. Sarradj and T. Geyer. Noise generation by porous airfoils. *13th AIAA/CEAS Aeroacoustics Conference (28th AIAA Aeroacoustics Conference)*, 2007. doi: https://doi.org/10.2514/6.2007-3719.

[52] J. Shah. Aeroacoustics and Flow Dynamics of an airfoil with a Gurney Flap. 2015. URL `http://resolver.tudelft.nl/uuid:f02e0a9c-9ef4-4d61-8617-fadb199a87e7`.

[53] J. C. Slattery. Flow of viscoelastic fluids through porous media. *AIChE Journal*, 13(6):1066–1071, 1967. doi: https://doi.org/10.1002/aic.690130606.

[54] W. Sutherland. LII. The viscosity of gases and molecular force . *The London, Edinburgh, and Dublin Philosophical Magazine and Journal of Science*, 36(223):507–531, 1893. ISSN 1941-5982. doi: https://doi.org/10.1080/14786449308620508.

[55] K. Vafai and C.L. Tien. Boundary and inertia effects on flow and heat transfer in porous media. *International Journal of Heat and Mass Transfer*, 24(2):195 – 203, 1981. ISSN 0017-9310. doi: https://doi.org/10.1016/0017-9310(81)90027-2.

[56] S. Whitaker. Flow in porous media i: A theoretical deviation of darcy's law. *Transport in Porous media*, 1:3–25, 1986. doi: https://doi.org/10.1007/BF01036523.

[57] D. Yang, M. S. Verma, J. H. So, B. Mosadegh, C. Keplinger, B. Lee, F. Khashai, E. Lossner, Z. Suo, and G. M. Whitesides. Buckling Pneumatic Linear Actuators Inspired by Muscle. *Advanced Materials Technologies*, 1(3):31–33, 2016. ISSN 2365709X. doi: https://doi.org/10.1002/admt.201600055.

[58] E.B. Yousef. Noise regulation. In *The Evolution of the US Airline Industry: Theory, Strategy and Policy*, pages 137–167. Springer US, Boston, MA, 2005. ISBN 978-0-387-24242-2. doi: https://doi.org/10.1007/0-387-24242-2_7.

A

Basic formulation of method of volume averaging

The averaging volume for a homogeneous two-phase system (solid matrix and fluid) is given by :

$$V = V_s + V_f \tag{A.1}$$

where V_s and V_f are the volume of solid and fluid in the averaging volume, respectively.
The fluid porosity is expressed as:

$$\epsilon = \frac{V_f}{V} \tag{A.2}$$

The average of local quantity Λ (fluid veloctiy, fluid pressure) in the averaging volume can be expressed in terms of superficial (external) phase average or intrinsic (internal) phase average. The intrinsic phase average is defined as:

$$< \Lambda >_i = V_f^{-1} \int \Lambda dV \tag{A.3-1}$$

and the superficial phase average is given as:

$$< \Lambda > = V^{-1} \int \Lambda dV \tag{A.3-2}$$

The two averages are related through porosity as:

$$< \Lambda > = \epsilon < \Lambda >_i \tag{A.4}$$

The local value of Λ can also be related to phase average by(5miguel):

$$\Lambda = < \Lambda >_i + \tilde{\Lambda} \tag{A.5}$$

where Λ is spatial deviation of Λ compared to $< \Lambda >_i$.
During the analysis of governing equations of transport phenomena in porous media, the differentiation and integration expressions are sometimes interchanged in order to present the quantity in form of intrinsic phase average. The spatial averaging theorem [26, 53] is used for this process given in vector form by:

$$< \nabla . \Lambda >_i = \nabla . < \Lambda >_i + V^{-1} \int n . \Lambda dA \tag{A.6}$$

where n is unit vector and A is inter-facial area present within averaging volume.
Substitution of eq. A.5 in eq. A.6 gives :

$$< \nabla.\Lambda >_i = \nabla. < \Lambda >_i + V_f^{-1} \int n. < \Lambda >_i \, dA + V_f^{-1} \int n.\tilde{\Lambda} dA \tag{A.7}$$

B

3-D printing polymer specification sheet

This appendix lists the material properties of the R5 polymer used to 3-D print all the perforated disks in this study. R5 is a liquid photopolymer that creates tough and accurate functional parts. It offers high chemical resistance, tolerance to broader operating temperatures and good processability. Products made from R5 showcase excellent fatigue properties, strong memory retention and high quality up-facing and down-facing. Table B lists material properties of the R5 polymer.

Table B.1: Material properties of R5 polymer [12]

Material Property	**Value**
Tensile Strength	31-39 MPa
Elongation at Break	11-25%
Elongation at Yield	16%
Modulus of Elasticity	1,245-1,510 MPa
Flexural Strength	40-45 MPa
Flexural Modulus	1,190 - 1,383 MPa
Izod Impact - Notched	0.2 - 0.50 J/cm
Hardness (Shore D)	81 Shore
Water Absorption	0.78%
Graves Tear	154,287 N/m

C

Stepper motor specification sheet

This appendix presents the technical details of the stepper motor selected for the actuation device in the dynamic configuration set-up. The stepper motor was purchased from Physik Instrumente (PI) GmbH Co. KG and its model number was M-229.26S. It was used in conjunction with C-663.12 Mercury Step single-channel controller for single-axis configuration. Table C.1 lists technical specifications of the motor.

Table C.1: Stepper motor specification sheet[41]

Parameter	M-229.26S	Unit	Tolerance
Motion and Positioning			
Travel range	25	mm	
Design resolution	0.00061	μm	Typ
Backlash	10	μm	Typ
Unidirectional repeatability	±2	μm	Typ
Velocity	4	mm/s	Typ
Reference switch repeatability	1	μm	Typ
Minimum incremental motion	1	μm	Typ
Mechanical properties			
Drive screw type	Leadscrew		
Drive screw pitch	0.5	mm	
Gear ratio	-		
Push/pull force	80	N	Max
Drive properties			
Motor type	2-phase stepper motor		
Step resolution	400	Steps/rev	
Nominal current per phase	850	mA	Max
Reference and limit switches	Hall effect		
Miscellaneous			
Operating temperature range	-20 to 65	^{o}C	
Material	Anodized aluminium, chrome steel, brass		
Mass	0.61	Kg	±5%
Cable length	0.6	m	±10 mm
Connector	D-sub 15 (m)		
Recommended controller	C-663.12		

D

List of Mass flow rates, pipe-level Reynolds number Re_p and hole-level Reynolds number Re_h

This appendix lists the Mass Flow Rates (Kg/s) that were inputted to the permeability rig for the measurement of pressure drop ΔP for different specimens and orientations. The corresponding Reynolds number at pipe level is given as: $Re_p = \frac{\rho V D_p}{\mu}$, where ρ is the temperature density of air (Kg/m^3), V is the flow velocity (m/s), D_p is the diameter of the pipe and μ is the temperature dependant viscosity of air (Pa.s).

Table D.1: Pipe-level Reynolds number for input Mass flow rate

Mass flow rate m^*	**Reynolds number** Re_p
0.0001215	169.181
0.0002340	327.318
0.0003645	509.560
0.0004855	678.763
0.0006070	848.679
0.0007285	1018.495
0.0008500	1188.639
0.0009715	1357.547
0.0010930	1526.951
0.0012145	1696.595
0.0013355	1867.776
0.0014570	2037.686
0.0015785	2208.532
0.0017000	2378.945

Table D.2 and D.3 list the hole-level Reynolds number calculated for each hole closure

orientation with respect to input Mass flow rate, for l_h = 1.5 mm & 3 mm samples. The formula for calculating Hole-level Reynolds number is given by equation 2.18 of chapter 2.

Table D.2: Hole-level Reynolds number for input Mass flow rate, l_h = 1.5 mm

Mass flow rate m^*	**Re$_h$ for each Hole Closure (%)**								
	0	**12.5**	**25**	**37.5**	**50**	**62.5**	**75**	**87.5**	**100**
0.0001215	11.16	11.27	11.46	11.94	13.41	15.60	18.28	21.56	25.66
0.000234	21.59	21.79	22.13	23.08	25.94	30.06	35.11	41.36	49.61
0.0003645	33.62	33.95	34.47	35.94	40.42	46.81	54.68	64.35	77.32
0.0004855	44.78	45.23	45.91	47.87	53.85	62.35	72.85	85.91	103.03
0.000607	55.99	56.55	57.41	59.86	67.33	77.96	91.08	107.48	128.80
0.0007285	67.20	67.86	68.92	71.85	80.81	93.56	109.32	129.04	154.58
0.00085	78.43	79.20	80.43	83.86	94.31	109.09	127.57	150.61	180.38
0.0009715	89.57	90.53	91.93	95.86	107.80	124.70	145.80	172.15	206.17
0.001093	100.75	101.86	103.41	107.83	120.94	140.46	164.04	193.70	231.97
0.0012145	111.94	112.93	114.93	119.82	134.45	156.02	182.28	215.25	257.82
0.0013355	123.24	124.25	126.42	131.80	148.32	171.63	200.50	236.73	283.59
0.001457	134.45	135.68	137.95	143.54	161.77	187.26	218.72	258.27	309.54
0.0015785	145.72	147.17	149.51	155.58	175.33	202.88	236.74	279.81	335.21
0.001700	156.97	158.57	160.92	174.72	188.89	218.54	254.96	301.40	364.04

Table D.3: Hole-level Reynolds number for input Mass flow rate, l_h = 3 mm

Mass flow rate m^*	**Re$_h$ for each Hole Closure (%)**								
	0	**12.5**	**25**	**37.5**	**50**	**62.5**	**75**	**87.5**	**100**
0.0001215	44.78	45.46	46.25	48.43	53.79	62.45	73.21	86.71	103.35
0.000234	86.67	87.85	89.43	93.18	103.87	120.71	141.54	166.88	200.04
0.0003645	134.95	136.80	139.28	145.19	161.77	188.09	220.44	259.71	311.47
0.0004855	179.50	182.19	185.60	193.46	215.44	250.52	293.65	345.89	414.27
0.000607	224.78	227.79	231.98	241.83	269.37	313.26	367.16	432.50	518.79
0.0007285	269.73	273.38	278.41	290.19	323.26	375.98	440.63	519.09	622.54
0.00085	314.77	319.02	324.90	338.63	377.30	438.74	514.16	605.62	726.48
0.0009715	359.75	364.62	370.89	387.03	431.14	501.52	587.70	692.31	830.29
0.001093	404.78	409.73	417.23	434.90	484.39	564.03	661.22	778.93	934.21
0.0012145	449.87	455.07	463.51	483.42	538.15	627.01	734.86	865.69	1038.27
0.0013355	494.75	501.16	510.60	531.73	592.98	688.71	808.26	952.29	1141.86
0.001457	539.69	547.39	557.19	580.75	646.98	750.74	881.82	1037.83	1245.57
0.0015785	584.74	592.78	603.71	629.14	700.93	816.02	955.38	1126.63	1349.56
0.001700	630.02	638.59	650.30	677.70	755.27	878.25	1027.87	1212.26	1454.05

E

List of Flow Parameters for Static and Dynamic configurations

This appendix lists the Flow Permeability K, Form Factor C and Flow Resistivity R values for l_h = 1.5 mm & 3 mm samples in Static and Dynamic configurations.

Table E.1: Flow Permeability values for Static and Dynamic configurations

Hole Closure	$\mathbf{K}_{1.5mm}$		$\mathbf{K}_{3mm}$	
	Static	**Dynamic**	**Static**	**Dynamic**
100%closed	2.66E-10	3.32E-10	7.48E-11	4.82E-11
87.5%closed	5.19E-10	7.21E-10	4.59E-10	1.34E-10
75%closed	1.30E-09	1.11E-09	6.99E-10	3.65E-10
62.5%closed	2.39E-09	1.90E-09	1.03E-09	8.21E-10
50%closed	2.79E-09	3.99E-09	1.18E-09	1.27E-09
37.5%closed	3.86E-09	4.59E-09	1.24E-09	1.51E-09
25%closed	3.86E-09	4.66E-09	1.24E-09	1.56E-09
12.5%closed	4.10E-09	4.72E-09	1.25E-09	1.55E-09
0%closed	4.16E-09	4.85E-09	1.27E-09	1.53E-09

Table E.2: Form Factor values for Static and Dynamic configurations

Hole Closure	$\mathbf{C}_{1.5mm}$		$\mathbf{C}_{3mm}$	
	Static	**Dynamic**	**Static**	**Dynamic**
100%closed	3.69E+05	2.22E+04	1.30E+06	1.36E+05
87.5%closed	1.13E+05	3.67E+04	6.49E+05	2.27E+05
75%closed	8.51E+04	2.95E+04	2.01E+05	1.46E+05
62.5%closed	2.62E+04	2.12E+04	1.13E+05	7.81E+04
50%closed	1.68E+04	8.22E+03	3.85E+04	4.03E+04
37.5%closed	5.13E+03	3.05E+03	1.28E+04	2.22E+04
25%closed	1.60E+03	1.27E+03	1.18E+04	1.32E+04
12.5%closed	7.73E+02	7.76E+02	1.41E+04	9.00E+03
0%closed	5.52E+02	7.38E+02	9.54E+03	7.20E+03

Table E.3: Flow Resistivity values for Static and Dynamic configurations

Hole Closure	$\mathbf{R}_{1.5mm}$		$\mathbf{R}_{3mm}$	
	Static	**Dynamic**	**Static**	**Dynamic**
100%closed	6.90E+04	5.46E+04	2.43E+05	3.76E+05
87.5%closed	3.53E+04	2.52E+04	3.97E+04	1.35E+05
75%closed	1.41E+04	1.63E+04	2.59E+04	4.97E+04
62.5%closed	7.61E+03	9.56E+03	1.76E+04	2.21E+04
50%closed	6.52E+03	4.55E+03	1.54E+04	1.43E+04
37.5%closed	4.75E+03	3.96E+03	1.47E+04	1.20E+04
25%closed	4.76E+03	3.90E+03	1.46E+04	1.16E+04
12.5%closed	4.47E+03	3.84E+03	1.45E+04	1.17E+04
0%closed	4.38E+03	3.74E+03	1.43E+04	1.18E+04